TECHNISCHE UNIVERSITÄT DRESDEN

Hydrogen Isotope Transport and Separation via Layered and Two-Dimensional Materials

DISSERTATION

zur Erlangung des akademischen Grades

Doktor der Naturwissenschaften

(Dr. rer. nat.)

am Bereich Mathematik und Naturwissenschaften

der Technische Universität Dresden

vorgelegt von

M.Sc. Yun An

geboren in Shanxi, China

Erstgutachter:	Prof. Dr. Thomas Heine
Zweitgutachter:	Prof. Dr. Ralf Tonner
Tag der Verleihung:	19 April 2021

Dresden, 19 Januar 2021

Tag der mündlichen Prüfung: 19 April 2021

Die Dissertation wurde in der Zeit von Oktober 2016 bis Januar 2021 an der Technischen Universität Dresden unter der Betreuung von Prof. Dr. Heine durchgeführt.

Abstract

The enrichment of heavy hydrogen isotopes (deuterium, tritium) is required to fulfill their increasing application demands, e.g., in isotope related tracing, cancer therapy and nuclear reaction plants. However, their exceedingly low natural abundance and the close resemblance of physiochemical properties to protium render them extremely difficult to be separated. In this thesis, we investigate hydrogen isotope transport and separation via layered and two-dimensional materials. Three different theoretical challenges are undertaken in this work: (1) identification of the transported hydrogen species (proton H^+ or protium H atom) inside interstitial space of layered materials (hexagonal boron nitride, molybdenum disulfide and graphite) and elucidation of their transport mechanism; (2) separation of hydron (proton H^+, deuteron D^+, and triton T^+) isotopes through vacancy-free graphene and hexagonal boron nitride monolayers; (3) capture of the extremely rare light helium isotope (^{3}He) with atomically thin two-dimensional materials.

In the case of hydrogen transport, the essential challenges are investigation of its mechanism as well as the identification of transported particles. Regarding the case of hydron isotope separation, the essential questions are whether or not pristine graphene is permeable to the isotopes, and how quantum tunneling and topological Stone-Wales 55-77 defects affect their permeation and separation through graphene. In the last case, to capture the light helium isotope, quantum tunneling, which favors the lighter particles, is utilized to harvest ^{3}He using graphdiyne monolayer. Our results provide novel theoretical insights into hydrogen particle transport inside the interstitial space of van der Waals materials; they uncover the mechanism of hydron isotope separation through 2D graphene and hexagonal boron nitride monolayers; and they predict the influence of pure quantum tunneling on the enrichment of ^{3}He through graphdiyne membrane.

Index of Abbreviations

1D	one-dimensional
2D	two-dimensional
3D	three-dimensional
5MR	5-membered ring
6MR	6-membered ring
7MR	7-membered ring
AFM	atomic force microscope
BO	Born-Oppenheimer
BOMD	Born-Oppenheimer molecular dynamics
BZ	Brillouin zone
CAQS	chemical affinity quantum sieving
CC	coupled cluster
CCSD(T)	coupled cluster with single and double excitations, triple excitations estimated using perturbation theory
CSVR	canonical sampling through velocity rescaling
CV	collective variable
CVD	chemical vapor deposition
DFT	density functional theory
D_2O	heavy water
FES	free energy surface
GGA	generalized gradient approximation
GS	Girdler-Sulfide
GDY	graphdiyne
GY	graphyne
h-BN	hexagonal boron nitride

HF	Hartree-Fock
KQS	kinetic quantum sieving
KS	Kohn-Sham
LDA	local density approximation
MetaD	metadynamics
MD	molecular dynamics
MoS_2	molybdenum disulfide
MP2	second order Møller–Plesset perturbation theory
NQE	nuclear quantum effect
PBE	Perdew–Burke-Ernzerhof
PES	potential energy surface
PIMD	path-integral molecular dynamics
SE	Schrödinger equation
SW	Stone-Wales
TEM	transmission electron microscopy
vdW	van der Waals
WKB	Wentzel-Kramers-Brillouin
WT-MetaD	well-tempered metadynamics
ZPE	zero-point energy

List of Symbols

D^+	deuteron
D_d	self-diffusion coefficient
E	total energy
E_a	activation energy
$f(p)$	momentum probability distribution of particles
H^+	proton
^3He	light helium isotope
^4He	helium
h	Planck constant
$\hbar$	reduced Planck constant
k	wave number
k_B	Boltzmann constant
k_f	force constant
k_r	rate constant
$T(E)$	transmission coefficient
T	temperature
T^+	triton
U_{max}	maximum energy barrier height
u	total particle flow
u_{class}	classical particle flow
u_{tunnel}	particle flow due to quantum tunneling
β	inverse of temperature, $\beta=1/k_BT$

Contents

1. Introduction

1.1 Hydrogen Isotope Separation

It has long been recognized that nuclear energy is crucial in balancing energy supply, environment, and economic development [1]. Nuclear power, as one of the major sources of electricity generation, releases less radiation into environment than any other approaches [2], which would create sustainable energy supply for the future. Currently, the main approaches obtaining nuclear power include—nuclear fission [3, 4], fusion [3, 5], and decay [3]. Among them, fusion is expected to have many advantages over the other two: it has the increased safety, reduced radioactivity, and less high-level nuclear waste [6]. Thus, investing fusion power would have significant long-term influence worldwide. Heavy hydrogen isotopes (deuterium D and tritium T), as important fuels in fusion reactors are, therefore, required in large amounts to fulfill their increasing demands.

Deuterium, the stable heavy isotope of protium, consists of a proton and a neutron, exists in surface water on earth with an abundance around 0.013% [7]. Deuterium is often used as fuels [8] in fusion reactions; in addition, heavy water (D_2O) is a key input material as neutron moderator in nuclear engineering [9]. Tritium, the heaviest hydrogen isotope in nature, contains one proton and two neutrons. Tritium is radioactive [10] and decays into light helium (^3He) with the half-life of 12.3 years. Along with deuterium, tritium serves as fuel in nuclear fusion reactions [11]. In addition to the usage in nuclear industry, heavy hydrogen isotopes have applications in many other fields, e.g., hydrogen isotope related tracing [12, 13] and cancer therapy [14] in

medical research. The separation of heavy hydrogen isotopes is, therefore, exceedingly important.

However, due to the extremely low natural abundance of heavy hydrogen isotopes [7] and the close resemblance in physicochemical properties with protium, separating the mixture of these isotopes is rather challenging. Conventional separation approaches, such as water distillation and water–hydrogen sulfide exchange [15], are exceedingly energy intensive with low separation factors, usually less than 2.5 [16]. Thus, searching for alternative approaches, with high efficiency and low energy cost to separate hydrogen isotopes, is of great importance.

1.1.1 State-of-the-art Industrial Deuterium Enrichments

Currently, several techniques are used for separating hydrogen isotopes on the industrial-plant scale, including distillation of water, Girdler-Sulfide (GS) process [16], and water–hydrogen sulfide exchange [15]. In general, these methods consume large amounts of energy, but their separation factors are rather low. Table 1.1.1 summarizes a few approaches used in the industrial production of deuterium [16].

Table 1.1.1 Overview of D_2O production processes, adapted from Ref. [16].

Process	**Separation Factor**	**Energy Cost**	**Natural Exchange Rate**
Distillation of H_2O	1.015 to 1.055	Very high	Moderate
Distillation of Liquid H_2	～1.5	Moderate	Slow
Water electrolysis	5 to 10	Very high	Fast
Water-Hydrogen sulfide exchange	1.8 to 2.3	High	Fast
Ammonia-hydrogen exchange	2.8 to 6	Moderate	Slow, catalyst needed
Water-hydrogen	2 to 3.8	Moderate	Almost nonexistent, catalyst needed

Among these techniques, the promising ones are based on the chemical exchange, with the archetype of the GS process [16], which was developed independently by K. Geib and J. S. Spevack in 1943 [17]. In the GS process, heavy water (D_2O) is produced by isotopic exchange between H_2O and hydrogen sulfide (H_2S) (and vice versa [18, 19]), with the chemical exchange equilibrium reaction:

$$H_2O\ (l) + HDS(g) \rightleftharpoons HDO\ (l) + H_2S(g)$$

The equilibrium constant for the reaction corresponds to the separation factor. GS process includes two sieve tray columns, one is referred to as cold tower, as it is maintained at 30 ℃; the other is at 130 ℃ and is referred to as hot tower. The difference in separation between 30 ℃ and 130 ℃ guarantees the enrichment. The separation factor is 2.33 at 30 ℃ and 1.82 at 130 ℃ [18].

Other alternative approaches, such as water distillation, are based on the small difference of boiling points of the components: the boiling points of H_2O (100.0 ℃) and D_2O (101.4 ℃) differ by only 1.4 ℃ [20]. The process of distillation is quite straightforward, yet the tiny boiling point difference makes the energy cost very high and the separation factor is low, only around 1.015-1.055 [16]. These weaknesses of the conventional techniques stimulate the researches on other separation methods, which could offer more efficient separation, as introduced in following sections, and which is also one of the motivations of this thesis.

1.1.2 Quantum Sieving

In 1995, Beenakker et al. [21] proposed the Kinetic Quantum Sieving (KQS) method, according to which, nanoporous materials can act as quantum sieves to separate hydrogen and helium isotopes, owing to the non-negligible nuclear quantum effect (NQE) in the processes. The condition of KQS is that the difference between the diameter of pore in the porous material and the hard core of the isotope particles should

be comparable to the de Broglie wavelength of the particle, thereby the NQE would play a significant role. The isotopes can, therefore, be separated by the different NQE.

According to the law of equipartition, the thermal de Broglie wavelength λ of a particle is expressed as:

$$\lambda = \frac{h}{\sqrt{3mk_{\mathrm{B}}T}} \tag{1.1.1}$$

where m is the mass of the particle and h is Planck constant, k_{B} and T are the Boltzmann constant and temperature, respectively. Table 1.1.2 gives the de Broglie wavelengths of several species at different temperatures, from which one can see that for light isotopes, such as H and D, even at room temperature, the de Broglie wavelengths are still considerable.

Table 1.1.2 The de Broglie wavelengths of particles at different temperatures.

Species	**Temperature (K)**	**λ (Å)**
H	300	1.45
D	300	1.03
T	300	0.84
H_2	300	1.03
H_2	77	2.03
H_2	20	3.99
D_2	300	0.73
D_2	77	1.44
D_2	20	2.83
He	300	0.73
He	4	6.32

It is clear that heavier isotopes have shorter de Broglie wavelengths than their lighter counterparts, the effective radius for the heavier isotope is therefore smaller, see Figure

1.1.1b. As a result, in KQS, the diffusion of heavier isotope is faster than the lighter ones. KQS method opens the door for exploring porous materials to sieve isotopes [22-33], with relatively high separation factors. However, in order to separate the isotopes efficiently, the difference of de Broglie wavelengths between them should be large enough, which usually requires cryogenic temperature [24]. Since cryogenic condition still costs huge energy, practical applications of KQS are limited.

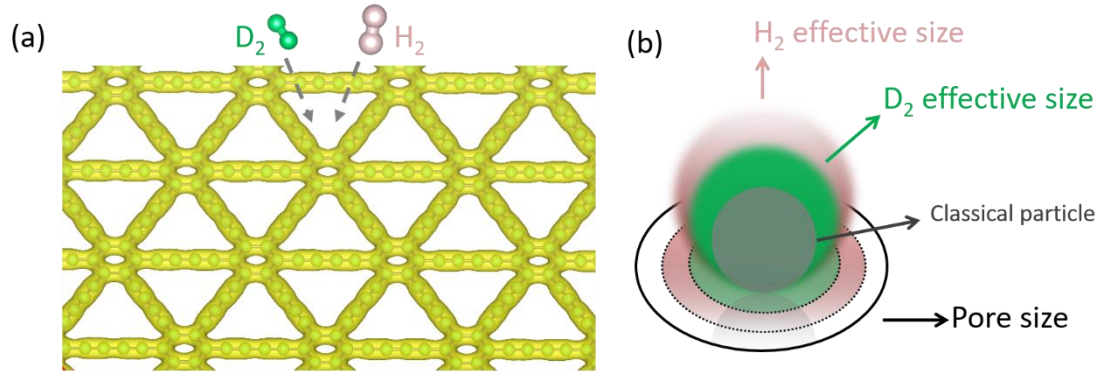

Figure 1.1.1 Schematic of KQS. (a) When the de Broglie wavelengths of the particles (here using H_2 and D_2 as example) are comparable to the pore size in the porous material, quantum sieving takes place. (b) Zoom in of H_2 and D_2 confined in a pore. The pink and green spheres represent the effective sizes of H_2 and D_2, respectively; the grey sphere represents the classical particle; the black circle is the effective pore size of the material.

Another approach for separating hydrogen isotopes was reported in 2013, known as chemical affinity quantum sieving (CAQS) [25], which is not limited by the pore size of materials. In CAQS, molecules bound on the strong adsorption sites of host materials, the adsorbate–adsorbent interactions lead to different bond strengths and, therefore, different zero-point energies (ZPE)—the minimum energy a quantum particle possess (even at 0 K), as shown in Figure 1.1.2. Consequently, this results in different adsorption enthalpies ΔH, which causes the overall separation. Since heavier isotopes have smaller ZPE, the interaction sites of materials preferably adsorb the heavy hydrogen isotopes. Methods based on the KQS and CAQS have been investigated in the past decades [22-33], their low temperature conditions, however, remain an ongoing challenge.

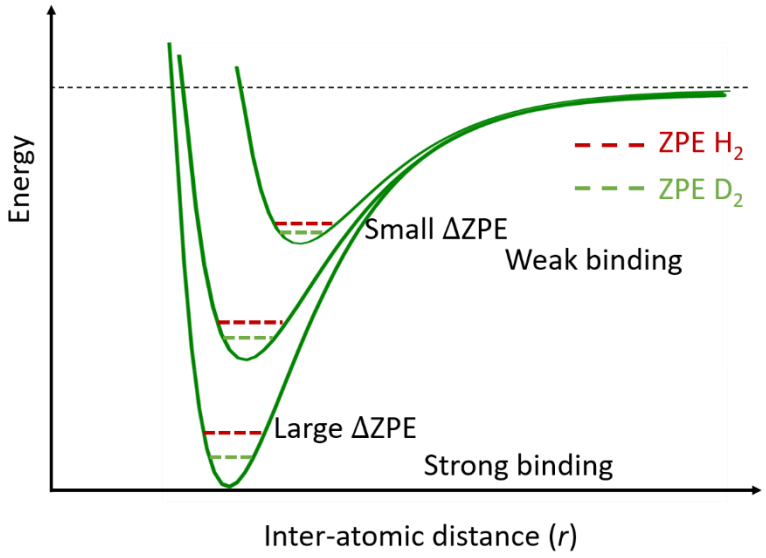

Figure 1.1.2 Qualitative energy curves of strengths of the adsorption sites in CAQS. The steeper the potential well depth, the larger difference of ZPE between the isotopes. The red and green dashed lines represent ZPE of H_2 and D_2, respectively.

1.1.3 Novel Hydrogen Isotope Separation Techniques

Hydrogen Isotope Transport and Separation via Layered Materials

Recently, Hu et al. [34] demonstrated that at room temperature, hydrogen isotopes can be separated via van der Waals (vdW) layered materials, e.g., hexagonal boron nitride (*h*-BN) and molybdenum disulfide (MoS_2). In the experiment setup [34], the hydrogen isotopes were injected by the palladium electrodes—PdHx, they then entered into the layered materials with different entry barriers. Since deuterium has smaller de Broglie wavelength than that of protium (see Table 1.1.2), it experiences a lower entry energy barrier, which results in the separation: for D/H is 1.4 in *h*-BN and 1.2 in MoS_2 [34] at room temperature. The schematic for this process is shown in Figure 1.1.3. One of the outstanding parts of this finding is that the working environment is simply at ambient conditions, so no cryogenic temperature is needed, which could largely reduce the energy consumption. The vdW materials with proper interstitial space could, therefore, serve as quantum sieves for hydrogen isotopes.

While the separation was caused by different entry barriers between the isotopes, the experimental setup does not conclude which hydrogen species got transported in the process: whether H atom or H^+ entering from PdHx electrode is difficult to estimate due to the unknown atomistic details. In principle, they both have the possibility to enter into the interstitial space of layered materials; yet, their transport is ambiguous. Because if the protons were injected and entered into the interlayer space, the immediate neutralization is expected, as proton's electron affinity of 13.6 eV is significantly higher than the work function of the host materials. On the other hand, if the interjected species were H atoms, any two H atoms encountering each other are expected to recombine immediately, for the high binding energy when forming H_2 (4.52 eV in the gas phase [35]); but H_2 molecules cannot transport inside the narrow interstitial space of these vdW crystals, which was confirmed by the experiment [34]. Therefore, which hydrogen species indeed transport through the layered materials and what are their transport mechanisms, require further investigations.

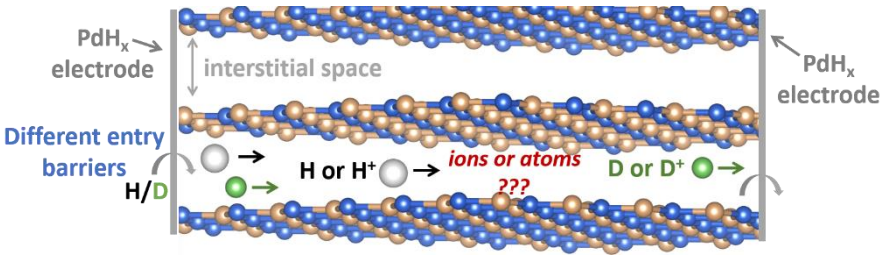

Figure 1.1.3 Schematic of hydrogen isotope transport inside layered *h*-BN, heavier isotopes experience smaller entry barriers and diffuse faster. Yet, whether H^+ or H were injected from the PdHx electrode is unclear, i.e., the species of transported particle (ions or atoms) is unknown inside layered materials.

Hydron Isotope Separation Through 2D Materials

For a long time, pristine graphene monolayer was considered to be impermeable to any molecules, atoms, ions. Even for the particle as small as proton, the energy barrier estimated for a proton through pristine graphene is still very high, e.g., around 1.4-1.6 eV from first-principle calculations [36-38]. Such high energy barrier indicate it is impossible for protons to transfer through perfect graphene, unless defects were

introduced on the membrane [39]. However, recent experimental work by Geim and co-workers [40] showed that protons can surprisingly permeate through pristine graphene, with a relatively low energy barrier around 0.8 eV, which is reduced at least by 0.5 eV compared with previous theoretical predicted values [36-38]. In 2016, the same group further found that pristine graphene monolayer not only allows protons to transfer through, it can also sieve hydron isotopes (proton H^+ and deuteron D^+) at room temperature, with a high H^+/D^+ separation factor of 10 [41], which is much more efficient than conventional separation approaches [16]. Figure 1.1.4 depicts the schematic of the separation process. Similar selectivity of H^+/D^+ was also detected for *h*-BN monolayer. The finding demonstrates that graphene and *h*-BN monolayers can be excellent candidates in the future hydrogen isotope separation technologies. However, why vacancy-free graphene can allow protons to go through and what causes the separation of the isotopes, are still not well understood so far, which needs further investigations.

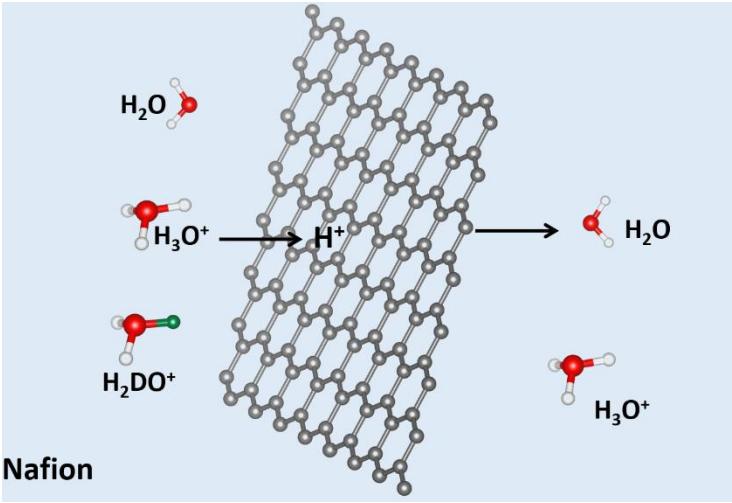

Figure 1.1.4 Schematic of aqueous proton (H^+) and deuteron (D^+) permeation through graphene monolayer.

1.2 Motivation and Objectives

As elucidated in Section 1.1.3, layered crystals and 2D materials have great potential in hydrogen isotope separation. However, the transport and separation mechanisms in

these processes are not well understood to date, which motivates us to investigate deeper in this thesis, summing up as follows.

(1) For hydrogen isotope separation and transport in the interstitial space of layered materials [34], while the difference in the entry barrier of the hydrogen isotopes into the interstitial space of the layered materials was found to be the driving factor for the isotope separation; the transported species inside the interstitial space and the transport mechanism were not clear. In the experimental setup [34], the hydrogen species were injected from the palladium electrodes, PdHx. Yet, the setup could not distinguish whether protons (H^+) or protiums (H atoms) enter the layered material: for protons, immediate neutralization is expected, as the proton's electron affinity of 13.6 eV is significantly higher than the work function of the host materials, even for a wide band gap insulator as *h*-BN. On the other hand, any two protium atoms encountering each other are expected to recombine immediately because of the high binding energy when forming H_2 (4.52 eV in the gas phase) [35]; and H_2 molecules cannot transport in between the small interstitial space of these layered materials [34]. Thus, the observed transport process of hydrogen through *h*-BN and MoS_2 requires further investigations to identify the transported species and their transport mechanisms. To this end, in part I of this thesis, we will explore the transport mechanism and identify the species of particle (H^+ or H atoms) transferred in the interstitial space of layered vdW materials (layered *h*-BN, MoS_2 and graphite).

(2) The vacancy-free graphene and *h*-BN monolayers have shown surprisingly high H^+/D^+ selectivity at room temperature [41]. However, whether or not 2D vacancy-free graphene and *h*-BN can let hydron isotopes permeate through was rather controversial, which triggered a debate between theoretical and experimental sides. For instance, state-of-the-art calculations estimate transfer energy barriers of about 1.4-1.6 eV for a single proton passing through a pristine graphene sheet [36-38], which indicate that perfect graphene is essentially impermeable to proton at ambient condition. On the other hand, Lozada-Hidalgo et al. [41-43] unambiguously pointed

out that the high permeability and high isotope selectivity are from vacancy-free graphene, and the energy barrier measured from the experiment is at least 0.5 eV lower than the theoretical predicated ones. Recent nano-balloon tests further stated that there are no atomic-vacancy defects in the graphene used in the previous experiments [43]. Thus far, the underlying mechanism behind this finding is still unknown. The proposed hypotheses include atomic defects [39] or local hydrogenation [44, 45]. However, neither could explain both the high permeability and remarkable selectivity of the atomically thin membranes. To find out the full picture behind 2D monolayers sieving hydron isotopes, in part II of this work, we aim to investigate the mechanism of hydron isotope separation through vacancy-free 2D graphene and *h*-BN monolayers. In particular, the influence of quantum tunneling to the ion separation will be addressed.

(3) Besides graphene and *h*-BN, other 2D nano-porous materials with proper pore size could have potential in separating isotopes as well. Utilizing the method developed for investigating the influence of quantum tunneling would be a good approach to screen the porous materials for different isotopes. Except hydrogen, other elements, such as helium isotopes (^{3}He and ^{4}He) could also be separated through 2D porous monolayers. To this regard, we investigate the experimentally available [46] one-atom-thick carbon allotrope of graphyne [47, 48] and graphdiyne [49-51] monolayers for ^{3}He and ^{4}He isotope separation.

1.3 Outline

The outline of this thesis is as follows: Chapter 2 introduces the theoretical methods employed in this work, aiming to give a brief overview of the general theoretical backgrounds of the studies.

In Chapter 3, basic properties of the investigated layered (*h*-BN, MoS_2, graphite) and 2D (graphene and *h*-BN monolayers) materials are reviewed. The experimental techniques for the production of 2D single-layers are also introduced.

Chapter 4 presents the results of hydrogen particle transport in-between the interstitial space of layered *h*-BN, MoS_2, and graphite, focusing on identifying the category of the hydrogen species and investigating the transport mechanism. Density functional theory (DFT) calculations combined with well-tempered metadynamics (WT-MetaD) simulations at finite temperature are employed. Influence of the common sulfur vacancy defect in MoS_2 is investigated as well.

Chapter 5 and Chapter 6 constitute Part II of this work, they focus on hydrogen isotope separation. The main body of Part II is Chapter 5, which shows the results of separating hydron isotopes through graphene and *h*-BN monolayers. The effect of quantum tunneling is investigated. To explore the influence of ring size to the permeation and separation, the topological Stone-Wales defect and local hydrogenation of the graphene membrane are studied.

Chapter 6 deals with the one-atom thick materials of graphyne and graphdiyne to sieve helium isotopes (^{3}He and ^{4}He).

Chapter 7 summarizes the main conclusions and outlook of this work.

2. Theoretical Background

In this chapter, the theoretical framework used in this thesis is summarized. We start with the Born-Oppenheimer (BO) approximation [52], as it is one of the most fundamental approximations in many-body theory. BO approximation decouples the electronic and the nuclear motion of atoms, the wave function in Schrödinger equation can, therefore, be treated as a product of electronic and nuclear terms. This makes it possible to solve the motions of electrons and nuclei independently, which highly simplifies the many-body problem. In this thesis, all methods employed the BO approximation. In Section 2.2 we turn to the electronic structure methods and introduce the Density Functional Theory (DFT). As one of the most widely used methods for the electronic structure nowadays, DFT provides a great balance between the accuracy and computational cost, the ground state of electrons is well described. In this work, DFT is mainly employed for the electronic structure calculations.

Since the second part of this thesis deals with hydrogen isotope separation, the motions of nuclei must be considered. To this end, we discuss the nuclear quantum effects (NQE) in Section 2.3. Both equilibrium and non-equilibrium scenarios are considered: for the former, the harmonic approximation is discussed for the nuclear Schrödinger equation; for the later, we introduce quantum tunneling, which is employed for describing hydron isotopes permeating through 2D membranes.

In chemistry, free energy difference describes well for the physical movement of particles in a system, and molecular dynamics (MD) simulation is a good approach to obtain it. Part of this thesis investigates the transport of hydrogen particles inside layered crystals, where we employ well-tempered metadynamics (WT-MetaD)

simulations to get the free energy barrier. Therefore, in Section 2.4, free energy calculations are introduced to get a brief overview of the methods. In addition, for a general reaction, its activation energy, which is usually obtained from the Arrhenius equation, can give important information. Yet, when the NQE plays an important role in the reaction, the Arrhenius equation could fail and non-Arrhenius behavior would be observed. We will briefly discuss this in Section 2.5.

2.1 Born-Oppenheimer Approximation

A system that consists of electrons and nuclei can be described by the non-relativistic, time-independent Schrödinger equation:

$$H\Psi(\boldsymbol{r},\boldsymbol{R}) = E\Psi(\boldsymbol{r},\boldsymbol{R}) \tag{2.1.1}$$

where H and E are the Hamilton and energy of the system, respectively, and Ψ is the many body wave-function.

For N_n nuclei with mass M_I at the position $\boldsymbol{R}_I$ and N_e electrons with mass m_e and charge $-e$ at the position $\boldsymbol{r}_i$, the total Hamiltonian in Equation (2.1.1) can be given as (here written in natural units, $m_e = e = \hbar = 1/4\pi\varepsilon_0 = 1$):

$$H = \underbrace{-\sum_{I}^{N_\mathrm{n}} \frac{1}{2M_I}\nabla_\mathrm{I}^2}_{T_\mathrm{n}} \underbrace{-\sum_{i}^{N_\mathrm{e}} \frac{1}{2}\nabla_\mathrm{i}^2}_{T_\mathrm{e}} + \underbrace{\frac{1}{2}\sum_{I\neq J}^{N_\mathrm{n}} \frac{Z_I Z_J}{|\boldsymbol{R}_I - \boldsymbol{R}_J|}}_{V_\mathrm{n-n}} + \underbrace{\frac{1}{2}\sum_{i\neq j}^{N_\mathrm{e}} \frac{1}{|\boldsymbol{r}_i - \boldsymbol{r}_j|}}_{V_\mathrm{e-e}} \underbrace{-\sum_{I}^{N_\mathrm{n}}\sum_{i}^{N_\mathrm{e}} \frac{Z_I}{|\boldsymbol{r}_i - \boldsymbol{R}_I|}}_{V_\mathrm{n-e}} \tag{2.1.2}$$

where the first right-hand term is the kinetic energy of the nuclei T_n, the second term represents the kinetic energy of the electrons T_e, the third and fourth terms are the Coulomb repulsion between the nuclei ($V_\mathrm{n-n}$) and the electrons ($V_\mathrm{e-e}$), respectively, and the final term is the Coulomb attraction between the electrons and the nuclei ($V_\mathrm{n-e}$).

Equation (2.1.1) has possible solutions only for the simplest quantum system, such as the hydrogen atom. For many-body systems, approximations are required, one of which

is the Born-Oppenheimer (BO) approximation [52]. In the BO approximation, the motions of electrons are separated from those of the nuclei, and the coupling terms between the nuclei and the electrons are neglected. The total wave function in the BO approximation is expressed by the electronic and the nuclear wave functions:

$$\Psi(\boldsymbol{r_i}, \boldsymbol{R_I}) = \psi_{\mathrm{e}}(\boldsymbol{r_i})\psi_{\mathrm{n}}(\boldsymbol{R_I}) \tag{2.1.3}$$

where $\boldsymbol{R}$ and $\boldsymbol{r}$ specify the positions of the nuclei and the electrons, respectively; i and I are the indexes of electrons and nuclei; $\psi_{\mathrm{e}}(\boldsymbol{r_i})$ is the electron wave function while $\psi_{\mathrm{n}}(\boldsymbol{R_I})$ is the nuclear wave function.

The electronic and the nuclear Schrödinger equation can be written as:

$$E_{\mathrm{e}}\psi_{\mathrm{e}}(\boldsymbol{r_i}) = H_{\mathrm{e}}\psi_{\mathrm{e}}(\boldsymbol{r_i}) \tag{2.1.4 a}$$

$$E_{\mathrm{n}}\psi_{\mathrm{n}}(\boldsymbol{R_I}) = H_{\mathrm{n}}\psi_{\mathrm{n}}(\boldsymbol{R_I}) \tag{2.1.4 b}$$

where E_{e} and E_{n} are the total electronic energy and total nuclear energy, respectively.

The separation of electronic and nuclear degrees in the BO approximation allows to solve the electrons and nuclei independently. In this work, both electronic and nuclear motions will be considered: in Section 2.2, introductions for the electronic structure methods of DFT are given; while in Section 2.3, the harmonic approximation and Wentzel-Kramers-Brillouin (WKB) approximation [53] are introduced to include the nuclear motion in the Schrödinger equation.

Owing to the fact that nuclei are much heavier than electrons (the mass difference between nuclei and electrons yields several orders of magnitude), the motions of nuclei are much more sluggish than electrons. Therefore, the nuclei can be treated as fixed and the electrons move immensely faster and only feel the potential produced by the fixed nuclei. So the electronic Hamiltonian in Equation (2.1.4 a) can be written as follows:

$$H_e = \underbrace{-\sum_{i}^{N_e} \frac{1}{2}\nabla_i^2}_{T_e} + \underbrace{\frac{1}{2}\sum_{i\neq j}^{N_e} \frac{1}{|\boldsymbol{r}_i - \boldsymbol{r}_j|}}_{V_{e-e}} - \underbrace{\sum_{I}^{N_n}\sum_{i}^{N_e} \frac{Z_I}{|\boldsymbol{r}_i - \boldsymbol{R}_I|}}_{V_{nuc-e}} \tag{2.1.5}$$

Generally speaking, the interaction term V_{e-e} in Equation (2.1.5) impedes any straightforward analytic solution, as when describing a system, an exact solution would imply dealing with $\sim 10^{23}$ particles, which is too demanding for practical applications. In order to solve electronic Schrödinger Equation, approximations are necessary, one of the most popular approaches is Density Functional Theory (DFT).

2.2 Density Functional Theory

DFT describes the electronic ground state structure on the basis of one variable — the electron density $n(\boldsymbol{r})$. The initial idea of DFT was proposed by Thomas [54] and Fermi [55] in 1927, then developed by Hohenberg and Kohn in 1964 [56], with the assumption that an interacting many electron system in an external potential $\upsilon(\boldsymbol{r})$, a functional of charge density $n(\boldsymbol{r})$ can represent its ground state energy E_υ, i.e. $E_\upsilon(n)$, instead of the formulation $E_\upsilon[\psi(\boldsymbol{r_1}, \boldsymbol{r_2}, \ldots, \boldsymbol{r_N})]$, where ψ is the wave function with N electrons in many-body theory. A year later, in 1965, Kohn and Sham proposed the famous Kohn-Sham (KS) equations [57], which assumes the ground state density of an interacting electron system is equal to another fictitious effective non-interacting system that has the exact same density as the interacting one. Nowadays, DFT has become one of the most popular methods for describing the weakly correlated ground state electrons.

2.2.1 Kohn-Sham Equations

KS equations [57] introduce an auxiliary system of non-interacting particles and assume it has the same ground state density as the real interacting system. The non-interacting electrons move in an effective potential $\upsilon = \upsilon_{aux}(\boldsymbol{r}) = \upsilon_{eff}(\boldsymbol{r})$.

The kinetic-energy can be separated into two components, one corresponds to a system of non-interacting electrons $T_s[n]$ and the other corresponds to the remaining part that accounts for the correlations $T_c[n]$:

$$T[n] = T_s[n] + T_c[n] \tag{2.2.1}$$

In this way, the problem got simplified significantly, since the kinetic-energy operator of a non-interacting system can be described by the Laplacian of single particle orbitals. Likewise, the potential energy related to the interaction between the electrons can be split to:

$$E_{e-e}[n] = E_H[n] + E_{xc}[n] \tag{2.2.2}$$

where $E_H[n]$ is the Hartree term [58] and $E_{xc}[n]$ is the exchange and correlation between the interacting electrons.

The total electronic ground state energy in KS equations is given by:

$$E_{KS}[n] = T_s[n] + E_H[n] + E_{ext}[n] + E_{xc}[n] \tag{2.2.3}$$

$E_{ext}[n]$ is the energy with the external potential and $E_{xc}[n]$ is the exchange-correlation energy, nearly all the quantum-mechanical many-body effects are involved in the term of $E_{xc}[n]$.

2.2.2 Exchange-Correlation Energy

In KS equations, the complexity of the many-body interaction is reflected in the exchange-correlation energy $E_{xc}[n]$, yet the exact form of this functional is unknown, necessary approximations are needed. Nowadays, A great number of exchange-correlation functionals are available, the most popular ones are summarized and presented in the "*Jacob's Ladder*" [59], going from "Earth of Hartree" ($E_{xc}[n] = 0$) to "Heaven of chemical accuracy" [59], as shown in Figure 2.2.1.

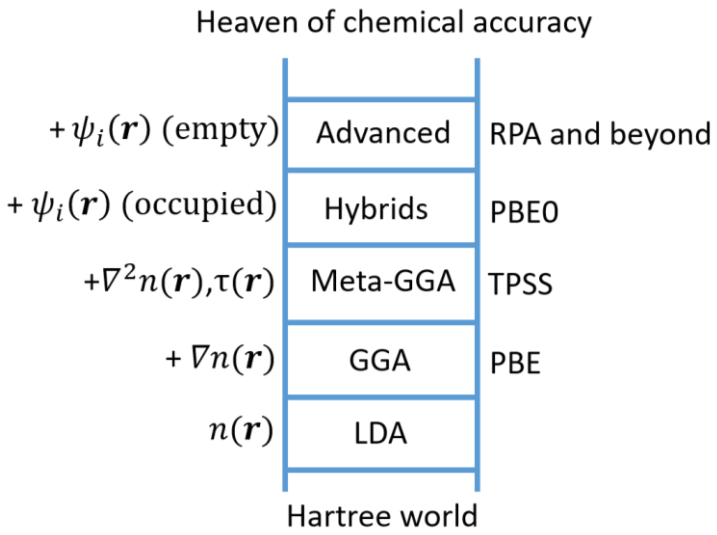

Figure 2.2.1 "*Jacob's ladder*" of exchange-correlation functionals, left side of the ladder are the factors each method depends on, right side are the representative methods of each rung.

The rungs on the *Jacob's ladder* are ordered by the sophistication of the methods. The first level of the ladder is the *local density approximation* (LDA). The idea of LDA is that for the homogeneous electron gas, the external potential density $n(\mathbf{r})$ is a constant (this also works for the inhomogeneous systems which have a slowly varying density). The exchange energy in LDA is known analytically but the correlation energy has no analytical form and can only be derived with the high or low density limit [60]. LDA usually tends to underestimate atomic ground-state energies as well as ionization energies, while the binding energies are usually overestimated [61].

In reality, the electron density in molecular systems is inhomogeneous and normally has clear variations, which is not the case in LDA. To overcome this disadvantage of LDA, the *generalized gradient approximation* (GGA) was proposed, which assumes that the exchange-correlation energies not only depend on the electron density but also on its gradient $\nabla n(\boldsymbol{r})$. GGA usually show a better performance than local methods, especially in geometries and ground-state energies of covalently bonded and weakly bound systems [62, 63]. One of the most widely used functionals of GGA is PBE, which

was developed by Perdew, Burke, and Ernzerhof [64]. PBE is usually referred to as a non-empirical GGA, for its parameters are obtained by considering the exact limits. In this thesis, PBE was employed in all the calculations presented in Chapters 4.

The third rung on the ladder are the Meta-GGA functionals [65, 66], which consider additionally, the Laplacian of the electron density $\nabla n(\boldsymbol{r})^2$ or the Kohn-Sham orbitals through the electron kinetic energy density $\tau(\boldsymbol{r})$.

The fourth rung of the *Jacob's ladder* are the hybrid functionals, they include a portion of the exact exchange from the Hartree-Fock (HF) method [67], the rest of the exchange-correlation energy is derived from other sources, such as DFT. Hybrid functionals devote to decrease the self-interaction errors in local functionals. Their computational cost is larger, as the non-local exchange operators need to be considered. One of the most popular hybrid functionals is PBE0 [68], which mixes the exact HF exchange energy and the PBE exchange energy as 1:3 ratio, and the correlation energy is fully from PBE. The exchange-correlation in PBE0 is expressed by the following form:

$$E_{\mathrm{XC}}^{\mathrm{PBE0}} = \frac{1}{4} E_{\mathrm{X}}^{\mathrm{HF}} + \frac{3}{4} E_{\mathrm{X}}^{\mathrm{PBE}} + E_{\mathrm{C}}^{\mathrm{PBE}} \tag{2.2.4}$$

The value of $1/4$ is considered from the fourth-order many-body perturbation theory [69].

Other E_{XC} functionals beyond the ones on *Jacob's ladder* are coming out every year [70]. However, one should keep in mind that simply adding the complexity to climb higher on *Jacob's ladder* does not necessarily lead to higher accuracies [71].

2.2.3 Dispersion Correction for DFT

One of the major weaknesses of standard local or semi-local DFT functionals is that the long range electron-correlation is not included there. The long range electron-correlation force, which is highly non-local and predominates when the atoms

(molecules) are close to each other, is usually referred to as the London dispersion force, for it was originally proposed by F. London in 1930 [72]. This interaction is caused by the instantaneous dipole developed in the atom (due to the permanent motion of electrons), which results in the electrostatic attraction between the atoms. Nowadays, it is generally accepted that taking dispersion into account is absolutely necessary [73] to get more accurate results, especially for the weakly interacting systems.

To make up for the exclusion of the long range dispersion in DFT, a variety of empirical or semi-empirical methods were developed for the correction of dispersion, the most commonly used series include DFT-D2 [74] and DFT-D3 [75], which were developed by Grimme et al. [75, 76]. The energy of the dispersion correction is a function of interatomic distances, with adjustable parameters fitted to conformational and interaction energies calculated at the CCSD(T)/CBS level.

The dispersion energy E_{disp} in the DFT-D approaches is calculated independently from the Kohn−Sham energy E_{KS} and the total energy. After dispersion correction, the total energy has the following form:

$$E_{\text{total}} = E_{\text{DFT}} + E_{\text{disp}} \tag{2.2.5}$$

In the DFT-D2, the dispersion energy is expressed by:

$$E_{\text{disp}}^{\text{D2}} = -\frac{1}{2}\sum_{i=1}^{N_{\text{at}}}\sum_{j=1}^{N_{\text{at}}}\frac{C_6^{ij}}{R_{ij}^6}s_6 f_{\text{d},6}(R_{ij}) \tag{2.2.6}$$

where N_{at} is the number of atoms in the system, C_6^{ij} is the dispersion coefficient for the atom pair *ij*, s_6 is the global scaling factor, and R_{ij} is the interatomic distance. The value of s_6 in the damping function changes in different DFT functionals, e.g., s_6 is 0.75 in PBE and 1.2 in BLYP [74]. The term $f_{\text{d},6}(R_{ij})$—the damping function, scales the force field, it can minimize the contributions from interactions within typical bonding distances. The form of $f_{\text{d},6}(R_{ij})$ is as following:

$$f_{\mathrm{d},6}(R_{ij}) = \frac{1}{1+\exp\left[-\mathrm{d}\left(R_{ij}/(s_{\mathrm{R}}R_{0ij})-1\right)\right]} \tag{2.2.7}$$

where parameter s_{R} is often fixed at 1.

In the DFT-D3 correction, the dispersion coefficient C_6 is environment−dependent and the energy term is expressed by:

$$E_{\mathrm{disp}}^{\mathrm{D3}} = -\frac{1}{2}\sum_{i=1}^{N_{at}}\sum_{j=1}^{N_{at}}\left(f_{\mathrm{d},6}(R_{ij})\frac{C_6^{ij}}{R_{ij}^6} + f_{\mathrm{d},8}(R_{ij})\frac{C_8^{ij}}{R_{ij}^8}\right) \tag{2.2.8}$$

The C_6 coefficient depends on the coordination number, if the hybridization state changes during the process, C_6 coefficient also changes simultaneously. For example, C_6 differs by ~35% between the sp^2 and sp^3 hybridized carbons. The damping function $f_{\mathrm{d,n}}(R_{i,j})$ in the DFT-D3 correction is expressed as:

$$f_{\mathrm{d},n}(R_{\mathrm{i,j}}) = \frac{s_n}{1+6\left(\frac{R_{ij}}{s_{\mathrm{R,n}}R_{0ij}}\right)^{-\alpha_n}} \tag{2.2.9}$$

where $R_{0ij} = \sqrt{C_{8ij}/C_{6ij}}$, the parameters α_6, α_8, $\mathrm{s_{R,8}}$ and s_6 are fixed numbers of 14, 16, 1 and 1, respectively; s_8 and $s_{\mathrm{R,6}}$ are adjustable parameters whose values are related to the exchange-correlation functionals [75].

DFT-D3 can use the Becke-Jonson (BJ) damping of the form:

$$f_{\mathrm{d},n}(R_{i,j}) = \frac{s_n R_{ij}^n}{R_{ij}^n + \left(\alpha_1 R_{\mathrm{0ij}} + \alpha_2\right)^n} \tag{2.2.10}$$

where s_6 is fixed value as 1, α_1, α_2 and s_8 are adjustable parameters. BJ damping has the advantage that one can avoid the repulsive interatomic forces at shorter distances. Interested readers can find further detailed discussions in Ref. [76].

DFT has been widely used in the electronic structure calculations, yet the results from DFT could change depending on the functionals. One can benchmark DFT energies with other methods, such as the Coupled Cluster (CC) theory [77, 78]. CC theory was

first proposed [78] in 1960 and was used for quantum chemical calculations in 1966 [79]. It is usually referred to as the "gold-standard" of quantum chemistry, and as the most accurate approach to solve the many-body problem [80]. In particular when dealing with single, double, and perturbative triple excitations, CC theory gives high accurate ground-state properties for molecules [81]. In this thesis, CCSD(T) method was used as the benchmark for the DFT results in Chapter 5. Interested readers can go to reviews such as Ref. [80] for further information about CC theory.

2.3 Nuclear Quantum Effects

Within the classical nuclei approximation, one fails to describe nuclear quantum effects (NQE), e.g., zero-point energy (ZPE) and quantum tunneling. Although NQE is often considered to be dominant only at low temperatures, for light nuclei, such as hydrogen, even at room temperature, NQE could still make a big difference. Another important consequence of neglecting NQE is that one loses the ability to predict equilibrium isotope effect. Since one of our goals in this thesis is hydrogen isotope separation, the motions of nuclei must be considered.

2.3.1 Nuclear Schrödinger Equation

Within the BO approximation, the nuclear Schrödinger equation is expressed by Equation (2.1.4b). Several methods were proposed to deal with the quantum nature of nuclei. When the geometry is at the stable equilibrium, the nuclear Schrödinger equation can be described using harmonic approximation. If the system is in a non-equilibrium state and the NQE plays an important role there, one can estimate the nuclear motion across a barrier from the Wentzel-Kramers-Brillouin (WKB) approximation [53].

The eigenvalues of Equation (2.1.4b) give the discrete energy levels of the vibrations, rotations and translations of the molecule. The nuclear wave functions are described as:

$$\psi_{\mathrm{n}}(\boldsymbol{R}) = \psi_{\mathrm{vib}}(\boldsymbol{R})\psi_{\mathrm{rot}}(\boldsymbol{R})\psi_{\mathrm{trans}}(\boldsymbol{R}) \tag{2.3.1}$$

A general potential function $V(\boldsymbol{R})$ for a molecular vibration can be expanded in a Taylor series (here we assume the molecule at bound states, near the minimum $\boldsymbol{R}$=$\boldsymbol{R}^{\boldsymbol{0}}$):

$$V(\boldsymbol{R}) = V(\boldsymbol{R}^0) + \sum_I (\boldsymbol{R}_I - \boldsymbol{R}_I^0)\left(\frac{\partial V}{\partial \boldsymbol{R}_I}\right)_0 + \frac{1}{2}\sum_{I,J}(\boldsymbol{R}_I - \boldsymbol{R}_I^0)(\boldsymbol{R}_J - \boldsymbol{R}_J^0)\left(\frac{\partial^2 V}{\partial \boldsymbol{R}_I \boldsymbol{R}_J}\right)_0 + \cdots \tag{2.3.2}$$

At the vicinity of a stable equilibrium point, the term of $V(\boldsymbol{R}^0)$ and the first derivative are zero, which means:

$$V(\boldsymbol{R}^0) = 0$$

$$\sum_I (\boldsymbol{R}_I - \boldsymbol{R}_I^0)\left(\frac{\partial V}{\partial \boldsymbol{R}_I}\right)_0 = 0$$

The expansion of $V(\boldsymbol{R})$ can be truncated at the second order, as higher terms could be neglected due to the small displacements. So the potential function $V(\boldsymbol{R})$ can be written as the following form, known as the harmonic approximation (see the red curve in Figure 2.3.1):

$$V(\boldsymbol{R}) \approx \frac{1}{2}\sum_{I,J}(\boldsymbol{R}_I - \boldsymbol{R}_I^0)(\boldsymbol{R}_J - \boldsymbol{R}_J^0)\left(\frac{\partial^2 V}{\partial \boldsymbol{R}_I \boldsymbol{R}_J}\right)_0 = \frac{1}{2}k_{\mathrm{f}}(\boldsymbol{R}_I - \boldsymbol{R}_I^0)(\boldsymbol{R}_J - \boldsymbol{R}_J^0) \tag{2.3.3}$$

where k_{f} is the force constant of the vibrational motion, $\boldsymbol{R}$ denotes the internuclear distance, and $\boldsymbol{R}^0$ is the equilibrium internuclear distance. k_{f} is the second derivative of the potential energy and is responsible for the shape of the potential well. A larger k_{f} leads to steeper potential well and shorter bond length.

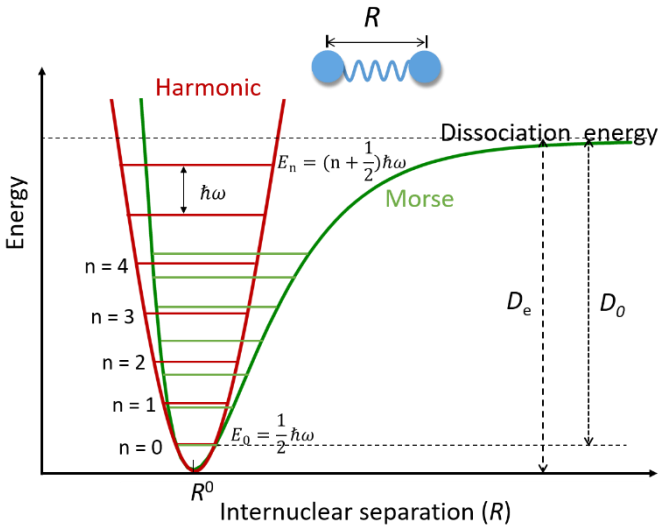

Figure 2.3.1 Harmonic oscillator potential (red curve) and Morse potential [82] (green curve). Energy levels in harmonic oscillator potential are equally spaced by the vibrational levels $\hbar\omega$ (ω is the frequency, $\omega = \sqrt{k/m}$), while in Morse potential the space of energy level decreases as the energy approaches the dissociation energy D_e. The real dissociation energy D_0 is smaller than D_e due to the correction of zero-point energy.

As Figure 2.3.1 shows, the lowest vibrational level is not at zero, but is $\hbar\omega/2$ (ω is the frequency and it equals $\sqrt{k/m}$), this energy is the zero-point energy (ZPE), which is the smallest energy for a quantum mechanical system. ZPE is mass-dependent, heavier isotopes have smaller ZPE than their lighter counterparts. This difference can be used to separate isotopes, such as in kinetic quantum sieving (KQS) [22-33].

2.3.2 Quantum Tunneling

When a system is in a non-equilibrium state, the motion of nuclei can be reflected with quantum tunneling, which is another NQE. Quantum tunneling was firstly discovered by F. Hund while investigating the ground state of the double-well potential [83] in 1927. In the same year, L. Mandelstam and M. Leontovich independently proved the existence of quantum tunneling [84]. In general, quantum tunneling allows particles to

tunnel through an energy barrier that is higher than their kinetic energies, which violates the principles of classical mechanics. Quantum tunneling has been observed in many processes, especially in the proton-involved systems [85, 86].

The wave-particle nature yields the difference between classical and quantum mechanics. According to the Heisenberg uncertainly principle [87], it is impossible to determine a particle's position and its momentum components simultaneously, which indicates that there is no probability of exactly zero for a particle. In other words, for a given particle, the probability of its existence on the other side of a finite potential energy hill is non-zero, this phenomenon is known as quantum tunneling.

Figure 2.3.2 depicts the scenario of quantum tunneling. In classical mechanics, the electron (green sphere in Figure 2.3.2) with low kinetic energy E ($E < U_{max}$) is repelled by the wall of potential well, as the electron does not have enough energy to overcome the high energy barrier $U_{max.}$ In quantum mechanics, however, quantum tunneling allows the electron to "tunnel" through the energy barrier and appear on the other side.

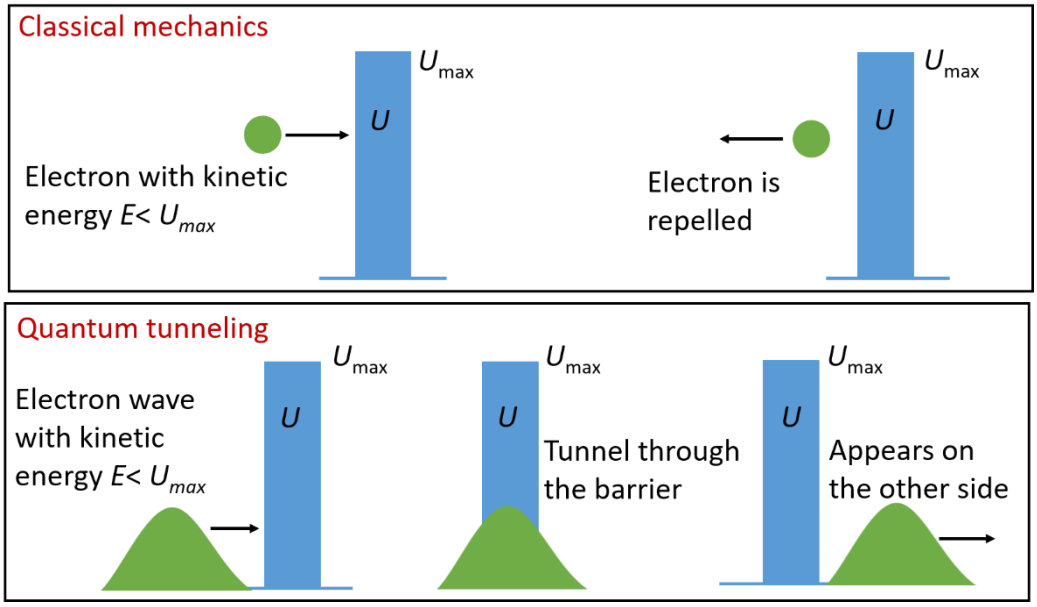

Figure 2.3.2 Schematics of classical mechanics (top) and quantum tunneling (bottom) for an electron with lower kinetic energy E than the maximum height of the energy barrier U_{max}. In classical mechanics, the particle turns back if its energy is less than

U_{max}. In quantum mechanics, quantum tunneling allows the particle tunnel through the barrier even if it has smaller energy than U_{max}.

Three conditions must be fulfilled in quantum tunneling: 1) the height of the energy barrier must be finite and the width of the PES must be narrow; 2) the kinetic energy E of the particle is smaller than the maximum height of the potential energy U_{max} ($E < U_{max}$); 3) the particles must have wave properties, which means quantum tunneling solely applies to microscopic systems, such as protons and light atoms, but is not applicable to macroscopic objects.

There is a finite probability for a particle to tunnel through a barrier, this transmission probability depends on the height and width of the potential barrier, as well as the mass of the particle. Calculating the transmission probability of quantum tunneling is important for its applications. One of the most common approaches to obtain the transmission probability of quantum tunneling is the Wentzel-Kramers-Brillouin (WKB) approximation [53].

Wentzel-Kramers-Brillouin (WKB) approximation

WKB approximation [53] was proposed by the physicists G. Wentzel, H. Kramers and L. Brillouin in 1926.[1] It is often employed to obtain tunneling coefficients in one-dimensional (1D) problems, yet it can also be applied to three-dimensional (3D) symmetric problems [88, 89].

Assuming a slowly varying potential, the wave function of the Schrödinger equation can be written as:

$$\psi(x) = A\exp(\pm ikx) \tag{2.3.4}$$

where k is the wavevector with the following form:

[1] In 1923, mathematician H. Jeffreys had developed a general approach for the approximations to a class of differential equations including Schrödinger equation. Therefore, WKB approximation is also referred to as "JWKB approximation" in some references.

$$k = \frac{2\pi}{\lambda} = \sqrt{\frac{2m(E-U)}{\hbar^2}} \tag{2.3.5}$$

If potential U changes slowly with x, two scenarios need to consider, i.e. $E > U$ and $E < U$. For each case, $k(x)$ can be expressed by:

$$k(x) = \sqrt{\frac{2m\big(E-U(x)\big)}{\hbar^2}} \quad \text{if } E > U(x) \tag{2.3.6}$$

$$k(x) = -i\sqrt{\frac{2m(U(x)-E)}{\hbar^2}} \quad \text{if } E < U(x) \tag{2.3.7}$$

the wave function solution of the Schrodinger equation is expressed as:

$$\Psi(x) = A\exp(i\phi(x)) \tag{2.3.8}$$

where $\phi(x) = xk(x)$. If the potential is constant, $\phi(x) = \pm kx$, which means the phase changes linearly with x. If the potential varies slowly, $\phi(x)$ should also slowly vary from the linear scenario.

According to Schrödinger equation:

$$-\frac{\hbar^2}{2m}\frac{\partial^2}{\partial x^2}\Psi(x) + U(x)\Psi(x) = E\Psi(x) \tag{2.3.9}$$

Plugging Equation (2.3.7) and Equation (2.3.8) into Equation (2.3.9), the following form is obtained:

$$i\frac{\partial^2\phi}{\partial x^2} - \left(\frac{\partial\phi}{\partial x}\right)^2 + \big(k(x)\big)^2 = 0 \tag{2.3.10}$$

The WKB approximation within the assumption that the potential is varying slowly, so $k(x)$ and $\phi(x)$ should also vary slowly. The 0th order and the 1st order of WKB approximation are expressed by:

$$\Psi(\mathrm{x}) = \exp\left\{i(\pm\int k(x)dx + C_0)\right\} \tag{2.3.11}$$

$$\Psi(\mathrm{x}) = \exp\left\{ i(\pm \int \sqrt{\left(k(x)\right)^2 \pm i\frac{\partial}{\partial x}k(x)}dx + C_1) \right\} \tag{2.3.12}$$

In a rectangular potential $U(x)$ with the width of L, as shown in Figure 2.3.3(a), the tunneling probability T is the ratio of the transmitted intensity to the incident intensity:

$$T = \frac{\Psi^*(L)\Psi(L)}{\Psi^*(0)\Psi(0)} \tag{2.3.13}$$

where $\Psi(\mathrm{x}) = \Psi(0)e^{i(\pm\int k(x)dx + C_1)}$. When quantum tunneling occurs, the kinetic energy E should be smaller than U, which means the form of $k(x)$ is the same as Equation (2.3.7). Therefore, the probability of quantum tunneling for a rectangular potential is expressed by:

$$T = \frac{\Psi^*(L)\Psi(L)}{\Psi^*(0)\Psi(0)} = \exp\left(-2\sqrt{2m(U-E)/\hbar^2}\,L\right) \tag{2.3.14}$$

Similarly, in a 1D potential energy surface, as shown in Figure 2.3.3(b), the transmission coefficient is described as:

$$T(E) = \exp\left\{-\frac{2}{\hbar}\int_{x_1}^{x_2}\sqrt{2m[U(x)-E]}dx\right\} \tag{2.3.15}$$

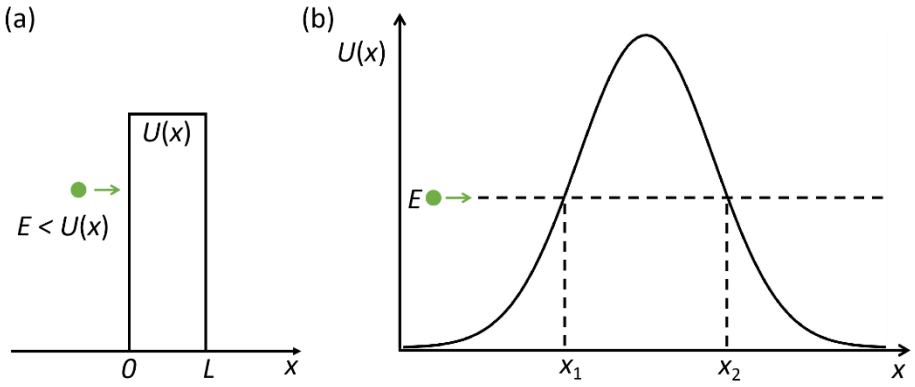

Figure 2.3.3 Schematic of a particle with energy E ($E < U_{max}$) tunnel through a rectangular potential (a) and Gaussian potential (b), respectively.

Equation (2.3.15) is usually used to calculate the transmission probability of tunneling in 1D system. One can see that the particle transmission coefficients decrease exponentially with the mass of particles. This explains, why tunneling is common for nanoscale objects, but negligible for macroscopic objects.

In the WKB approximation, as the potential $U(x)$ is slowly varied in comparison to λ, the fowling condition must be fulfilled:

$$\left|\frac{\partial}{\partial x}k(x)\right| \ll |(k(x))^2|$$

From this condition one can see the 1st order approximation is very close to the 0th order approximation. WKB approximation fails in the points where the kinetic energy E of the particle equals to the potential $U(x)$, the points are called as the turning points, as classical particle will turn around and change direction when its energy E is smaller than $U(x)$. At the turning points, the wave factor $k(x)$ is zero, yet its derivate obviously is not, i.e., the $k(x) = 0$ but $\frac{\partial k(x)}{\partial x} = -i\frac{\partial}{\partial x}(\sqrt{\frac{2m(E-U(x))}{\hbar^2}}) \neq 0$ at the turning points, which apparently does not match the condition of $\left|\frac{\partial}{\partial x}k(x)\right| \ll |(k(x))^2|$. Connection formulas should be applied at the turning points [90]. At all the other regions, WKB approximations works very well.

There are other approaches to describe the quantum nature of nuclei, one of them is the path-integral molecular simulations (PIMD). This method incorporates quantum mechanics into molecular dynamics simulations through Feynman path integrals [91], which essentially maps the quantum system onto a corresponding effective classical system. The basic idea of PIMD is that the wave function is separated into electronic and nuclear part, based on the BO approximation; the nuclei are treated quantum mechanically, each quantum nucleus are mapped onto a classical system—this classical system includes several fictitious particles connected by harmonic springs. The classical system created by this way, although has an increased complexity, can be

solved relatively easily. Interested readers can find further details of PIMD in the Refs. [92, 93].

Several physical phenomena, such as radioactive decay, can be explained by quantum tunneling. The principle of quantum tunneling results in the development in various fields, e.g., tunnel diode [94], scanning tunneling microscope [95] (STM). In this thesis, quantum tunneling is investigated in the process of hydron isotope separation through 2D materials. In Chapter 5 and Chapter 6 of this work, WKB-approximation is employed to calculate transmission coefficients of tunneling by applying Equation (2.3.15).

2.4 Free Energy Calculations

Free energy differences are very important in statistical mechanics, they can help us to estimate whether a reaction can occur spontaneously or it needs input work from the outside. Also, free energy differences are related to the equilibrium constants in chemical processes. In Chapter 4 of this work, the calculated free energy barriers for hydrogen transport in the interstitial space of layered materials give direct and critical information for the possibility of the particles traveling inside these materials. Therefore, in this section, the basic theory of free energy related calculations is introduced.

2.4.1 Free Energy Perturbation Theory

For a system transforming from one thermodynamic state *A* to another *B*, the potential energy functions of these two states *A* and *B* are described by $U_{\mathrm{A}}(\boldsymbol{r}_1, \ldots, \boldsymbol{r}_{\mathrm{N}})$ and $U_{\mathrm{B}}(\boldsymbol{r}_1, \ldots, \boldsymbol{r}_{\mathrm{N}})$. The Helmholtz free energy difference between the two states can be expressed by $\Delta F_{\mathrm{AB}} = F_{\mathrm{A}} - F_{\mathrm{B}}$, where the free energies F_{A} and F_{B} are obtained from their canonical partition functions Q_{A} and Q_{B}, $F_{\mathrm{A}} = -kT\ln Q_{\mathrm{A}}$ and $F_{\mathrm{B}} = -kT\ln Q_{\mathrm{B}}$, the following equations are obtained:

$$Q_{\mathrm{A}}(N,V,T) = C_{\mathrm{N}} \int d^{\mathrm{N}}\boldsymbol{p}\, d^{\mathrm{N}}\boldsymbol{r} \exp\left\{-\beta[\sum_{i=1}^{N} \frac{\boldsymbol{p}_i^2}{2m_i} + U_{\mathrm{A}}(\boldsymbol{r}_1, \ldots \boldsymbol{r}_{\mathrm{N}})]\right\} = \frac{Z_{\mathrm{A}}(N,V,T)}{N!\,\lambda^{3\mathrm{N}}}$$

$$Q_{\mathrm{B}}(N,V,T) = C_{\mathrm{N}} \int d^{\mathrm{N}}\boldsymbol{p}\, d^{\mathrm{N}}\boldsymbol{r} \exp\left\{-\beta[\sum_{i=1}^{N} \frac{\boldsymbol{p}_i^2}{2m_i} + U_{\mathrm{B}}(\boldsymbol{r}_1, \ldots \boldsymbol{r}_{\mathrm{N}})]\right\} = \frac{Z_{\mathrm{B}}(N,V,T)}{N!\,\lambda^{3\mathrm{N}}}$$

(2.4.1)

The free energy difference ΔF_{AB} can, thus, be expressed by:

$$\Delta F_{\mathrm{AB}} = F_{\mathrm{A}} - F_{\mathrm{B}} = -kT \ln\left(\frac{Q_{\mathrm{B}}}{Q_{\mathrm{A}}}\right) = -kT \ln\left(\frac{Z_{\mathrm{B}}}{Z_{\mathrm{A}}}\right) \tag{2.4.2}$$

where Z_{A} and Z_{B} are the configurational partition functions of the two states *A* and *B*:

$$Z_{\mathrm{A}} = \int d^N \boldsymbol{r} e^{-\beta U_A(\boldsymbol{r}_1, \ldots \boldsymbol{r}_{\mathrm{N}})}$$

$$Z_{\mathrm{B}} = \int d^N \boldsymbol{r} e^{-\beta U_{\mathrm{B}}(\boldsymbol{r}_1, \ldots \boldsymbol{r}_{\mathrm{N}})} \tag{2.4.3}$$

The Equation (2.4.2) could be calculated straightforwardly if it can be described by a phase space average. To this end, assume inserting unity into the description for Z_{B} as:

$$\begin{aligned} Z_{\mathrm{B}} &= \int d^N \boldsymbol{r} e^{-\beta U_{\mathrm{B}}(\boldsymbol{r}_1, \ldots \boldsymbol{r}_{\mathrm{N}})} \\ &= \int d^N \boldsymbol{r} e^{-\beta U_{\mathrm{B}}(\boldsymbol{r}_1, \ldots \boldsymbol{r}_{\mathrm{N}})} e^{-\beta U_{\mathrm{A}}(\boldsymbol{r}_1, \ldots \boldsymbol{r}_{\mathrm{N}})} e^{\beta U_{\mathrm{A}}(\boldsymbol{r}_1, \ldots \boldsymbol{r}_{\mathrm{N}})} \\ &= \int d^N \boldsymbol{r} e^{-\beta U_{\mathrm{A}}(\boldsymbol{r}_1, \ldots \boldsymbol{r}_{\mathrm{N}})} e^{-\beta (U_{\mathrm{B}}(\boldsymbol{r}_1, \ldots \boldsymbol{r}_{\mathrm{N}}) - U_{\mathrm{A}}(\boldsymbol{r}_1, \ldots \boldsymbol{r}_{\mathrm{N}}))} \end{aligned} \tag{2.4.4}$$

So the ratio of $Z_{\mathrm{B}}/Z_{\mathrm{A}}$ can be written as:

$$\begin{aligned} \frac{Z_{\mathrm{B}}}{Z_{\mathrm{A}}} &= \frac{1}{Z_{\mathrm{A}}} \int d^N \boldsymbol{r}\, e^{-\beta U_{\mathrm{A}}(\boldsymbol{r}_1, \ldots \boldsymbol{r}_{\mathrm{N}})} e^{-\beta \left(U_{\mathrm{B}}(\boldsymbol{r}_1, \ldots \boldsymbol{r}_{\mathrm{N}}) - U_{\mathrm{A}}(\boldsymbol{r}_1, \ldots \boldsymbol{r}_{\mathrm{N}})\right)} \\ &= \langle \exp(-\beta (U_{\mathrm{B}}(\boldsymbol{r}_1, \ldots \boldsymbol{r}_{\mathrm{N}}) - U_{\mathrm{A}}(\boldsymbol{r}_1, \ldots \boldsymbol{r}_{\mathrm{N}})) \rangle_A \end{aligned} \tag{2.4.5}$$

where the symbol $\langle \cdots \rangle_{\mathrm{A}}$ means an average taken in regards to the canonical configurational distribution of state *A*.

Plugging Equation (2.4.5) into Equation (2.4.2) gives

$$\Delta F_{\mathrm{AB}} = -kT\ln\langle e^{-\beta(U_{\mathrm{B}}-U_{\mathrm{A}})}\rangle_A \tag{2.4.6}$$

Equation (2.4.6) is the well-known free energy perturbation formula [96]. One needs to keep in mind, however, that this formula works well only when the potential energy between state *A* and state *B* does not differ significantly. If the potential energy difference of $U_{\mathrm{A}}—U_{\mathrm{B}}$ is very large, the exponential term will become negligibly small.

2.4.2 Collective Variables

In a system, a small set of generalized coordinates can characterize the progress of some chemical, mechanical or thermodynamical processes, these generalized coordinates are usually referred to as *collective variables*, *reaction coordinates*, or *order parameters*, depending on the contexts and the systems. Herein, *collective variables* (CV) will be used.

A great number of methods [97] were developed to enhance sampling along the preselected collective variables (CVs). The methods are aimed to create the probability distribution function of a subset of *n* collective variables in a system. If these collective variables are obtained from a transformation of the Cartesian coordinates to generalized coordinates $q_\alpha = f_\alpha(\boldsymbol{r}_1, \ldots, \boldsymbol{r}_{\mathrm{N}})$, $\alpha = 1, \ldots, n$, then the probability density those *n* variables will have values of $q_\alpha = s_\alpha$ in the canonical ensemble is given by:

$$P(s_1, \ldots, s_{\mathrm{n}}) = \frac{C_{\mathrm{N}}}{Q(N,V,T)} \int d^N\boldsymbol{p} d^N\,\boldsymbol{r} e^{-\beta H(\boldsymbol{r},\boldsymbol{p})} \prod_{\alpha=1}^{n} \delta(f_{\mathrm{a}}(\boldsymbol{r}_1, \ldots \boldsymbol{r}_{\mathrm{N}}) - s_\alpha) \tag{2.4.7}$$

where δ-functions are introduced to fix the reaction coordinates $q_1, \ldots q_{\mathrm{N}}$ at $s_1, \ldots, s_n$. Once $P(s_1, \ldots, s_{\mathrm{n}})$ is obtained, the free energy hypersurface in the reaction coordinates can be written as:

$$\mathrm{F}(s_1, \ldots, s_{\mathrm{n}}) = -kT\ln P(s_1, \ldots, s_{\mathrm{n}}) \tag{2.4.8}$$

Note that although the CVs are quite powerful in getting chemical information, they should be carefully chosen and used, otherwise some erroneous predictions might occur. For example, poorly chosen CVs could lead to wrong free energy barriers. Readers can find further insight about choosing the reasonable sampling approaches in the textbook of *Statistical Mechanics: Theory and Molecular Simulation* by M. Tuckerman [98].

2.4.3 Metadynamics

In molecular dynamics, it is usually not possible to get the free energy difference through a straightforward method, due to the high energy barriers or other sampling issues. A standard solution to this problem is to apply an external biased potential that forces the system to search the regions of high free energy, and this is the main idea of Metadynamics (MetaD). MetaD was originally proposed by Laio and Parrinello in 2002 [97] and is widely employed to obtain the free energy surfaces (FES) of reactions. In MetaD, the energy basins are “filled in” with a time-dependent potential that depends on the history of a system’s trajectory. Once an energy basin is filled, it will drive the system into the next energy basin that is subsequently filled, until the whole energy landscape turns flat. After reaching this state, the free energy surface can be constructed from the accumulated time-dependent potential. The schematic procedure of MetaD is shown in Figure 2.4.1. The position of a system (represented by a green point in an unknown FES) is as a function of CV.

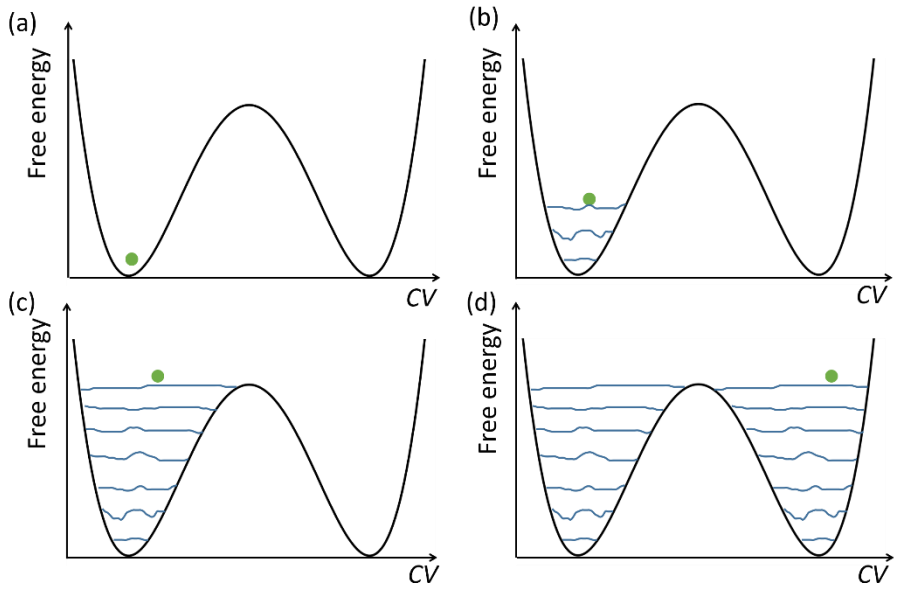

Figure 2.4.1 The schematic procedure of MetaD. (a) The simulation reaches the first minimum (left basin). (b) A biased potential (in blue) is being added to the surroundings of the first minimum. (c) The biased potential is large enough to force the system to move to the second minimum (right basin). (d) At the end, the entire energy landscape turns flat.

One can consider the probability distribution function in Equation (2.4.9), $P(s_1, \dots, s_n)$ as an ensemble average expressed by:

$$P(s_1, \dots, s_n) = \left(\prod_{\alpha=1}^{n} \delta(f_\alpha(\boldsymbol{r}_1, \dots \boldsymbol{r}_N) - s_\alpha) \right) \tag{2.4.9}$$

The phase space average can, therefore, be replaced by a time average over a trajectory (assuming the ergodic dynamics):

$$P(s_1, \dots, s_n) = \lim_{\mathcal{T}\to\infty} \frac{1}{\mathcal{T}} \int_0^{\mathcal{T}} dt \prod_{\alpha=1}^{n} \delta(f_\alpha(\boldsymbol{r}_1(t), \dots \boldsymbol{r}_N(t)) - s_\alpha) \tag{2.4.10}$$

A δ-function is introduced here, which is described as the limit of a Gaussian function, when the height goes towards infinity and the width goes to 0,

$$\delta(x - a) = \lim_{\sigma\to\infty} \frac{1}{\sqrt{2\pi\sigma^2}} \exp\left\{ \frac{-(x-a)^2}{2\sigma^2} \right\} \tag{2.4.11}$$

where x is the configurational variables and a is a hard-to-reach point in CV space.

With Equation (2.4.11), Equation (2.4.10) can be reorganized as:

$$P(s_1, \dots, s_n) = \lim_{\mathcal{T}\to\infty} \lim_{\Delta s\to\infty} \frac{1}{\sqrt{2\pi\Delta s^2}\mathcal{T}} \int_0^{\mathcal{T}} dt \prod_{\alpha=1}^{n} \exp\left[-\frac{(s_\alpha - f_\alpha(\boldsymbol{r}_1(t), \dots, \boldsymbol{r}_\mathrm{N}(t)))^2}{2\Delta s^2}\right] \tag{2.4.12}$$

Equation (2.4.12) indicates an approximation to $P(s_1, \dots, s_n)$ for each finite $\mathcal{T}$ and Δs, and it turns increasingly accurate when the Gaussian width Δs decreases and $\mathcal{T}$ increases. For numerical evaluation, the integral in Equation (2.4.12) can be treated as discrete sum, therefore, the approximation can be written as:

$$P(s_1, \dots, s_n) \approx \frac{1}{\sqrt{2\pi\Delta s^2}\mathcal{T}} \sum_{k=0}^{\mathcal{N}-1} \exp\left[-\sum_{\alpha=1}^{n} \frac{(s_\alpha - f_\alpha(\boldsymbol{r}_1(k\Delta t), \dots, \boldsymbol{r}_\mathrm{N}(k\Delta t)))^2}{2\Delta s^2}\right] \tag{2.4.13}$$

Equation (2.4.13) shows a proper bias potential that can be added to the original potential $U(\boldsymbol{r}_1, \dots, \boldsymbol{r}_\mathrm{N})$ to assist the system sample to its free energy hypersurface, and meanwhile, it allows for a direct rebuilding of the surface from the dynamics straightforwardly. The form of a bias potential can be written as:

$$U_\mathrm{G}(\boldsymbol{r}_1, \dots, \boldsymbol{r}_\mathrm{N}, t) = W \sum_{t=\tau G, 2\tau G, \dots,} \exp\left[-\sum_{\alpha=1}^{n} \frac{(f_\alpha(\boldsymbol{r}) - f_\alpha(\boldsymbol{r}_\mathrm{G}(t)))^2}{2\Delta s^2}\right] \tag{2.4.14}$$

where $\boldsymbol{r} \equiv \boldsymbol{r}_1, \dots, \boldsymbol{r}_\mathrm{N}$, $\mathbf{r}_\mathrm{G}(t)$ represents the time evolution of the complete set of coordinates up to the time t under the potential $U + U_\mathrm{G}$, τ_G is the time interval, W and Δs are the height and width of each Gaussian, respectively. The reason to use this bias potential is to add Gaussians of height W and width Δs to the potential energy at intervals τ_G, so when the time increases, these Gaussians will accumulate. Assume a system starts in a deep basin of the PES, by applying the above method, this basin will be "filled in" by the Gaussians, as a result, the system will be lifted up towards the energy barrier until it is able to cross the energy barrier and arrive the next basin.

If the collective variables move with a relatively slow speed, then they move swiftly on the potential of mean force surface $F(q_1, \cdots, q_n)$ instead of on the bare potential energy surface. Therefore, if the extra Gaussians were added slowly enough, when time increases, U_G takes on the shape of $-F(q_1, \cdots, q_n)$, for it arrives the maxima while A is in minima, and vice versa. So for a given long trajectory $\boldsymbol{r}_G(t)$ generated by the bias potential, the free energy surface can be constructed as:

$$F(q_1, \cdots, q_n) \approx -W \sum_{t=\tau G, 2\tau G, \ldots,} \exp\left[-\sum_{\alpha=1}^{n} \frac{(q_\alpha - f_\alpha(\boldsymbol{r}_G(t)))^2}{2\Delta s^2}\right] \qquad (2.4.15)$$

So far, MetaD has been widely used in many fields to enhance sampling in molecular dynamic simulations. However, it still needs to be improved on some aspects, particularly for example, MetaD has two major drawbacks: first, it usually suffers a poor convergence; second, it could risk of being pushed into the regions of configurational space that might not be physically meaningful when continuing a run. In order to solve these problems, Barducci et al. [99] came up with the improved theory by using an adaptive-bias, known as well-tempered metadynamics (WT-MetaD), which solves the convergence issue in MetaD and allows the exploration of the FES being limited to the physically meaningful regions.

Generally speaking, in WT-MetaD, by adding a history-dependent potential $U(\mathrm{s}, \mathrm{t})$, the FES can be obtained as:

$$\tilde{F}(s,t) = -\frac{T+\Delta T}{\Delta T} U(s,t) = -(T+\Delta T)\ln\left(1+\frac{\omega N(s,t)}{\Delta T}\right) \qquad (2.4.16)$$

where ω is the dimension of energy rate, $N(s,t)$ is the histogram from the biased simulation, ΔT is the temperature parameter. By adding ΔT, the barrier crossing can be increased and facilitate the search in the CVs space. Besides, a finite value of ΔT will spontaneously limit the exploration area in the FES around the order T+ΔT, which is more reasonable and physically meaningful. In short, WT-MetaD can avoid the risk of

overfilling of the free energy regions in the simulations and, therefore, gives more accurate FES. In Chapter 4 of this work, WT-MetaD is employed to obtain the free energy barriers of hydrogen particle transport inside layered materials.

2.5 Non-Arrhenius Behavior

The activation energy is the minimum energy that compounds must overcome to result in the occurrence of a reaction, it gives straightforward information of a process. In this work, we would like to estimate the effective activation energy barrier in the quantum tunneling involved systems. To be more preciously, we want to calculate the activation energies in the process of proton isotope permeating through graphene monolayer.

For a given reaction, its rate constant k_{r} is expressed by the empirical Arrhenius equation:

$$k_{\mathrm{r}} = A \exp(-E_{\mathrm{a}}/k_{\mathrm{B}}T) \tag{2.5.1}$$

where A is the pre-exponential factor, E_{a} is the activation energy, k_{B} is the Boltzmann constant, and T is temperature. The natural logarithm form of Equation (2.5.1) is:

$$\ln(K) = -\frac{E_{\mathrm{a}}}{k_{\mathrm{B}}}\left(\frac{1}{T}\right) + \ln(A) \tag{2.5.2}$$

Plotting $\ln(K)$ versus $1/T$ gives the so-called Arrhenius plot (see the black line in Figure 2.5.1). The slope of the Arrhenius plot is $-E_{\mathrm{a}}/k_{\mathrm{B}}$, from which, the activation energy E_{a} for the reaction can be determined.

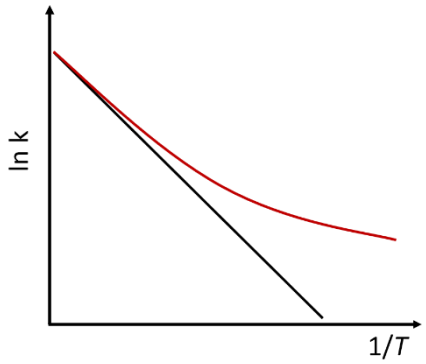

Figure 2.5.1 Linear (black) and non-linear (red) Arrhenius plots.

Arrhenius equation has been successfully applied for describing rate constants and activation energies, nonetheless, it cannot be generally applied to any reaction. As an empirical equation instead of a fundamental physical equation, Arrhenius equation is valid only for classical cases. If quantum effects play a considerable role in the reaction, Arrhenius plot will exhibit clear curvature due to quantum effects, which is referred to as the non-Arrhenius behavior (see the red curve in Figure 2.5.1). In such cases, the Arrhenius equation could fail and result in inaccurate activation energies. In Section 5.5, we will explore the effective activation energy in the process of the proton isotope permeating through graphene monolayer. Since quantum tunneling plays a significant role in such process, the non-Arrhenius behavior could take place, from which we estimate the upper limit of energy barrier of a reaction, where the Arrhenius equation is applicable.

.

3. The Fundamental Properties of Layered and 2D Materials

As one of the most well-known two-dimensional (2D) materials, graphene was first exfoliated in 2004 experimentally [100], which led to the Nobel Prize in Physics in 2010 for A. K. Geim and K.S. Novoselov. In the past decade, graphene has been investigated intensively due to its outstanding properties. Other family members of 2D materials beyond graphene, for instance, hexagonal boron nitride (*h*-BN) [101-103], transition metal dichalcogenides (TMDCs) [104-110], phosphorene [111-114], also have fascinating properties and potential applications in various fields, such as electronics, gas molecule separation, and catalysis.

The bulk forms of these materials exist as layered solids, which are connected by the weak van-der-Waals (vdW) forces between individual layers [115], this allows layered materials to be exfoliated into 2D monolayers. In this work, both layered materials and their exfoliated 2D monolayers will be studied. Therefore, in this chapter, we introduce the basic properties of the representative materials investigated in the thesis.

3.1 Layered Materials

Layered materials are widespread on our planet since ancient time [116], they are held together by the weak vdW interactions between the adjacent monolayer planes, creating the interstitial space which is referred to as vdW gap. For this reason, such materials are categorized as the group of "vdW crystals". A large number of materials, such as graphite, hexagonal boron nitride (*h*-BN), and molybdenum disulfide (MoS_2), belong to vdW layered materials (see Figure 3.1.1).

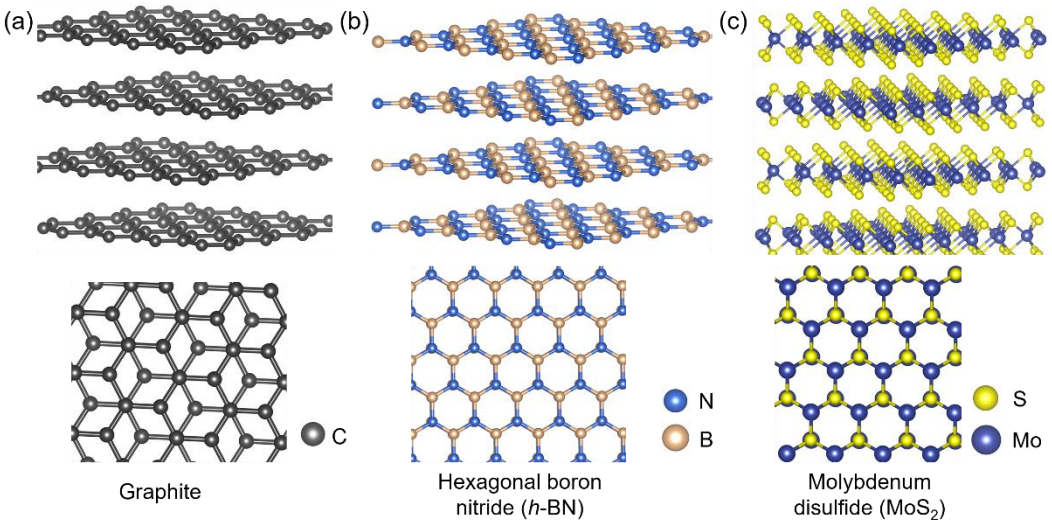

Figure 3.1.1 Structural modes of layered materials: (a) graphite, (b) hexagonal boron nitride (*h*-BN), and (c) molybdenum disulfide (MoS_2).

Graphite is one of the most common layered materials. It consists of stacked carbon layers with honeycomb lattice, the distance between the adjacent layers is about 3.30 Å. Its sister material, hexagonal boron nitride (*h*-BN), also known as "white graphite", has similar hexagonal lattice, and slightly larger interlayer distance of 3.33 Å. Transition metal dichalcogenide molybdenum disulfide (MoS_2) also belongs to layered materials, with a plane of molybdenum (Mo) atoms sandwiched between two planes of sulfur (S) atoms. The interstitial space of these layered materials provide them an extra channels for remarkable chemistry, for example, in Chapter 4 of this work, layered *h*-BN, MoS_2, and graphite are studied for transporting hydrogen particles through their interstitial space.

3.2 Two-dimensional Materials

3.2.1 Graphene

Graphene, formed by carbon atoms arranged in planar hexagonal rings, was exfoliated by A. K. Geim and K. S. Novoselov in 2004 [100], through mechanically exfoliated approach from its mother material—bulk graphite (see Figure 3.2.1). As the first 2D

material, the atomic thickness of graphene endows itself being the thinnest membrane and is promising in various applications, e.g., in electrochemical energy storage [117], optoelectronics [118], and electronics [119].

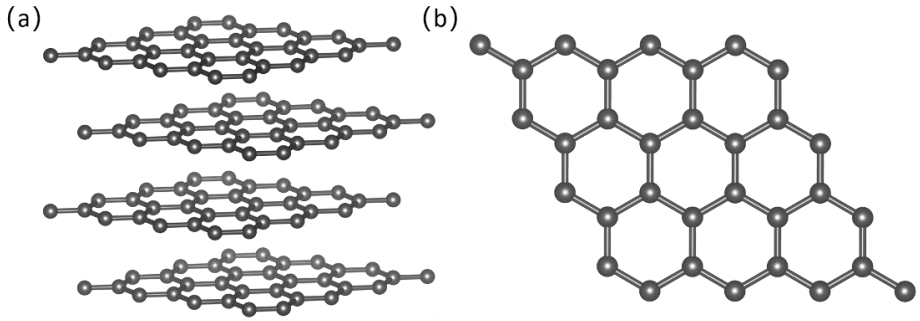

Figure 3.2.1 Bulk graphite (a) and the exfoliated graphene monolayer (b).

The basis of graphene's lattice consists of two carbon atoms, see Figure 3.2.2. In graphene, each carbon atom is 1.42 Å apart from its three nearest neighbors, which makes the lattice constant a_0 2.46 Å. The hexagonal Bravais lattice (see Figure 3.2.2a) can be described by:

$$a_1 = a_0\left(\frac{\sqrt{3}}{2}, \frac{1}{2}\right) \quad a_2 = a_0\left(\frac{\sqrt{3}}{2}, -\frac{1}{2}\right) \tag{3.1.1}$$

The first Brillouin zone (BZ) is shown in Figure 3.2.2b, with a reciprocal lattice vectors given by:

$$b_1 = \frac{2\pi}{a_0}\left(\frac{\sqrt{3}}{3}, 1\right) \qquad b_2 = \frac{2\pi}{a_0}\left(\frac{\sqrt{3}}{3}, -1\right) \tag{3.1.2}$$

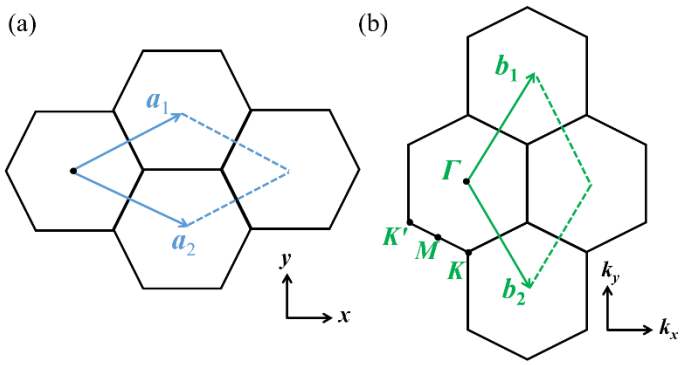

Figure 3.2.2 (a) The standard honeycomb lattice of graphene, with the unit cell contains two carbon atoms defined by two lattice vectors a_1 and a_2. (b) Reciprocal lattice with lattice vectors b_1 and b_2.

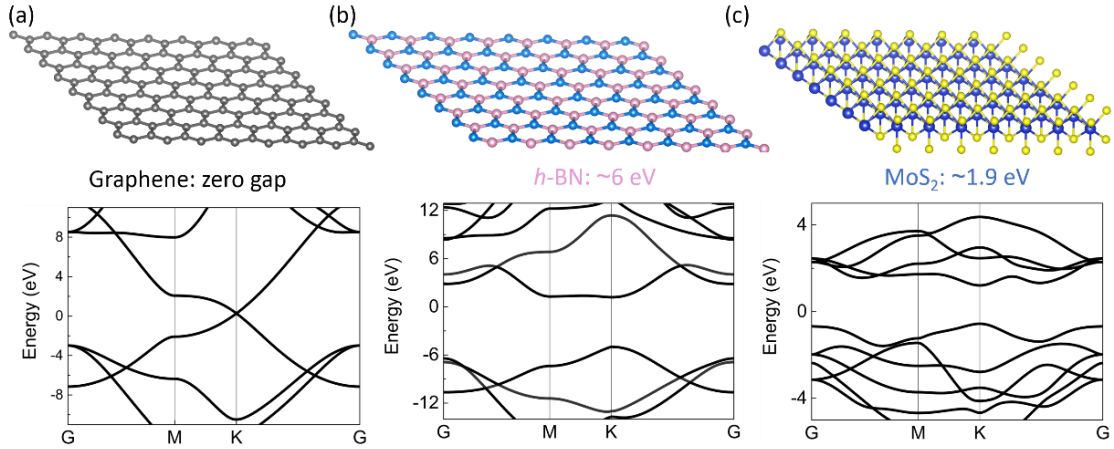

Figure 3.2.3 Band structure of (a) graphene, (b) *h*-BN, and (c) MoS_2 monolayers. Monolayer of *h*-BN and MoS_2 will be introduced in Sections 3.2.2 and 3.2.3, respectively.

Graphene is a gapless semi-metal with distinctive band structure (see Figure 3.2.3a). Its valence band (π) and conduction (π*) bands meet each other at the *K* and *K'* points in the BZ, these points are called as the Dirac points [120]. Close to the Dirac points, within the low-energy excitations, a liner dispersion relation is observed [120], see Figure 3.2.4. This conical and liner dispersion indicates that electrons behave like massless Dirac fermions, moving nearly at the speed of light (300 times smaller) [120], which brings remarkable properties for graphene.

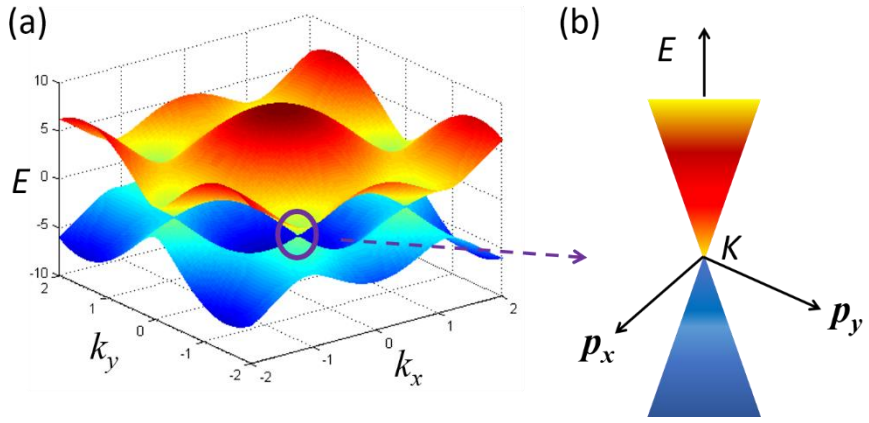

Figure 3.2.4 (a) Energy dispersion of π electrons in graphene; (b) Zoom in of one of the Dirac points.

The experimentally available graphene is usually produced from mechanical exfoliation [121] or chemical vapour deposition (CVD) [122-124] procedure. The exfoliated graphene is normally defect-free or has very few defects [125], but the technique itself prevents the usage of large-scale, because the size of the exfoliated graphene is limited to hundreds of microns. CVD method is considered as the most promising approach to produce large area and continuous graphene [123], yet the CVD produced graphene membranes usually have defects. For example, one of the most common defects, topological Stone-Wales (SW(55-77)) defect [126, 127], is usually observed in the CVD produced graphene membranes, as shown in Figure 3.2.5.

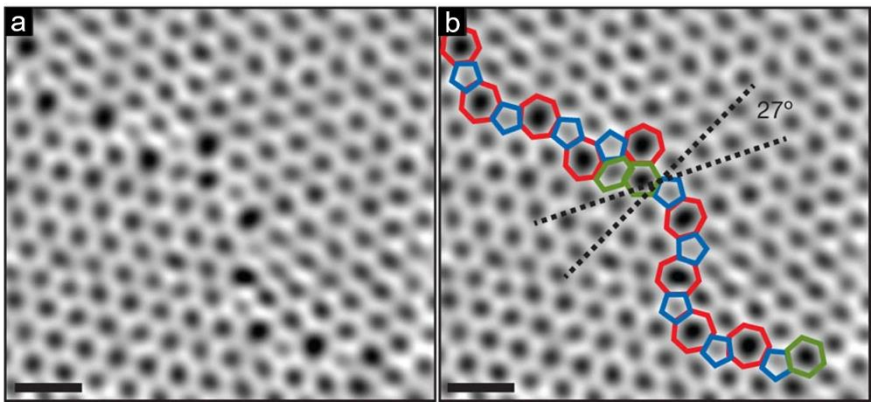

Figure 3.2.5 (a) Two grains in CVD graphene intersect with a 27° relative rotation. An aperiodic line of defects stitches the two grains together. (b) The image from (a) with the pentagons (blue), heptagons (red) and distorted hexagons (green) of the grain boundary outlined. Scale bars are 5 Å. Adapted from Ref.[127].

Defects could significantly affect electronic and chemical properties of graphene [128]. In this work, we present detailed discussions about the influence of topological SW(55-77) defects to the permeation and separation of hydron isotopes through graphene, which will be given in Chapter 5.

3.2.2 Hexagonal boron nitride

Hexagonal boron nitride (*h*-BN) [101-103] is a structural analogue of graphene. Its unit-cell is occupied by a boron and a nitrogen atom, resulting in a honeycomb lattice (see Figure 3.2.6) with the lattice constant of 2.50 Å. Like graphite, bulk *h*-BN is a layered material, it is hold together by weak vdW forces between individual *h*-BN planes (see Figure 3.2.7), which makes exfoliating layered *h*-BN into monolayers possible [129].

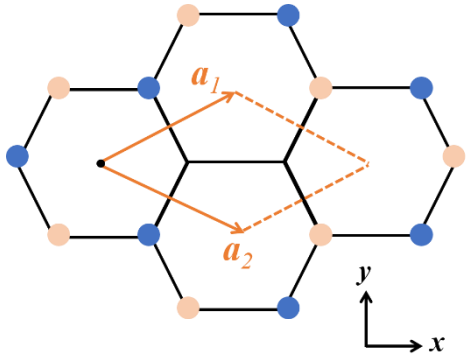

Figure 3.2.6 The lattice of *h*-BN, with the unit cell contains a nitrogen atom and a boron atom defined by two lattice vectors a_1 and a_2.

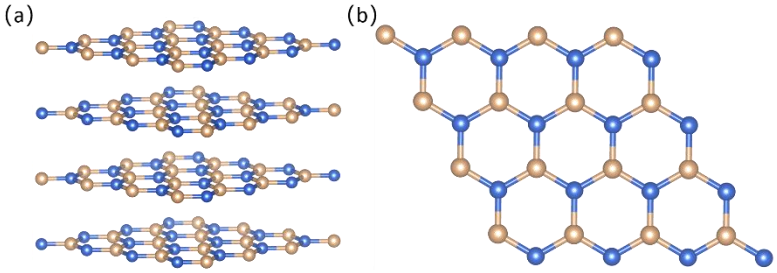

Figure 3.2.7 (a) Layered *h*-BN with the most stable AA' stacking (N over B) mode. (b) Monolayer of *h*-BN.

Layered *h*-BN has different stacking modes, the most stable configuration is AA' stacking (N over B) [130]. Yet, it usually exhibits low-energy shearing mode to other stackings, such as A'B (staggered N over N), as shown in Figure 3.2.8. The energy barrier for the interlayer shear is rather small [130, 131], even smaller than k_BT at 300 K (around 25 meV), therefore well accessible at room temperature.

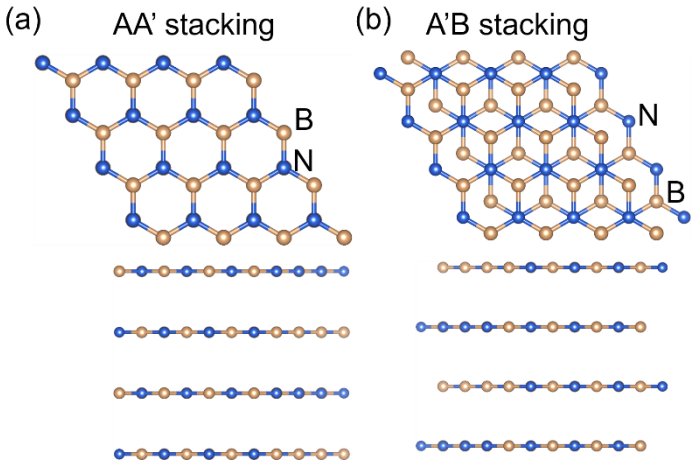

Figure 3.2.8 h-BN stackings of AA' (a) and A'B (b).

Monolayers of *h*-BN can be synthesized through CVD on polycrystalline Cu and Pt foils [134-137]. Through TEM and conductive AFM studies, it is suggested that no defects or pinholes exist in *h*-BN [138]. The band structure of *h*-BN is shown in Figure 3.2.3b, from which one can see that *h*-BN monolayer is an insulator, with a direct bandgap of about 6.0 eV [139] at the high-symmetry point *K*.

Layered *h*-BN is studied in Chapter 4 of this thesis, to investigate the transport of hydrogen species (charged H^+ and neutral H atom) inside its interstitial space. Monolayer of *h*-BN is explored in Chapter 5, where the focus is separating hydron isotopes through 2D graphene and *h*-BN monolayers.

3.2.3 Molybdenum Disulfide

Molybdenum disulfide (MoS_2) is a typical layered material that belongs to the family of transition metal dichalcogenides (TMDs), it was firstly studied as early as in 1923

[104], but became a hot topic only since 2010 [140]. The excellent electronic, optical, mechanical, chemical, and thermal properties of MoS_2 render itself being significant in various fields, for instance, photodetectors [141, 142], solar cells [143, 144], nano-photonics [145, 146] and chemical sensors [147-149].

MoS_2 monolayer is composed of a plane of molybdenum atoms sandwiched between two planes of sulfur atoms (see Figure 3.2.9), with the lattice constant of 3.16 Å [150]. It is a semiconductor whose band gap varies with the number of layers: bulk MoS_2 has an indirect gap of 1.29 eV up to 1.9 eV with decreasing thickness [151], while monolayer MoS_2 is transferred into a direct gap semiconductor with a band gap of 1.88 eV [140, 152], see Figure 3.2.3c.

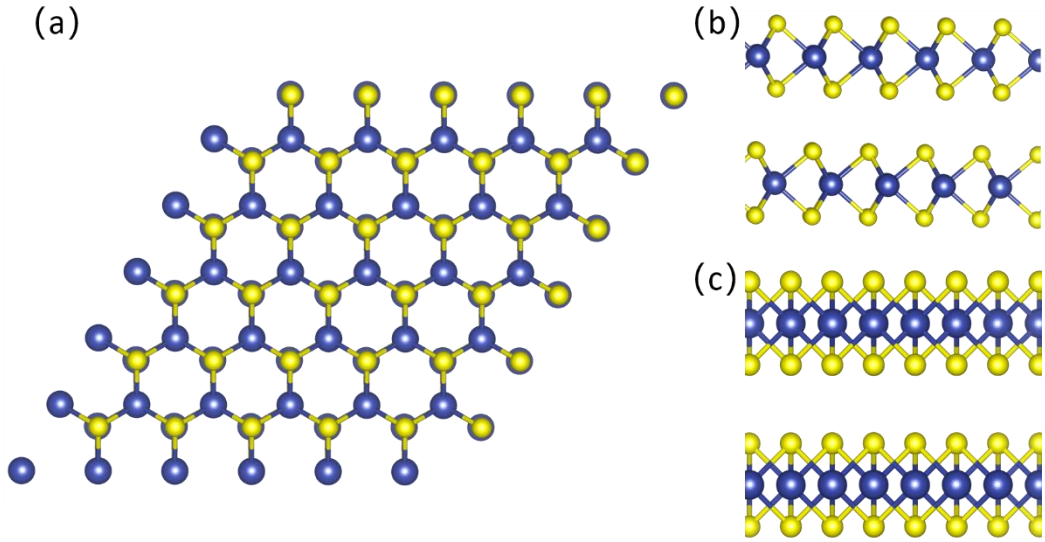

Figure 3.2.9 Bilayer structure of MoS_2 with top view (a) and side views (b and c).

The experimentally available MoS_2 monolayer can be produced through exfoliation or chemical vapor deposition (CVD) approaches [153], yet various types of defects usually exist in MoS_2 membranes, among which, the most common defect is the sulfur atom vacancy [154]. In Chapter 4 of this work, we study the transport of hydrogen particles in the interstitial space of layered MoS_2, both cases of perfect and defective MoS_2 (with atomic sulfur vacancy) will be investigated.

Part I

Hydrogen Particle Transport in the Interstitial Space of Layered Materials

4. Hydrogen Transport in Interstitial Space of Layered *h*-BN, MoS_2 and Graphite

Recent experiment [34] have demonstrated transport and separation of hydrogen isotopes through the van der Waals gap in hexagonal boron nitride and molybdenum disulfide bulk layered materials. However, the experimental setup could not distinguish if the transported particles were protons (H^+) or protiums (H atoms). Herein, in this chapter, we identify the species of transported hydrogen particles inside layered materials and investigate their transport mechanisms. We show that protium atoms, rather than protons, are transported through the van der Waals gap. The diffusion mechanism of both protons and protiums involves a hopping process between adjacent layers, which is assisted by low-energy phonon shear modes.

The results presented in this chapter are published in the journal of *Small*, 15(43), 1901722 (2019). I myself performed all numerical calculations, except the WT-MetaD simulations of H^+ inside layered *h*-BN, which was carried out by P. Petkov at the beginning. The manuscript was prepared by myself, with comments and remarks by A. Kuc, P. Petkov, M. Lozada-Hidalgo and T. Heine. Readers will find most parts of the following chapter in the original paper [155]. Reproduced with permission from *Small* **2019,** *15*, 1901722, copyright Wiley-VCH.

4.1 Introduction

Recently, Hu et al. [34] reported hydrogen isotope separation by sieving through the interstitial space of layered bulk materials hexagonal boron nitride (*h*-BN) and molybdenum disulfide (MoS_2). While the difference in the entry barrier of the hydrogen

isotopes into the interstitial space of the layered materials was found to be the driving factor for the isotope separation, there is no conclusive picture yet on the chemical interaction of interstitial hydrogen with the layered materials, and on the transport mechanism through them.

Spatial confinement has a strong impact on the chemical properties of molecules [156-158]. The layers of *h*-BN, MoS_2, and graphene are chemically very stable, and the interlayer interactions impose pressure on the intercalated species [115, 159, 160]. So, the chemistry in the interstitial space of a layered material is expected to be significantly different from the surface-adsorbed counterpart.

The experimental setup in the work of Hu et al. [34] does not allow to conclude if protons (H^+) or protiums (H atoms) enter the layered material: For protons, immediate neutralization is expected, as the proton's electron affinity of 13.6 eV is significantly higher than the work function of the host materials, even for a wide band gap insulator as *h*-BN. On the other hand, any two H atoms encountering each other are expected to recombine immediately due to the high binding energy when forming H_2 (4.52 eV in the gas phase) [35]. The observed transport process of hydrogen through *h*-BN and MoS_2 requires, therefore, further investigations.

The aim of this chapter is to answer two open questions regarding the experiment of Hu et al. [34], namely i) which hydrogen species are transported within the layered materials (protons or protiums) and ii) what is the diffusion mechanism of these species in the interstitial space between the layers.

In order to answer these questions, we investigate, on the grounds of first-principles calculations, the chemical interaction and self-diffusion coefficients of both H and H^+ species in *h*-BN, MoS_2, and graphite. We show that both H^+ and H can be accommodated in *h*-BN and MoS_2, and that diffusion mechanism follows low free-energy barrier zigzag hopping between adjacent layers. This zigzag hopping is assisted by the low-frequency rigid-layer shear modes (52.5 cm^{-1} and 33.7 cm^{-1} for *h*-BN [132,

161] and MoS_2 [162]). Moreover, sulfur vacancies—a typical defect in MoS_2 [163]—act as hydrogen traps and suppress the transport. The calculated self-diffusion coefficients suggest that both H in MoS_2 and *h*-BN are transported easily, with significantly lower diffusion barrier compared to the entry barrier to the interstitial space. The same is true for protons in MoS_2, while proton self-diffusion in *h*-BN is hampered. In graphite, protons are immediately neutralized to H atoms, which themselves are almost immobile once bound to the carbon atoms [164-166].

4.2 Methodology

We calculate the free energy surfaces (FESs) of hydrogen particle (charged proton H^+ and neutral protium atom H) transport in the interstitial space of layered *h*-BN, MoS_2, and graphite, which can give us a straightforward insight of the free energy barrier in each scenario. The FESs are obtained by employing well-tempered-metadynamics (WT-MetaD) simulations, see Section 2.4.3 for further theoretical backgrounds of WT-MetaD.

The self-diffusion coefficient D_d of hydrogen particle transfer in the interstitial space of layered materials is calculated from the following formula [167]:

$$D_d = D_0 \exp(-\frac{E_a}{k_B T}) \tag{4.2.1}$$

where D_0 is the pre-factor, T is temperature (here set to 300 K, which is the experimental condition), k_B is Boltzmann's constant, and E_a is the free energy barrier for hopping process of hydrogen species, which is obtained from WTMetaD simulations. D_0 is calculated as follows [168]:

$$D_0 = \frac{(\Delta r)^2 \upsilon_0}{q_i} \tag{4.2.2}$$

where Δr is the distance between H species in two adjacent binding sites, υ_0 is the frequency of the bond stretching modes (here is N-H or B-H stretching), and q_i is 2, 4,

or 6, for the diffusion dimensionality of 1D, 2D, or 3D, respectively. In this work, we consider a 2D diffusion, therefore q_i is taken as 4.

4.3 Calculation Details

We have studied three layered materials, namely *h*-BN, MoS_2, and graphite (see Figure 4.3.1). For all the systems, the interaction of proton (H^+) and protium (H atom) with the layers was investigated. We used the following supercells to describe the interactions: the 4×4×2 supercell was used for both *h*-BN and graphite, while 4×4×1 supercell for MoS_2, resulting in 128 atoms in *h*-BN and graphite, and 96 atoms in MoS_2. Both supercell representations result in the *c* lattice vector of about 12-14 Å, thus a similar simulation box in all models. The fully optimized lattice parameters of each system are shown in Table 4.4.1 and are in a fairly good agreement with the experimental values [150, 169, 170].

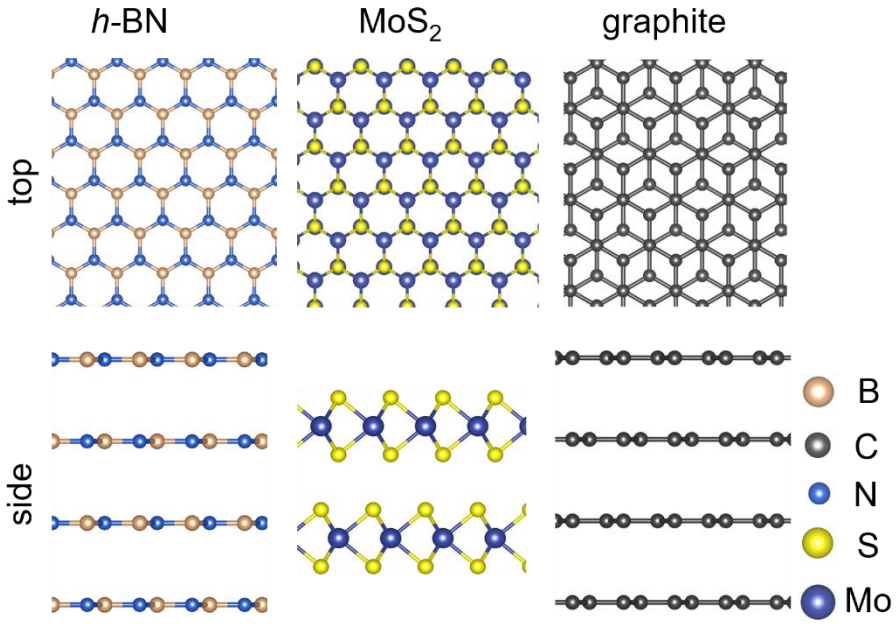

Figure 4.3.1 Top and side views of layered materials considered in this chapter.

All the calculations were performed using density functional theory (DFT) with Perdew-Burke-Ernzerhof [64] (PBE) functional and D3 correction of van der Waals

interactions following the approach of Grimme [76] as implemented in the *CP2K 3.0* package [171]. The Quickstep method was employed, with Goedecker-Teter-Hutter [172] (GTH) pseudopotentials together with DZVP-MOLOPT-GTH-SR basis set for B, C, N, S, and Mo. Hydrogen was treated with the DZVP-all electron basis set and all-electron potential. Plane-wave energy cutoff was set to 360 Ry and the atomic positions and lattice parameters were fully optimized. The charged periodic systems were calculated using background charge as implemented in *CP2K 3.0* package [171] and the charge was set to the total system.

Well-tempered metadynamics [99] (WTMetaD) simulations were performed to obtain the free energy barriers. The canonical *NVT* ensemble [173] (constant number of atoms (*N*), constant volume (*V*) and constant temperature *(T)*) was employed. Temperature was set to 300 K using *CSVR* (canonical sampling velocity rescaling) thermostat [174], with the temperature parameter ΔT of 1500 K and a time step of 0.5 fs. Every 200 steps, a Gaussian hill was spawned, the adopted Gaussian hills height and width were set to $1x10^{-3}$ hartree and 0.1 (internal cp2k units), respectively. Each WTMetaD simulation was preceded by standard Born-Oppenheimer molecular dynamics (BOMD) simulations (MD; *NVT*, 300 K, time step of 0.5 fs) with duration of 7 ps. Two collective variables (CVs) were defined to trigger the process of H^+ or H transfer (see Figure 4.3.2). For instance, in the case of H^+ inside *h*-BN, the nitrogen atoms in *h*-BN are divided into three different kinds: NI (inner layer with H^+ bound), NII (inner layer neighboring NI), and N (outermost layers). The first collective variable CV1, is defined as the coordination number of H^+ to NI, while the other collective variable, CV2, is defined as the coordination number of H^+ to NII. Similar CVs were divided for MoS_2 and graphite, see Figure 4.3.2b-d.

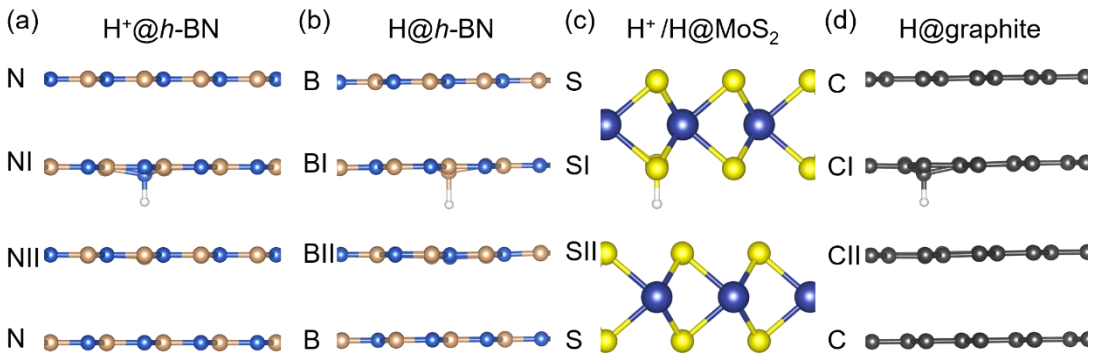

Figure 4.3.2 The definition of the collective variable in the WTMetaD simulations: (a) H^+ in *h*-BN, (b) H in *h*-BN, (c) H^+ and H in MoS_2, (d) H in graphite.

The form of the coordination function is defined as follows:

$$CN_{\mathrm{H-X}} = \sum_i^H \sum_j^X \frac{1-(\frac{r_{ij}}{R_0})^6}{1-(\frac{r_{ij}}{R_0})^{12}} \tag{4.3.1}$$

For the CVs defined in each system, the following reference *H-X* (X = N or B) distances (R_0) were used: 2.3 a_0 for H^+@*h*BN, 2.9 a_0 for H@*h*BN, 2.5 a_0 for H@graphite, 3.0 a_0 for H@MoS_2 and H^+@ MoS_2. These parameters are slightly larger (up to 10%) than the average value in the fluctuation of the corresponding H-X distances during the BOMD simulations. Thus, when the H or H^+ is close to the transition state region, the coordination number of H to X is close to 0. We have also investigated the scenario with three CVs specified, where the third CV describes the hopping of H species within the same layer. However, such a process was not observed with the employed number of hills, which indicates in all cases, the free energy barrier for transport within the same layer was much higher than between the layers. Thus, it is a safe and efficient choice to use the two CVs during the simulations.

4.4 Results

We first discuss the experimental setup of Hu et al. [34], which is schematically shown in Figure 4.4.1. We separate the path of hydrogen species between the two hydrogen injecting palladium electrodes, PdHx, in three steps: the entrance of hydrogen species

from the electrode to the layered material (step I), which is governed by the entry energy barrier; the diffusion of hydrogen species in the interstitial space of the layered material (step II); and the exit of hydrogen species from the layered material back to the electrode (step III), where the energy barrier is equal to the negative of the entry barrier. While steps I and III have been determined from experimental data in Ref. [34] (an entry barrier of 0.45±0.04 eV was reported for *h*-BN), the type of the hydrogen species (protons or protiums) transported between the layers, the diffusion mechanism of the species inside the interstitial of the layered material, and the energy barrier related to this diffusion are still unknown and will be discussed below.

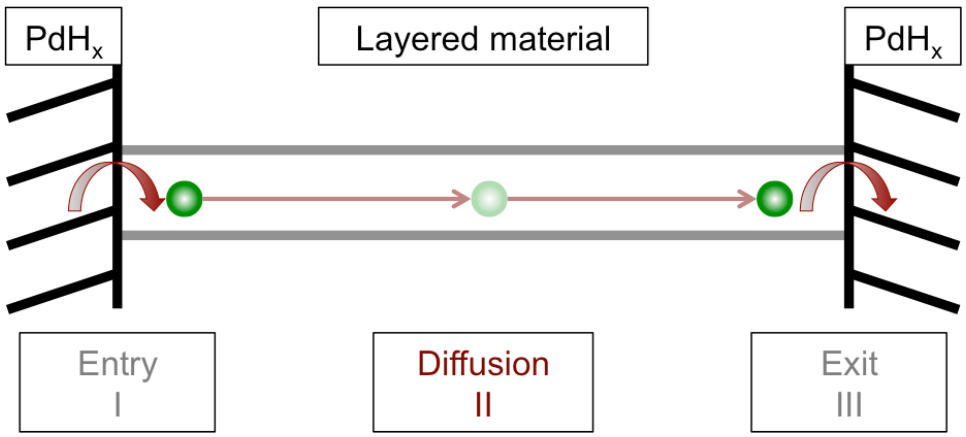

Figure 4.4.1 Schematic representation of experimental setup [34]. Three main steps are identified: Step I—diffusion of hydrogen species from PdHx electrode into the layered material. Step II—diffusion of hydrogen species between the layers of the layered material. Step III—diffusion of hydrogen from the layered material back to the electrode. Each step is governed by energy barriers: entry barrier for step I, self-diffusion barrier for step II, and exit barrier (equal to negative of entry barrier) in step III. Adapted from Ref. [155].

The energy involved in the process of H or H^+ entering from PdHx electrode is difficult to estimate, as the atomistic details are not known. There is obviously a much stronger binding of H^+ to the layered material compared to H atom, however, a similar Coulomb energy penalty applies, when H^+ is removed from its PdHx source. A very rough estimation of the thermodynamic cycle suggests that both processes would show a similar energetic profile (see "A1 Thermodynamic cycle-estimation of transfer energies" in Appendix). At present, the experimentally assessed entrance barrier of about 0.45 eV

in step I is the best estimate for this process.

4.4.1 Structural properties of proton and protium in *h*-BN, MoS_2, and graphite

We first study single proton (H^+) or protium (H atom) confined in the interstitial space of layered bulk crystals of *h*-BN, MoS_2, and graphite. A proton located in the interstitial space of *h*-BN binds to a N atom, forming a N-H bond with a bond length of 1.05 Å (which is only slightly longer than the N-H bond length in NH_3 (1.02 Å) and $NH4^+$ (1.03 Å)), and locally slightly decreases the interlayer separation. On the contrary, a H atom forms a B-H bond of 1.32 Å length (compared with 1.35 Å in boron hydrides [175], e.g., B_5H_9) and slightly increases the interlayer separation. Details are given in Figure 4.4.2 and Table 4.4.1. Due to the fourth bond, which forms upon binding H^+ or H, both N and B atoms transform from sp^2 to sp^3 hybridization and thus pyramidalize to approach a tetrahedral configuration. Therefore, independent of H atom or H^+ in the lattice, the local bonding to B or N, respectively, gives similar structural parameters compared to the corresponding bonds in the corresponding neutral gas phase molecules. In MoS_2, H^+ (or H atom) connects to a S atom, forming a S-H bond of 1.37 (1.43) Å, and also slightly decreases (increases) the local interlayer distance. For metallic graphite, proton immediately neutralizes once it enters into the interlayer space, and binds to a C atom, forming a C-H bond of 1.12 Å (compared with 1.10 Å in CH_4), and the interlayer distance increases due to the pyramidalization of the binding carbon atom, similar to the case of *h*-BN.

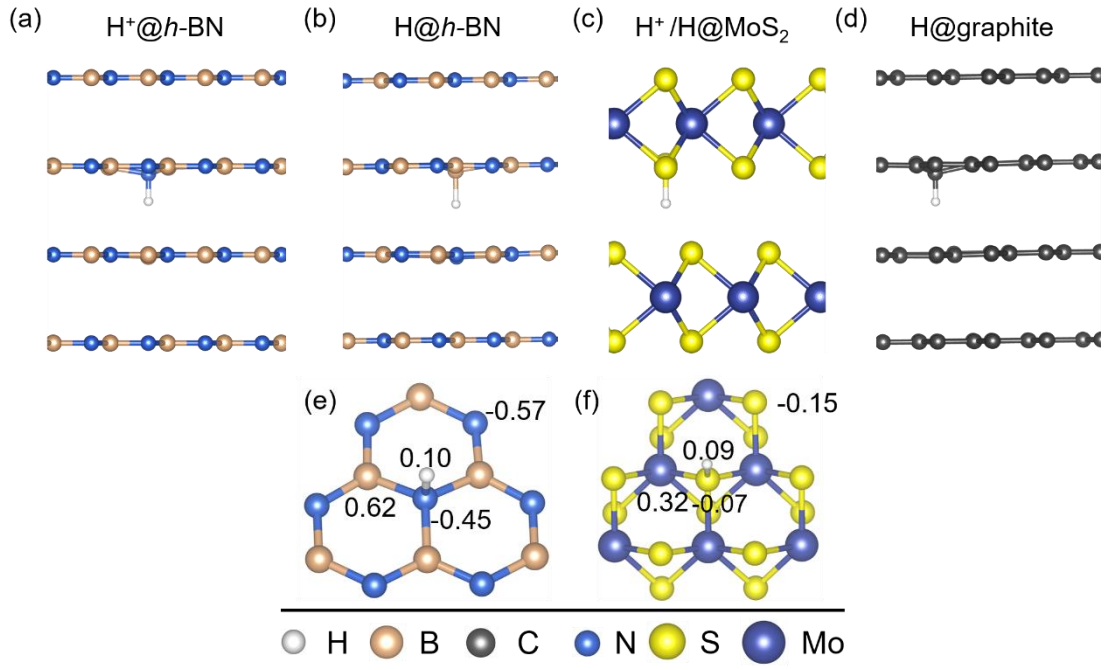

Figure 4.4.2 (a-d) Side view of H and H^+ bound to layered materials. In *h*-BN, H binds to B and H^+ binds to N; in MoS_2 both species bind to S; in graphite, H^+ gets neutralized, H binds to C. Binding atoms in *h*-BN and graphite are pyramidalized. Here, similar to the nomenclature in endohedral fullerenes, @ indicates the H^+ or H bound to the crystal. (e-f) Hirshfeld atomic charges of proton, the binding atoms, and their closest neighbors (cf. atomic charges in perfect materials: N (-0.58 e^-), B (0.58 e^-), S (-0.16 e^-), Mo (0.31 e^-)). The proton gets nearly neutralized upon binding and the charge of H^+ is delocalized in an area of about 3 Å around it.

Table 4.4.1 Calculated lattice parameters (*a*, *b*, and *c*) and the interlayer distances (d) in perfect *h*-BN, MoS_2 and graphite, shown with and without H species bound to the layers. Available experimental data are given in parenthesis [150, 169, 170]. Bond distances between H^+ or H atom and the binding atoms are also given.

System	***a* = *b* [Å]**	***c* [Å]**	***d* [Å]**	**X—H [Å]**
h-BN	2.512 (2.504)	6.784 (6.661)	3.393 (3.330)	-
H^+@*h*-BN	2.510	6.539	3.286	1.052 (N-H)
H@*h*-BN	2.513	6.845	3.427	1.322 (B-H)
MoS_2	3.164 (3.150)	12.320 (12.300)	6.160 (6.150)	-
H^+@MoS_2	3.150	12.124	6.062	1.370 (S-H)
H@MoS_2	3.160	12.365	6.178	1.426 (S-H)

Graphite	2.466 (2.460)	6.828 (6.710)	3.414 (3.355)	-
H@Graphite	2.467	6.874	3.429	1.124 (C-H)

We analyzed the electronic structures of covalently bound H^+ or H atom employing the Hirshfeld atomic charge analysis. Due to the high ionization potential of hydrogen, H^+ picks up almost one electron (~0.90 e^- both in *h*-BN and MoS_2) once bound to the crystal lattice. This charge is transferred mainly from the atoms that are in its closest vicinity (see Figure 4.4.2). Thus, even though the charge persists in its vicinity, the proton itself is almost neutralized. The N or S atoms, to which the proton binds, become less negatively charged (-0.45 e^- and -0.07 e^- vs. -0.58 e^- and -0.15(5) e^- in the perfect *h*-BN and MoS_2, respectively). Also, the second neighbors become slightly more positively charged, but the effect is much weaker than for the binding atom (0.62 e^- (B) and 0.32 e^- (Mo) vs. 0.58 e^- and 0.31 e^- in the perfect *h*-BN and MoS_2, respectively). The proton charge is delocalized in an area of about 3 Å radius. This effect is also shown by the electron density isosurfaces (see Figure 4.4.3). Even though the protons get immediately neutralized by the surrounding atoms of the crystal, in the remainder, we will still use the term proton in order to acknowledge the local charge of the system. On the other hand, no charge transfer between the *h*-BN, MoS_2 or graphite layers and the bound H atom is observed.

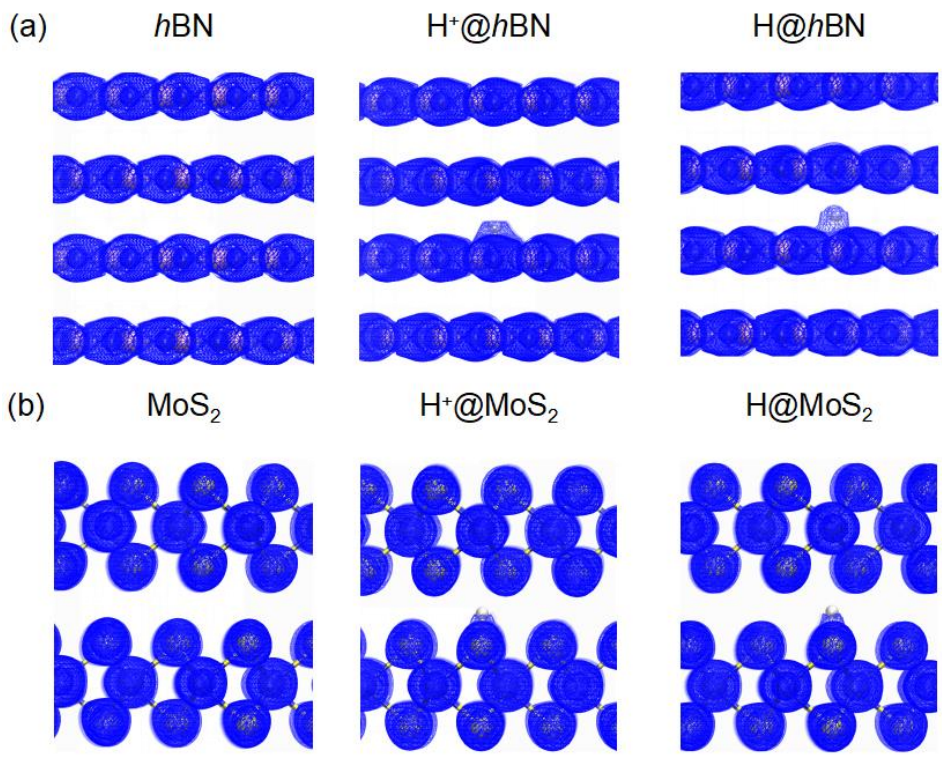

Figure 4.4.3 Electron density isosurfaces of *h*-BN (a) and MoS_2 (b) bulk systems with and without H^+ and H bound to the layers. In case of H^+, there is electron density on H upon binding, indicating charge transfer and neutralization of proton.

4.4.2. Diffusion process of proton and protium inside *h*-BN, MoS_2, and graphite

Next, we have simulated the diffusion process of the protons and H atoms through the interstitial space between the layers of 2D materials. Here, we exclude diffusion through the layers, as reported barriers for *h*-BN (0.9 eV) [38], which is significantly higher than transport within the interstitial space; and for MoS_2, no H species can permeate through due to its thick electron clouds [40], therefore, diffusion through the layers is not relevant for the time scales discussed here. As both H and H^+ bind to atoms of the crystal lattice, we investigated the transport process between individual binding sites. As the system has many degrees of freedom, including low-energy vibrational modes with rather large amplitudes, we employed well-tempered metadynamics [99] (WTMetaD) to determine the free-energy surface (FES) and to analyze the diffusion

barriers of H and H^+ travelling through the interstitial space of the layered materials (for details on WTMetD and DFT calculations see Section 4.2 and Section 4.3). The FES and the diffusion barriers for H^+ and H atom are discussed below in detail. Note that diffusion is governed by Brownian motion, thus, the directionality of the diffusion is not defined via the collective variables. However, below, we will refer to this as "path". The information that is the most important from these simulations is the lowest free-energy barrier for the transfer of hydrogen species in between the layers, which allows the calculation of the self-diffusion coefficient.

We first concentrate on *h*-BN: the low-energy paths for H and H^+ diffusing through *h*-BN are shown in Figure 4.4.4a-c and Figure 4.4.4d-f, respectively. The estimated free-energy barriers are 0.46 eV for H^+ and 0.08 eV for H atom (Figure 4.4.4b and e). In our simulations, H^+ (H atom) is initially bound to the nitrogen atom N1 (boron atom B1) in one layer (black; Figure 4.4.4a and d), which are the preferential binding sites. Most layered materials, including *h*-BN, exhibit low-energy shearing modes [132, 161]. Once the shearing brings a N atom of the adjacent layer to the vicinity of the proton, the probability that proton jumps to the closest N atom in this layer (N2, red) becomes significant. After the first proton jump, the next jump (N2 to N3, green) then goes back to the first layer, and so forth, resulting in a zigzag transport path between layers. Thus, after each two successive jumps, H^+ can be displaced by about 2.5 Å (the shortest intralayer N-N distance). It is important to note that proton carries its charge during the diffusion and hopping process: even though the proton is nearly neutralized, while being bound to N atom, when transferring to the next N adsorption site, it leaves the electron behind. The atomic charge analysis shows that the electronic configuration of the layer recovers to the pristine state after the proton has left, but the new binding site has a similar electronic configuration as the previous one.

The diffusion process of H atom follows a similar shear-assisted process, with the difference that the binding sites are now the B atoms and that the FES is shallower due to the lower binding strength of H atom to the lattice, when compared to protons. It

should be noted that the free-energy barriers cannot be corrected for the zero-point energy without explicit nuclear quantum effect consideration, for example in a path integral approach. Therefore, the nuclear quantum effects are not included in the calculations presented in this chapter.

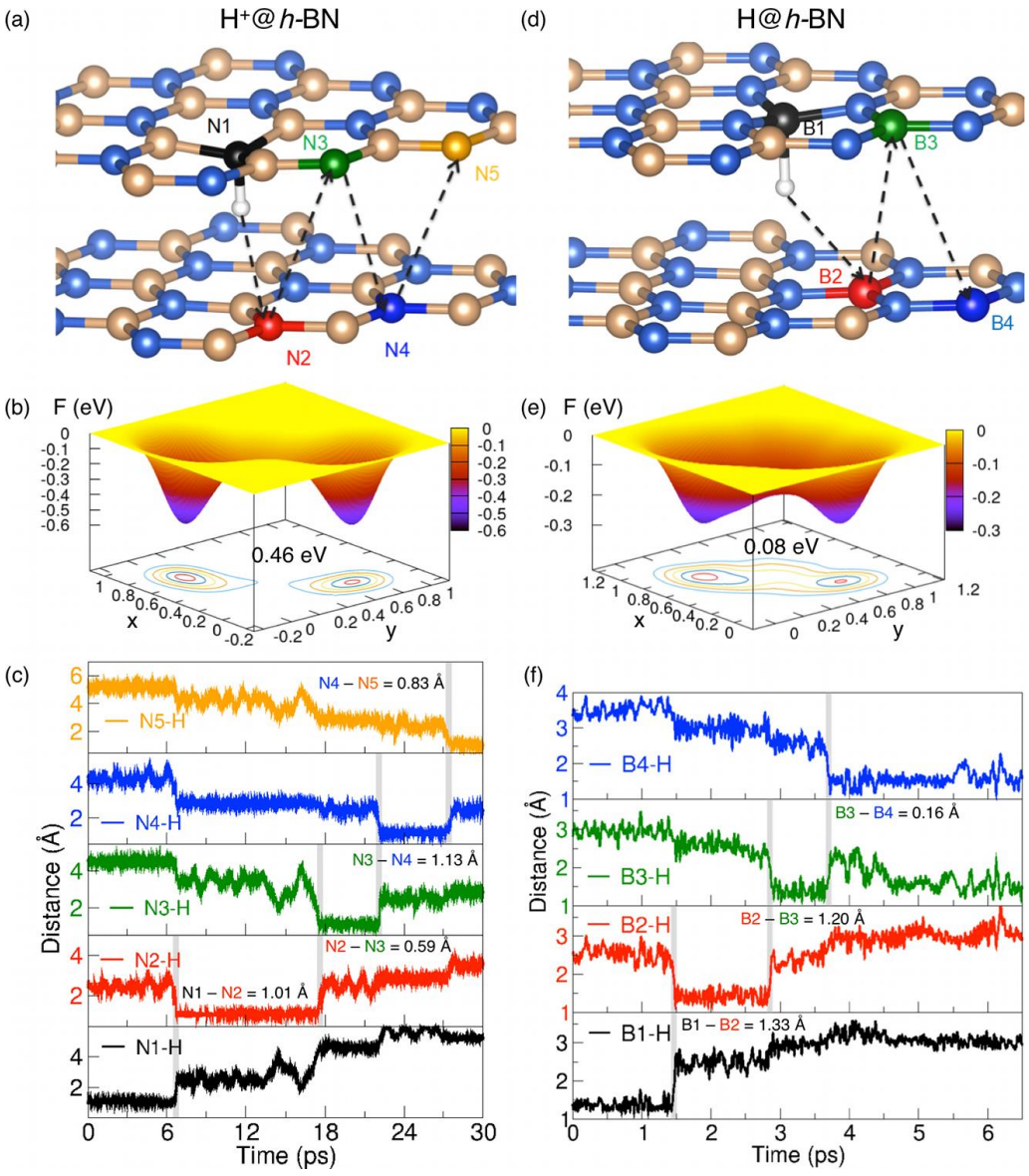

Figure 4.4.4 WTMetaD simulations of H^+ (a-c) and H (d-f) diffusion in between layers of *h*-BN. Both species are transported in a zigzag manner between the layers with low free-energy barriers. (a, d) Transfer paths along the *h*-BN interstitial space (zoom-in picture on two layers of interest), (b, e) Free-energy surface of the H species transfer between layers. The x and y axis correspond to the collective variables (CV1 and CV2), as defined in Figure 4.3.2 in Section 4.3, and the z axis and color legend refer to the free energy, F (in eV). (c, f) Change in the bond distances N-H and B-H during the WTMetaD trajectory as function of time. The vertical grey lines indicate the H or H^+

jump between the binding sites in neighboring layers as indicated in color in (a) and (d). The N-N and B-B distances indicate the in-plane distance between the neighboring transfer sites (compared with the same distances in the perfect stacking faults: AA' 1.45 Å, A'B and AB' 0.00 Å) indicate shearing from AA' towards either A'B or AB' stacking.

Close inspection of the WTMetD pathway suggests that the shear mode, where the individual layers slide against each other, significantly shortens the distance between the two next low-energy hopping sites (the next N or B atom in the neighboring layer, as depicted in Figure 4.4.4c and f). Thus, it has a strong effect on the hopping barrier. These shear modes are well-known for *h*-BN and MoS_2. They have been confirmed by Raman data (52.5 cm^{-1} and 33.7 cm^{-1} for *h*-BN [132, 161] and MoS_2 [162]) and the reported barriers for interlayer shear are as low as 8 meV and 2 meV, for the shearing between the most stable AA' stacking (N over B) to the A'B (N over N) and to AB' (B over B), respectively [130, 131]. These energy barriers are much smaller than k_BT at 300 K (about 25 meV), thus well accessible at room temperature. Indeed, analysis of the trajectory demonstrates that most transfers of H or H^+ between the layers have been assisted by the shear mode (see caption of Figure 4.4.4). Moreover, lowering the transition barrier by ~0.5 eV is confirmed by static calculations, shown in Figure 4.4.5.

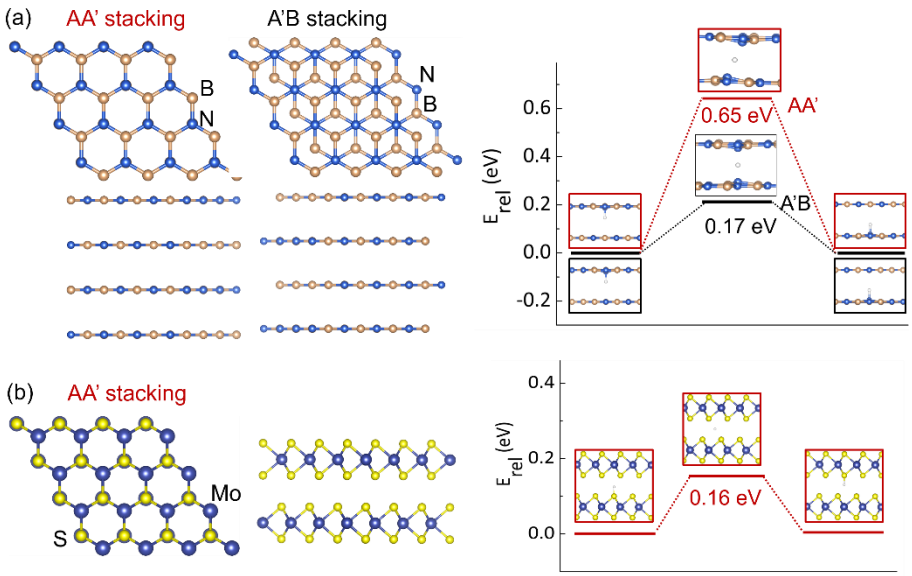

Figure 4.4.5 Static calculations of the potential energy barriers of H^+ transfer between layers of *h*-BN in the AA' and A'B stacking faults (a) and in AA' stacking of MoS_2 (b).

From the free-energy barriers, we estimated the self-diffusion coefficients of both species between the layers (see Section 4.2 for details). The calculated diffusion coefficients of H^+ and H inside *h*-BN in step II (cf. Figure 4.4.1) are $7.22 \times 10^{-11}\ cm^2 s^{-1}$ and $2.72 \times 10^{-4}\ cm^2 s^{-1}$, respectively, suggesting that the species transported in the experimental set up are H atoms. The much smaller self-diffusion coefficient value for H^+ comes from stronger binding of proton to a nitrogen atom than for hydrogen atom binging to a boron atom. For comparison, the reported experimental diffusion coefficient from the electrode to the layered material (in step I) was estimated to be $10^{-4} - 10^{-3}\ cm^2 s^{-1}$ [34].

We now turn to the case of MoS_2 layered crystals, for which we performed the same type of WTMetaD simulations of H^+ and H inside the interstitials. Both protium and proton inside MoS_2 bind to S atoms with very similar binding strengths. The transport mechanism is very similar to that in *h*-BN: initially, H^+ or H bind to sulfur atom S1 (see Figure 4.4.6a; black). As in *h*-BN, the diffusion is assisted by the shear modes, which allow the transfer from S1 to S2 or S3 in the adjacent layer. The next transfer can then either go back to the starting point, or hop to the next site, and so on. The trajectories are very similar in both cases; therefore, in Figure 4.4.6a, we only show the example of H atom. Both H and H^+ in MoS_2 are also transported along a zigzag path, hopping between the neighboring layers and the transfer is supported by low-energy shear modes. The changes in the S-H distances between binding sites are shown in Figure 4.4.6b for H atom case. The corresponding FES plots are given in Figure 4.4.6c and d. The FES profiles show the free-energy barriers of 0.11 eV for H^+ and 0.09 eV for H atom. Unlike in the case of *h*-BN, the barriers in MoS_2 are very similar, because of the same type of bonding atoms. These energy barriers are smaller than in the case of *h*-BN for the proton, while slightly higher for H atom inside *h*-BN. The calculated diffusion coefficients of H^+ and H inside MoS_2 are $6.91 \times 10^{-5}\ cm^2 s^{-1}$ and $1.50 \times 10^{-4}\ cm^2 s^{-1}$, again suggesting that the species transported in the experimental set up are H atoms, however, in this case the protons could also be possible.

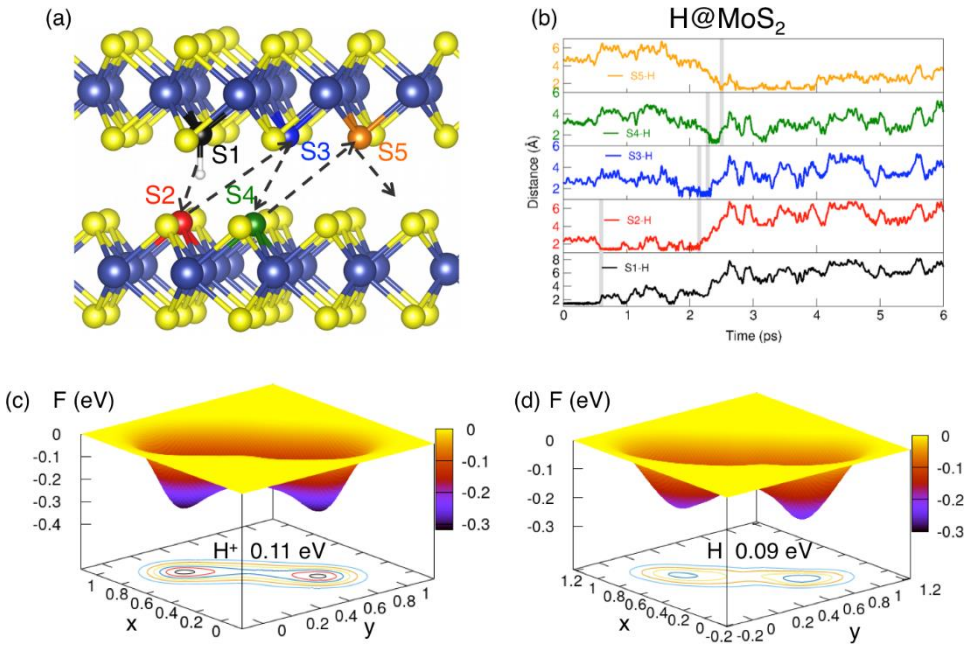

Figure 4.4.6 (a) Schematic of the H atom transfers path in perfect MoS_2 and (b) the change in the bond distances S-H during the WTMetaD trajectory as function of time (similar behavior also for H^+). The vertical grey lines indicate the H atom jumps between the binding sites in neighboring layers as indicated in color in (a). (c) and (d) are free-energy surfaces of H^+ and H atom transfer along the MoS_2 interstitial, respectively.

In contrast to *h*-BN or graphite, defects are much more common in the natural or synthesized MoS_2, typically with a dominant occurrence of sulfur vacancies [163]. Therefore, we studied also the diffusion of H species in the presence of this defect type. The WTMetaD results are shown in Figure 4.4.7, revealing that both H and H^+ are attracted strongly by the S atoms surrounding the vacancy site. The vacancy traps the travelling species and this effect appears to be stronger for H atoms than for protons. The FES for protons is 0.10 eV, close to the barriers in a perfect material. For H atom, we have obtained two different barriers, 0.06 eV and 0.25 eV, which might be due to the charge redistribution close to the vacancy and different binding strengths to the S atoms in the vicinity of the vacancy and far from it (see Figure 4.4.8). We found that the S-H binding strength is different when H species are close or far from the vacancy (see Figure 4.4.8). The total energy difference between H^+ bound close to the vacancy or far from it is only 2.4 kJ/mol, while for H atom, this total energy difference is as large as 12.1 kJ/mol, leading to the asymmetric FES. The binding energies of H atoms

to S atoms in perfect and defective MoS_2 are -0.65 eV and -1.33 eV, respectively, indicating stronger interaction H species with the surrounding of the vacancy. The smaller barrier corresponds to the hopping between binding sites far from the vacancy, which is similar to the case of a perfect system. The higher barrier corresponds to the hopping between binding sites close to the vacancy, showing that these sites interact much stronger with H atoms. The corresponding calculated diffusion coefficients inside defective MoS_2 are $1.02 \times 10^{-4}\ cm^2 s^{-1}$ (for H^+) and $4.78 \times 10^{-4}\ cm^2 s^{-1}$ and $3.07 \times 10^{-7}\ cm^2 s^{-1}$ (for H atom). The vacancies, therefore, suppress the overall transport properties of MoS_2, which could explain why in the experiment, the *h*-BN is a better hydrogen conducting material than MoS_2 [34].

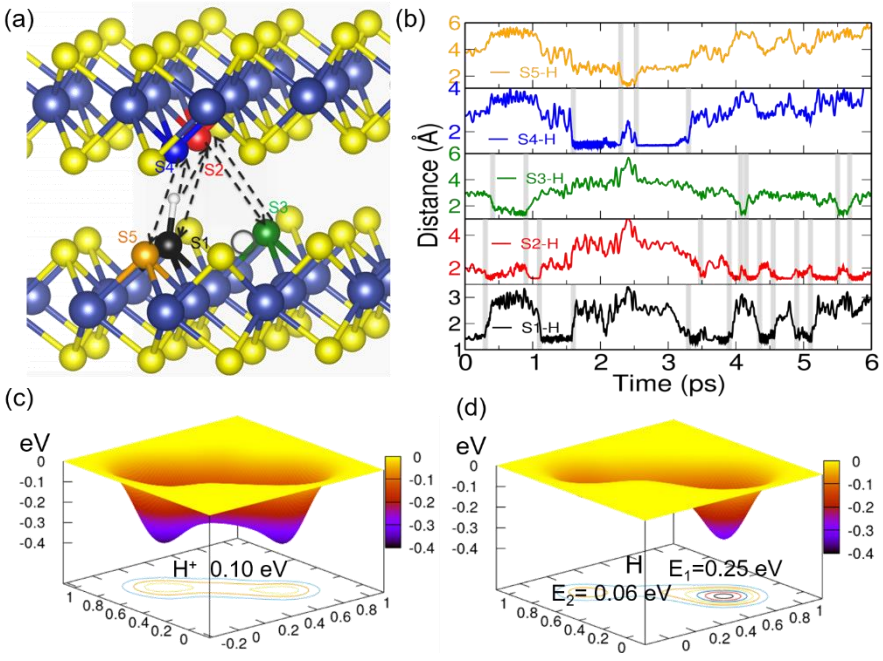

Figure 4.4.7 Schematic of the H^+ or H transfers path in defective MoS_2. (b) S-H bond distances change during WTMetaD simulations. For (a) and (b), we have similar behavior with H^+ and H, therefore, only exemplary plots for H atoms are shown. (c) Free energy surface of H^+ transfer along the defective MoS_2. (d) Free energy surface of H atom transfer along the defective MoS_2.

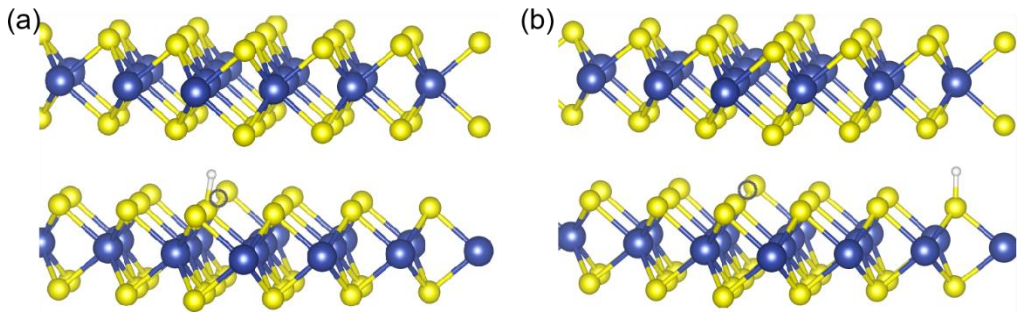

Figure 4.4.8 (a) H^+ or H atom bound far away from the sulfur vacancy. (b) H^+ or H atom bound close to the sulfur vacancy. The sulfur vacancy is marked as an empty gray circle.

Finally, we have investigated H atom inside graphite (proton gets immediately neutralized inside this system), as shown in Figure 4.4.9. Here, however, we have not observed any H atom transfers with free-energy barriers similar to the other materials, meaning that this process would require much higher activation energies and would be improbable in the experimental conditions. This is because the C-H bond is very strong, therefore, in order to allow the H transfer to the other layer, large energy is required to break the C-H bond. The simulation reveals only a single minimum in FES (corresponding to the stretching of C-H bond). If more hills were used, higher free-energy barrier would be overcome, however, this barrier would be too large to observe such a transfer experimentally (much larger than 0.7 eV). This finding is consistent with the experimental results [164-166], which show that graphite does not conduct hydrogen.

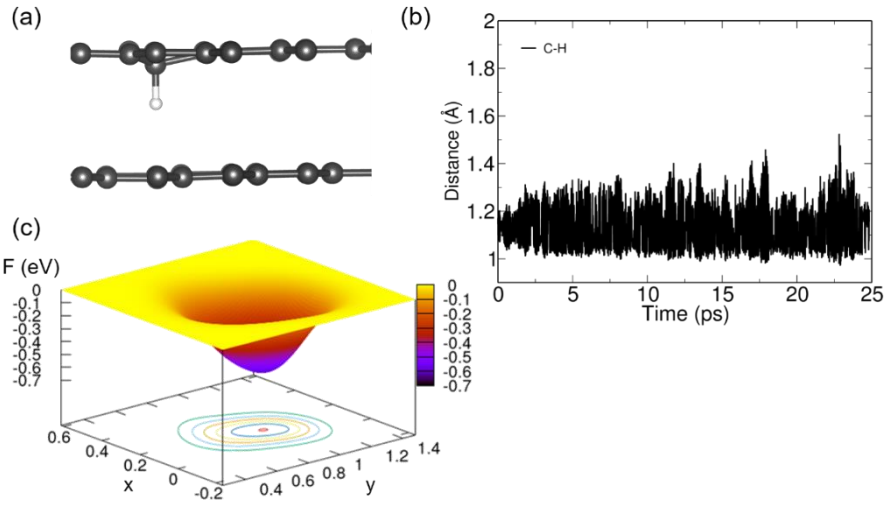

Figure 4.4.9 (a) H atom bound to graphite layers. (b) C-H bond distances change during WTMetaD simulations. (c) Free energy surface of H atom inside graphite.

4.4.3 Can H atoms Recombine to H_2 Molecules in the Interstitial Space of Layered Materials?

The large difference in the self-diffusion coefficients suggests that single hydrogen atoms are transported through the interstitial space of *h*-BN in experiment. This poses, however, the question of why hydrogen atoms do not recombine and form H_2 in the interstitial space. Indeed, the binding energy (while forming H_2) in the interstitial space is, though 1 eV smaller than for the free species, strongly exothermic (3.46 eV). We calculated all possible scenarios of two protiums interacting within the interstitial space of *h*-BN layers: two H atoms bind to the same layer, adjacent layer, and the same layer but different interstitials, as shown in Figure 4.4.10.

Single H atom carries a single spin, therefore, the following combinations of two H atoms can be considered: singlet, triplet, or, for large distances, antiferromagnetic singlet. At a close distance, only two configurations are possible, which reflect the H_2 molecule in the bonding singlet or in the antibonding triplet state (see Figure 4.4.10). For large distances, protiums do not interact with each other. Indeed, in the experiment of Hu et al. [34], the hydrogen species concentration (c_H) at the entrance to the *h*-BN

was very low, only 10^{13}-10^{14} cm^{-3}, that is, one proton or protium per 10^8 BN units. If they approach each other, they would not interact in case of parallel spins (Figure 4.4.10, red curves, modeled as the triplet state), but spin relaxation will favor the much more stable singlet state. Independent if the protiums are bound to the same (Figure 4.4.10a) or neighboring (Figure 4.4.10b) layers, for distances above 3 Å, a proton-hydride pair with the hydride bound to a boron and proton bound to the nitrogen is the most stable configuration (black curves), and additional Coulomb attraction will readily form the most stable structure, namely H_2 molecule in the interstitial region of the *h*-BN lattice (blue triangles). Also, if the H atoms are bound to the same layer, but at opposite interstitial sites, the formation of local proton-hydride pairs is energetically favored (Figure 4.4.10c).

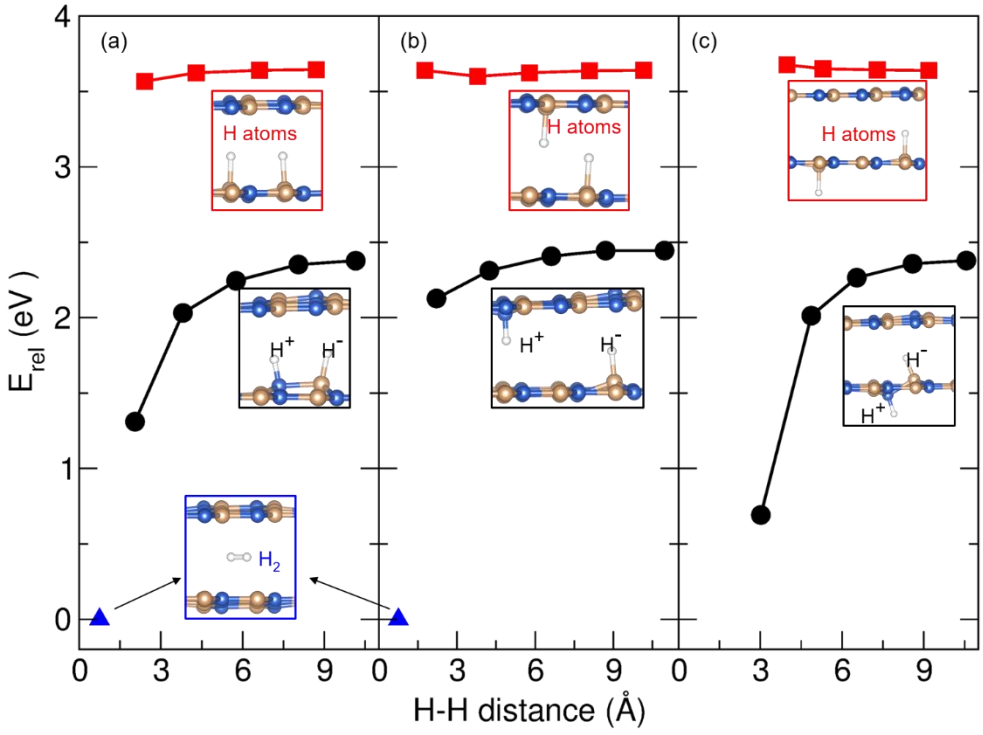

Figure 4.4.10 Relative energy (E_{rel}) of 2 H atoms in *h*-BN with respect to H_2 molecule in the interstitial space of *h*-BN lattice as function of distance between the 2 H atoms. Two H atoms bind to the same layer (a), adjacent layer (b) or the same layer but different interstitials (c). The blue triangles indicate H_2 molecule in the interstitial space, black circles proton-hydride (H^+—H^-) pairs, attached to N and B atom. The red squares show two non-interacting protiums (modeled as triplet state). For spin flip energies

between the triplet and antiferromagnetic single see Table A1 in Section A3 “Spin flip energies” in Appendix.

The blue triangles in Figure 4.4.10 indicate H_2 molecule in the interstitial space, black circles proton-hydride ($H^+ — H^-$) pairs, attached to N and B atom. An interatomic distance between two protiums of 3 Å or less always results in recombination to H_2. This apparent contradiction can be explained by the very low concentration of hydrogen species reported in the experiment [34], where a concentration of 10^{13}-10^{14} cm^{-3} was reported. This number corresponds to one H atom per about 2 m^2. Thus, the interplay of low hydrogen concentration, the quasi two-dimensional diffusion path in the interstitial space between the *h*-BN layers, and the high self-diffusion coefficient allows the transport of atomic hydrogen between the PdHx electrodes.

4.5 Conclusions

In conclusion, free energy barriers and related self-diffusion coefficients calculated using first-principles BO well-tempered metadynamics simulations demonstrate high mobility of protium in *h*-BN and MoS_2. In contrast, H^+ is highly mobile in MoS_2, but has a low self-diffusion coefficient in H^+ in *h*-BN. Hydrogen attached to graphite is essentially immobile. The related overall lattice of the layered materials remains intact. Locally, protons bind to N (S for MoS_2), pick an electron from the lattices and leave a charged site that extends over a few atoms. At low concentration, this charged state would be maintained. Protium binds to B (S for MoS_2) atoms. The transport of both protium and protons follows a zigzag path where the transported species hop between two adjacent layers. The probability of such a hopping is strongly increased by the interlayer shear modes that are typical for these materials. Recombination of protium will always occur if the species get close to each other, and is avoided only by low concentration and the quasi two-dimensional transport process. Our results should be of interest for hydrogen transport in other layered van der Waals materials, which could be important for applications in hydrogen isotope separation.

Part II

Quantum Sieving Isotopes via Two-dimensional Materials

5. Hydron Isotope Separation Through Graphene and *h*-BN Monolayers

While the isotope-dependent hydrogen permeability of graphene membranes at ambient condition has been demonstrated, the underlying mechanism has been controversially discussed during the past five years. The reported room temperature H^+-over-D^+ selectivity is 10, much higher than in any competing method. Yet, it has not been understood how protons can penetrate through graphene membranes — proposed hypotheses include atomic defects and local hydrogenation. However, neither could explain both the high permeability and high selectivity of the atomically thin membranes. In this chapter, we investigate the influence of quantum tunneling in the process of hydron isotope permeation and separation through 2D materials. We confirm that ideal graphene is quasi-impermeable to protons, yet the most common defect in sp^2 carbons, the topological Stone-Wales defect, has a calculated penetration barrier below 1 eV and H^+-over-D^+ selectivity of 7 at room temperature and, thus, explains all experimental results on graphene membrane that are available to date. We challenge the competing explanation, local hydrogenation, which also reduces the penetration barrier, but shows significantly lower isotope selectivity.

The results shown in this chapter are published in the journal of *Advanced Mater*ials, 2020, 32 (37), 2002442. The calculations were performed by myself, the quantum tunneling was calculated with a code written by A. F. Oliveira. The manuscript was prepared by myself with comments and remarks from A. Kuc, T. Brumme, A. F. Oliveira and T. Heine. Readers will find most of the following chapter in the original paper [176]. Reproduced with the permission from Advance Materials, 2020. *32*, 2002442. Copyright Wiley-VCH, Weinheim.

5.1 Introduction

Hydrogen isotopes (protium H, deuterium D, and tritium T) are important in various fields of science and technology [12-14, 177]; however, one of the most important issues to solve is their separation. For deuterium separation, currently available approaches on the industrial plant scale, such as H_2 distillation and water–hydrogen sulfide exchange [15], are exceedingly energy- and time-intensive, with very low separation factors, usually less than 2.5; and methods to capture tritium from low-concentration solutions are still unknown. This stimulates the exploration of possible alternative hydrogen isotope separation methods.

Recent experiments [41, 42], demonstrated that single atom-thin membranes of mechanically exfoliated graphene and *h*-BN are permeable to thermal protons (H^+), but much less so to deuterons (D^+), resulting in a room temperature selectivity for H^+/D^+ about 10, much higher than in the conventional separation methods [15]. These interesting findings are discussed somewhat controversially, both on theoretical [39, 44, 45, 178, 179] and experimental [180, 181] grounds. The underlying question is whether or not thermal protons can permeate through perfect 2D membranes. While the original experiments by Lozada-Hidalgo et al. report high permeability and isotope selectivity in the 2D defect-free materials [41-43], other experimental works either report improved results using chemical vapor deposited (CVD) 2D systems [180] or suggest that the proton flow penetrates through local defects rather than the defect-free graphene membrane [39, 181]. Recent nano-balloon tests unambiguously stated that there are no atomic-vacancy defects in the graphene used in the previous experiments [43]. However, other structural defect types without involving atomic vacancies are well-known for sp^2 carbon systems, such as grain boundaries, topological Stone-Wales (SW(55-77)) defects [126], and local hydrogenation, as shown in Figure 5.1.1. In particular, the SW(55-77) defect has been observed in mechanically exfoliated CVD graphene [182] and in graphene obtained by liquid phase exfoliation of graphite [183].

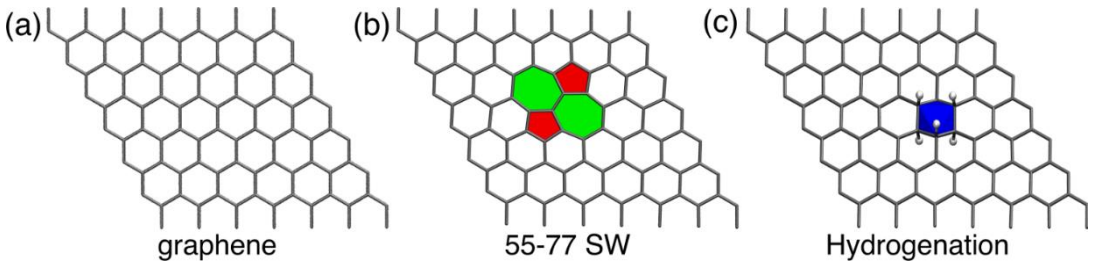

Figure 5.1.1 Structural representation of: (a) perfect graphene; (b) topological Stone-Wales (SW(55-77)) defect, and (c) hydrogenation of a 6-membered ring.

Several scenarios for the penetration of graphene by protons have been investigated theoretically to date [39, 44, 45, 178, 179], including defect-free graphene, atomic vacancy or topological defects, and partial hydrogenation of 6-membered rings (6MR, see Figure 5.1.1). Density-functional theory (DFT) calculations estimate transfer energy barriers (U_{max}) of about 1.4-1.6 eV for a proton passing through a pristine graphene sheet [36-38], in agreement with second order Møller–Plesset perturbation theory (MP2) (1.48 eV) [179], which indicates that graphene is essentially impermeable at ambient condition. Nuclear quantum effects (NQEs) correct the Born-Oppenheimer U_{max} to lower values [44, 178, 179, 184], for example, path-integral molecular dynamics (PIMD) accounts for a NQE-imposed barrier drop of 0.46 eV at 300 K [44].

The penetration barrier in graphene drops below 1 eV if some of its carbon atoms are hydrogenated and, thus, change their hybridization from sp^2 to sp^3 [44]. While there is a general agreement in the literature on the graphene penetration barriers for hydrogen and the nuclear quantum effects, only a few articles address the hydrogen isotope selectivity [178, 179, 184], and none of them offers a consistent picture explaining the experimental results that are available to date [41, 43, 186].

In this chapter, we calculated the flow of protons and their isotopes through graphene membranes and through the most common graphene defect sites. This allows the direct comparison of the permeability and the calculation of the corresponding selectivities. The models include, for comparison, pristine *h*-BN and, as principal target material, graphene as pristine membrane, with the topological SW(55-77) defect and with a locally hydrogenated ring. For each model, we first calculated the potential energy

surface (including U_{max}) on grounds of first-principles methods. The flow of protons (and their isotopes) is then estimated including quantum tunneling via the Wentzel–Kramers–Brillouin (WKB) approximation [53]. While we provide data for all three isotopes of hydrogen, including tritium for comparison, only the selectivities for the separation of H^+ and D^+ can be compared to the available experimental data and is, thus, the focus of this chapter. We show that the permeability of protons through perfect graphene is too low to generate appreciable particle flow, even though it would result in very high selectivities (much higher than reported in experiment). Local hydrogenation significantly lowers U_{max} but also reduces significantly the isotope selectivity to values much lower than those reported from experiment. On the other hand, we argue that the topological, vacancy-free SW(55-77) defect, with U_{max} below 1 eV and H^+-over-D^+ (H^+/D^+) selectivity of about 7, matches well the experimental findings by Lozada-Hidalgo et al. [41, 186] (see Figure 5.1.2). The H^+ flow through the 7MR ring is 10^6 times larger than that through the 6MR ring, indicating that, even if the concentration of such a defect was as low as 1 ppm, it would still govern the transport process in the graphene flake (and yet neither be detectable in the Raman spectrum nor in the nano-balloon test). These findings indicate that increasing the concentration of 7MRs in vacancy-defect-free sp^2 carbon structures are a promising route for the design of hydrogen-isotope-separation and potentially proton-exchange membranes.

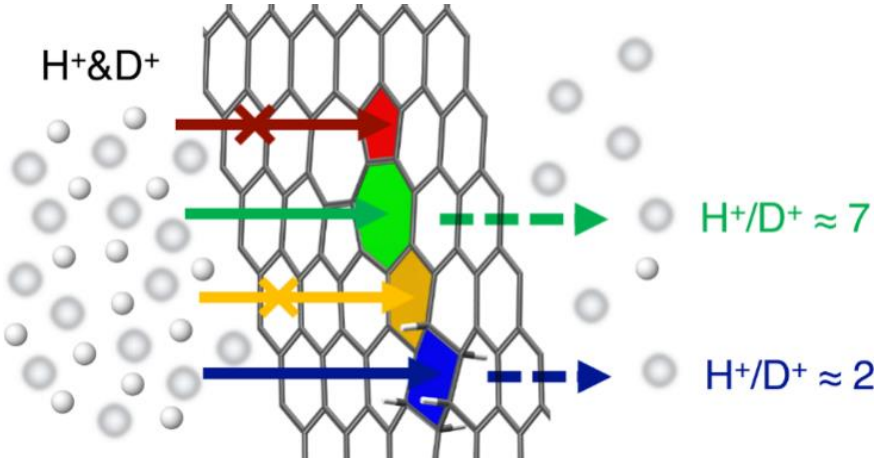

Figure 5.1.2 Schematic representation and summary of proton (H^+) and deuteron (D^+) transfer and separation through graphene with different carbon ring sizes. The most

plausible explanation of the high isotope selectivity is that 7-membered rings are present in the 2D membrane (green), as in the case of common SW(55-77) defects.

5.2 Methodology

By employing a one-dimensional (1D) transition state model, the transmission coefficients for quantum tunneling are calculated from Wentzel-Kramers-Brillouin (WKB) approximation [53]. When the energy E of a single particle is smaller than the maximum height of the barrier U_{max}, the transmission coefficient $T(E)$ can be described by:

$$T(E) = \exp\left\{-\frac{2}{\hbar}\int_{z_1}^{z_2}\sqrt{2m[U(z)-E]}dz\right\} \tag{5.2.1}$$

where z_1 and z_2 are the two turning points at which $U(z_1) = U(z_2) = E$.

Assuming that the particles are coming from infinite distance to the graphene membrane, by multiplying the kinetic energy distribution with the transmission coefficient $T(E)$, integrating over all the possible kinetic energies, the flow u of the particles tunnel through the potential barrier can be obtained:

$$u_{\text{tunnel}} = \sqrt{\frac{\beta}{2\pi m}}\int_0^{\infty}\exp(-\beta E)T(E)dE \tag{5.2.2}$$

where $\beta = 1/k_{\text{B}}T$, k_{B} is the Boltzmann constant and T is temperature.

For a given potential $U(z)$, the particle flow (u_{tunnel}) passing through the potential barrier that is contributed by quantum tunneling is expressed by:

$$u_{\text{tunnel}} = \sqrt{\frac{\beta}{2\pi m}}\int_{\infty}^{0}T(U(z))e^{-\beta U(z)}\frac{\partial U}{\partial z}dz \tag{5.2.3}$$

The classical particle flow is given as:

$$u_{\text{class}} = \frac{e^{-\beta U_{\max}}}{\sqrt{2\pi m\beta}} \tag{5.2.4}$$

The total particle flow passing through the potential barrier is given as:

$$u = u_{\text{class}} + u_{\text{tunnel}} = \frac{e^{-\beta U_{\max}}}{\sqrt{2\pi m\beta}} + \sqrt{\frac{\beta}{2\pi m}} \int_{\infty}^{0} T(U(z)) e^{-\beta U(z)} \frac{\partial U}{\partial z} dz \qquad (5.2.5)$$

The first term in Equation (5.2.5) corresponds to the classical particle flow, which is independent of tunneling, while the second term refers to the quantum tunneling contribution. In Section 5.4, we report results of both classical (u_{class}) and total (u) particle flows at 300 K to elucidate how much of quantum effects are involved in the transfer process of each particle.

5.3 Calculation Details

For graphene, pristine membrane and two possible defect types, the SW(55-77) and locally hydrogenated 6MR have been considered. They were studied on a coronene cluster model, which was carved from pristine graphene, as shown in Figure 5.3.1. Such a model was validated in earlier works [179]. The edge carbon atoms were saturated with hydrogen atoms to form a coronene molecule, as shown in Figure 5.3.1b. The SW(55-77) defect was created by rotation of one of the C-C bonds by 90° [126, 187], resulting in two pentagonal (5-membered) and two heptagonal (7-membered) rings (see Figure 5.3.1c). Periodic graphene models have also been considered for comparison, see the Section A4 of "Periodic supercell models" in Appendix.

For the trans-hydrogenation, one of the hexagonal (6-membered) rings was decorated with additional H atoms, changing hybridization of C atoms from sp^2 to sp^3 (see Figure 5.3.1d). Either two, four, or six H atoms were included, which correspond to the breaking of one, two, or all three π-bonds in one hexagonal ring. The lowest-energy H atom configuration in the 6MR is alternating on both sides, that is, two neighbouring C atoms have H atoms either above or below the cluster plane.

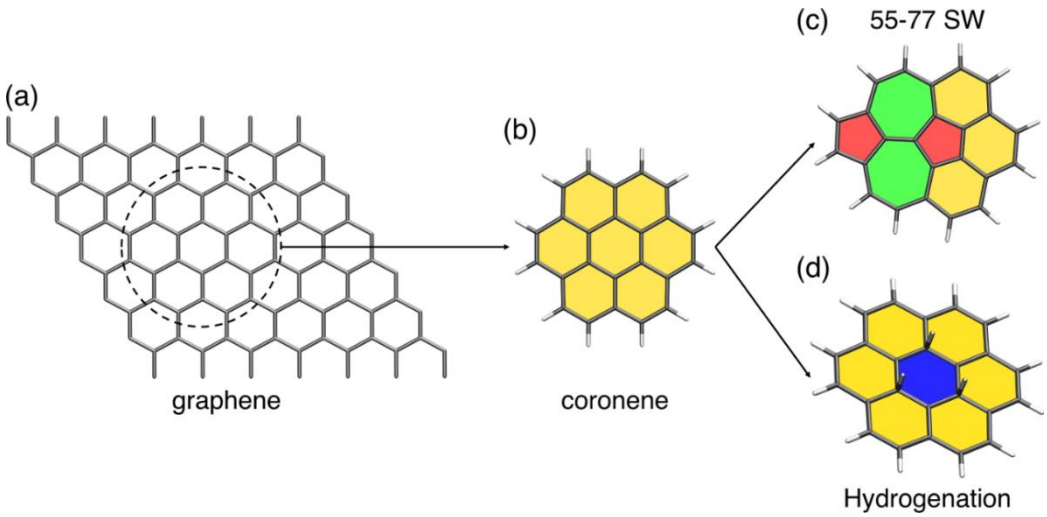

Figure 5.3.1 Carving a symmetrical fragment from the (a) periodic graphene sheet for computational models of: (b) coronene cluster model with 6MR (orange); (c) Stone-Wales (SW(55-77)) defect in the coronene cluster with two 5MR (red) and two 7MR (green); and (d) six H atoms hydrogenation (blue) of a 6MR ring in the coronene cluster.

For *h*-BN, as previous TEM and conductive AFM studies suggested that no defects or pinholes appear on *h*-BN [138], therefore, only perfect *h*-BN monolayer was studied. The *h*-BN monolayer was represented by the *h*-BN fragment cut from periodic *h*-BN, atoms on the edge were saturated with hydrogen atoms, as shown in Figure 5.3.2.

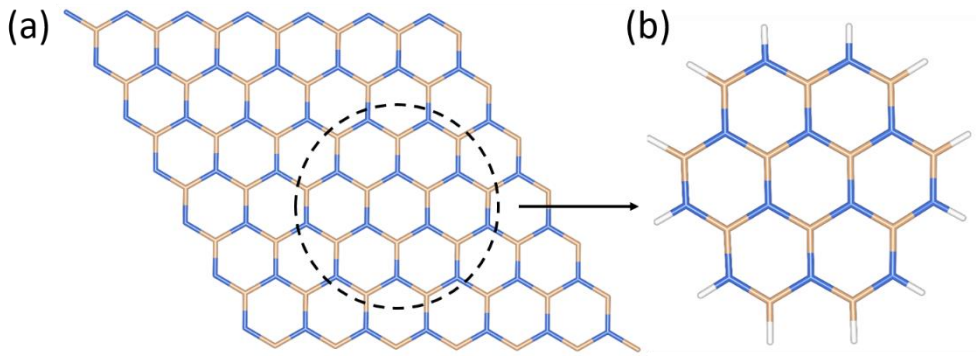

Figure 5.3.2 Carving a symmetrical fragment from the periodic *h*-BN sheet (a) for the computational model of *h*-BN cluster (b).

All structures were optimized using density-functional theory (DFT), employing the PBE0 functional [64, 68] and 6-31+G(d,p) basis set. The D3-(BJ) correction of London dispersion interactions following the approach of Grimme [76] was used as

implemented in Gaussian 09 package [188]. The benchmark calculations were carried out using DLPNO-CCSD(T) method, with cc-pvtz basis set and tight DLPNO thresholds, as implemented in ORCA 4.1 program [189].

In order to find the minimal potential energy barrier along the particles transfer path, a one-dimensional (1D) transition state model was employed. We assume the isolated particles follow a linear trajectory, moving from "vacuum" to the center of the graphene sheet on a path perpendicular to the basal plane. The transport path was defined by the vertical distance between the H^+/D^+ particle and graphene cluster, starting from 1.50 Å to −1.50 Å, with a step of 0.05 Å, with 0.00 indicating the particle in the ring center. The potential energy barriers (U_{max}) of a proton going through different types of rings in the cluster were calculated using single point energies on the optimized cluster structures. The schematic process is shown in Figure 5.3.3.

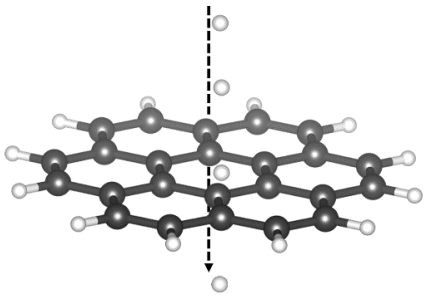

Figure 5.3.3 Schematic of calculating the PES of protons permeation through graphene.

5.4 Results

5.4.1 Hydron Isotope Permeate Through Graphene and *h*-BN Monolayers

First, we substantiated the results obtained using our density-functional theory (DFT) approach (PBE0/6-31+G(d,p)) with DLPNO-CCSD(T) calculations, which give an energy barrier of 1.58 eV for the H^+ to permeate through the central ring of a coronene cluster model (6MR). In our DFT method, this barrier is only slightly lower (1.41 eV).

We have calculated the energy profiles and the resulting transfer flow of H^+, D^+, and T^+ through the 5-, 6-, and 7-membered rings in a coronene flake model structure, and for a corresponding 6MR model of *h*-BN. The potential energy profiles of the cluster models are very similar to those obtained for a proton penetrating periodic graphene models calculated by us (for details, see Section A4 "Periodic supercell models" in Appendix) and Griffin et al. [190].

The potential energy profiles and the electron density isosurfaces at the transition state for each system are shown in Figure 5.4.1, while the corresponding flow of the isotopes are given in Table 5.4.1. The 5MR is impermeable, with U_{max} as high as 3 eV, and at the same time shows a very dense electron density in the ring centre (Figure 5.4.1b). Although the H^+/D^+ selectivity is very large, there is practically no proton flow through the membrane. The U_{max} reduces significantly to 1.41 eV for the 6MR and to 0.99 eV for the 7MR. At the same time, the electron densities at the ring centres decrease (Figure 5.4.1c and d). H^+/D^+ selectivities, calculated as ratios of the proton and deuteron flow, reduce to 66 for 6MR and to 7 for 7MR. The corresponding H^+/T^+ and D^+/T^+ selectivities are also given in Table 5.4.1. It should be noted, though, that the particle flow in the 7MR is 6 orders of magnitude higher than for the 6MR.

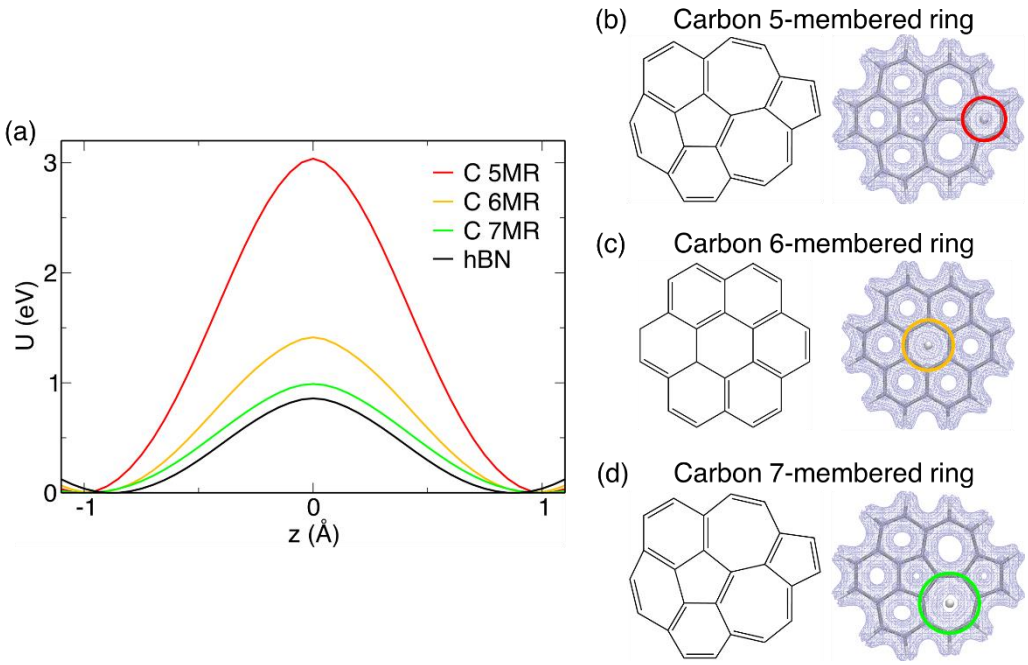

Figure 5.4.1 (a) The potential (U) as function of the distance between a particle and the 2D membrane (z) for the H^+ transfer through the carbon 5MR (red), 6MR (orange), and 7MR (green) in a coronene flake with a SW(55-77) defect. The potential is only considered between the minima, the increase beyond is due to the absence of solvent in our computational model. (b-d) The schematic models and the isosurfaces of H^+ transfer through the 5MR, 6MR, and 7MR, marked as red, black, and green circles, respectively. The value of each isosurface is set to 0.06. Note that U_{max} is at z = 0.

Table 5.4.1 The transfer energy barriers, U_{max} (calculated from Born-Oppenheimer approximation), the total (u) and the classical particle flow (u_{class}) for the H^+ and D^+ transfer at 300 K through 5MR, 6MR, and 7MR in a coronene flake with a SW(55-77) defect, and through *h*-BN 6MR. The particle flows are given in Hartree atomic units of length/time.

System		5MR	6MR	7MR	*h*-BN
U_{max} (eV)		3.04	1.41	0.99	0.90
H^+	u_{class}	2.71×10^{-55}	5.19×10^{-28}	6.86×10^{-21}	1.09×10^{-18}
	u	3.82×10^{-41}	2.34×10^{-25}	1.32×10^{-19}	2.11×10^{-17}
D^+	u_{class}	1.92×10^{-55}	3.67×10^{-28}	4.85×10^{-21}	7.71×10^{-19}
	u	9.13×10^{-51}	3.52×10^{-27}	1.91×10^{-20}	3.13×10^{-18}

T^+	u_{class}	1.57×10^{-55}	3.00×10^{-28}	4.00×10^{-21}	6.30×10^{-19}
	u	1.11×10^{-53}	1.35×10^{-27}	1.05×10^{-20}	1.71×10^{-18}
	$\frac{u_{H^+}}{u_{D^+}}$	4.2×10^{9}	66.5	6.9	6.7
	$\frac{u_{H^+}}{u_{T^+}}$	3.4×10^{12}	173.0	12.6	12.3
	$\frac{u_{D^+}}{u_{T^+}}$	823.0	2.6	1.8	1.8

It is worth noting that the experimentally detected H^+/D^+ selectivity of 10 was also obtained for *h*-BN monolayers. We have, therefore, applied the same method to the perfect *h*-BN, modelled as $B_{12}N_{12}H_{12}$ molecule, *h*-BN counterpart of coronene (no defects present), and we have obtained U_{max} of about 0.9 eV (in agreement with other work [178]) and a significantly higher particle flow than for the graphene 6MR with a selectivity of about 7 (Table 5.4.1), supporting our conclusions and the approach.

5.4.2 Influence of Hydrogenation

Since the experiments were performed in aqueous medium (Nafion), local hydrogenation of the 6MR in graphene was suggested as possible reason for the high proton transfer rates [44, 45]. Indeed, hydrogenation changes the local hybridization of C atoms from sp^2 to sp^3, makes the rings locally non-planar, somewhat increases the ring size (the C-C bond length increases by about 7%), and reduces the electron density inside the ring, due to removal of π electrons. Therefore, the particles experience weaker repulsion from the carbon atoms in the ring. This results in lowering of U_{max} for particles to about 0.7 eV for the full hydrogenation of a single 6MR as shown in Figure 5.4.2. For the 6MR+6H model, a double maximum shape of the PES is obtained (Figure 5.4.2a). In this case, at each side of the ring, the 3 H atoms impose a steric barrier, resulting in two maxima in the PES at |z| = 0.65 Å. The potential barrier at z = 0 is due to the carbon 6MR.

Addressing the energetics of the formation of such defects is beyond the scope of this chapter and we concentrate on a possible proton transfer and isotope selectivity through hydrogenated graphene. While values of U_{max} are lowered and the individual particle flows increase, as Table 5.4.2 shows, there is almost no quantum tunneling observed, even not for the protons. This suggests hydrogenation is most probably not relevant for proton and deuteron transfer due to the strongly suppressed quantum effects and the resulting very small selectivity (around 2 or less). The corresponding H^+/T^+ and D^+/T^+ selectivities are also reported for comparison.

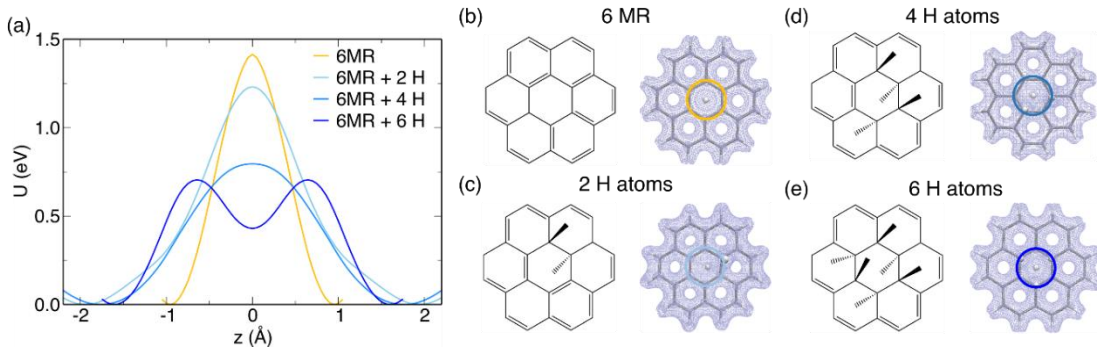

Figure 5.4.2 (a) The potential (U) as function of the distance between a particle and the 2D membrane for the H^+ transfer through the perfect 6MR (yellow), 2 H atom (light blue), 4 H atom (medium blue), and 6 H atom (dark blue) hydrogenated 6MR in the coronene flake. The potential is only considered between the minima, the increase beyond is due to the absence of solvent in our computational model. (b-d) The schematic models and the isosurfaces of H^+ transfer through the 6MR and 6MR with 2, 4, and 6 H atoms, marked as yellow and different blue circles, respectively. The value of each isosurface is set to 0.06. Note that U_{max} is at z = 0.

Table 5.4.2 The transfer energy barriers, U_{max} (calculated from Born-Oppenheimer approximation), the total (u) and the classical particle flow (u_{class}) of the particles at 300 K through the pristine 6MR and through 2H-, 4H- and 6H-trans-hydrogenated coronene flake. The particle flows are given in Hartree atomic unit of length/time.

System	**6MR**	**2H-trans hydrogenated**	**4H-trans hydrogenated**	**6H-trans hydrogenated**

$U_{\max}$ (eV)		1.41	1.23	0.79	0.70
H^+	u_{class}	5.19×10^{-28}	6.12×10^{-25}	1.27×10^{-17}	4.14×10^{-16}
	u	2.34×10^{-25}	3.04×10^{-24}	2.10×10^{-17}	9.72×10^{-16}
D^+	u_{class}	3.67×10^{-28}	4.33×10^{-25}	9.01×10^{-18}	2.93×10^{-16}
	u	3.52×10^{-27}	1.03×10^{-24}	1.24×10^{-17}	4.58×10^{-16}
T^+	u_{class}	3.00×10^{-28}	3.53×10^{-25}	7.36×10^{-18}	2.39×10^{-16}
	u	1.35×10^{-27}	6.75×10^{-25}	9.42×10^{-18}	3.31×10^{-16}
$\frac{u_{H^+}}{u_{D^+}}$		66.5	3.0	1.7	2.1
$\frac{u_{H^+}}{u_{T^+}}$		173.0	4.5	2.2	2.9
$\frac{u_{D^+}}{u_{T^+}}$		2.6	1.5	1.3	1.4

5.4.3 Discussions

Our results show that the $U_{\max}$ of particle transfer (protons and their isotopes) through a 2D membrane of graphene reduces if the ring size is enlarged, as in the cases of the SW(55-77) defects or hydrogenation of carbon atoms. Our calculated $U_{\max}$ of 1.41 eV for the 6MR and 0.99 eV for the 7MR are in close agreement with previous theoretical studies [178, 179]. The 7MR barrier of ~1eV is closest to the experimentally reported value [40, 41].

The selectivity is calculated as ratio of the isotope flows (see Section 5.2) and thus eliminates systematic errors in the approach. An increase of the ring size lowers the transmission barrier and, consequently, the H^+/D^+ selectivity, which is around 66 in the 6MR, while it is only around 7 in 7MR. The latter value is reasonably close to the

experimental value of 10 [41, 186]. A perfect graphene membrane would show a significantly lower deuteron flow. The fact that the selectivity slightly drops to 8 for a CVD-grown graphene [186] (which is expected to have grain boundaries, typically involving 7MR) further supports our hypothesis.

Lozada-Hidalgo et al. [41] rationalize the high isotope selectivity of the graphene membranes with the 60 meV difference in binding energy of deuterons and protons to water in the Nafion film. Fed into Arrhenius equation, this results in a selectivity of about 10 at room temperature, fitting to the experimental observation. However, with that argumentation, the selectivity would be independent of the membrane itself. As we have shown here, the selectivity is due to the tunnel effect when the hydrons penetrate through the graphene membrane.

Hydron isotope tunneling through defect-free *h*-BN and graphene has already been reported on grounds of WKB approximation followed by application of the empirical Arrhenius equation [178, 184]. The latter step is, however, not necessary for the calculation of isotope selectivities, which can be directly obtained as quotient of the isotope particle flows. This direct approach gives significantly larger selectivities (66 vs. 16…30 for graphene [178, 184], and 10 vs. 2-4 for *h*-BN [178]).

The huge increase of particle flow for the 7MR (by more than 6 orders of magnitude compared to the 6MR) indicates that even for a concentration on the ppm scale, 7MRs govern the proton transfer process. For Raman spectroscopy, a typical quality control experiment, the detectable concentration limit of topological SW(55-77) defects in a graphene monolayer is about 2×10^9 cm^{-2} [191-193], well above the ppm-scale concentration of 7MR that is needed to govern the proton transfer. At the same time, our conclusions are in agreement with a recent experiment by Lozada-Hidalgo and co-workers [43], which showed that the membranes employed in earlier experiments are free of vacancy defects. Vacancy defects and their energy barriers have been discussed in the literature by others [39]. They are typically significantly lower than the 7MR defect (e.g., 0.68 eV for OH-saturated vacancy defects [39]). As the thickness of the

membrane is the same, this will result in much lower selectivity than for the hydrogenated rings discussed here.

Moreover, we find that local hydrogenation of graphene is most probably not relevant for proton and deuteron transfer due to the strongly suppressed quantum effects and the resulting very small selectivity (around 2 or less).

The calculated selectivities towards tritium suggest that graphene may be useful for enriching tritium concentrations in contaminated water (H^+/T^+ selectivity is 12 at ambient condition), but hardly suitable to capture tritium from contaminated heavy water (D^+/T^+ selectivity is 1.8).

5.5 Revisit Arrhenius Equation

Quantum tunneling essentially lowers the energy barrier when protons through 2D membranes. It is instructive to know the effective energy barrier after taking quantum tunneling into consideration. To this end, we calculated the effective Arrhenius activation energy that includes quantum tunneling.

In a reaction, the experimental rate constant (k_r) and the inverse temperature ($1/k_{\mathrm{B}}T$) is usually connected by the empirical Arrhenius equation,

$$k_r = A\exp(-E_{\mathrm{a}}/k_{\mathrm{B}}T) \tag{5.5.1}$$

where A is the pre-exponential factor that describes an additional empirical dependence due to the collision frequency orientation, E_{a} is the Arrhenius activation energy, k_{B} is Boltzmann constant and T is temperature. In Section 5.2, Equation (5.2.5) gives the total particle flows u permeating through graphene. According Tkatchenko and co-workers [184], the average transmission probability k can be described from:

$$k = \sqrt{2\pi m\beta}u = e^{-\beta U_{\max}} + \int_{\infty}^{0} T(U(z))e^{-\beta U(z)}\frac{\partial U}{\partial z}dz \tag{5.5.2}$$

Combing Equation (5.5.1) and (5.5.2), the effective Arrhenius activation energy E_a that includes quantum tunneling is expressed by:

$$E_a(\beta) = -\frac{\partial lnk(\beta)}{\partial \beta} = \frac{U_{max}e^{-\beta U_{max}} + \int_{\infty}^{0} T(U)e^{-\beta U}(\beta U - 1)\frac{dU}{dz}dz}{e^{-\beta U_{max}} + \beta \int_{\infty}^{0} T(U)e^{-\beta U}\frac{dU}{dz}dz} \qquad (5.5.3)$$

Equation (5.5.3) gives the relationship of the effective Arrhenius activation energy includes quantum tunneling with different potentials. Utilizing the PESs of proton permeating through 5MR, 6MR and 7MR from BO-DFT calculations, plugging them into Equation (5.5.3), the effective Arrhenius activation energies $E_a(\beta)$ includes quantum tunneling at 300 K for hydron isotope permeating through 5MR, 6MR and 7MR are 0.47 eV, 0.80 eV and 0.76 eV, respectively. For comparison, the original energy barriers without quantum from BO-DFT are 3.04 eV (5MR), 1.41 eV (6MR) and 0.99 eV (7MR).

We notice that although the 5MR has the highest BO-DFT energy barrier (3.04 eV) among the three ring sizes, its effective Arrhenius activation energy (0.47 eV) is much lower than the ones of 6MR (0.80 eV) and 7MR (0.76 eV), which is unexpected and unphysical at all. This unrealistic value of effective Arrhenius activation energy for 5MR invites us to explore more PESs, to investigate the relationship of original energy barriers (here from DFT) without quantum tunneling and the effective Arrhenius activation energies (calculated from the Equation (5.5.3)) include quantum tunneling. Therefore, we engineered the original PESs of 5MR, 6MR and 7MR from DFT calculations by scaling their energy barrier heights U_{max} with different scaling factors f (varies from 0.2 to 2), the widths of the scaled PESs stay the same as the original ones. Figure 5.5.1a-c shows a branch of the scaled PESs, and they were then utilized to calculate the effective Arrhenius activation energies by employing the Equation (5.5.3), the relationship the effective Arrhenius activation energies and the scaled U_{max} are shown in Figure 5.5.1d-f.

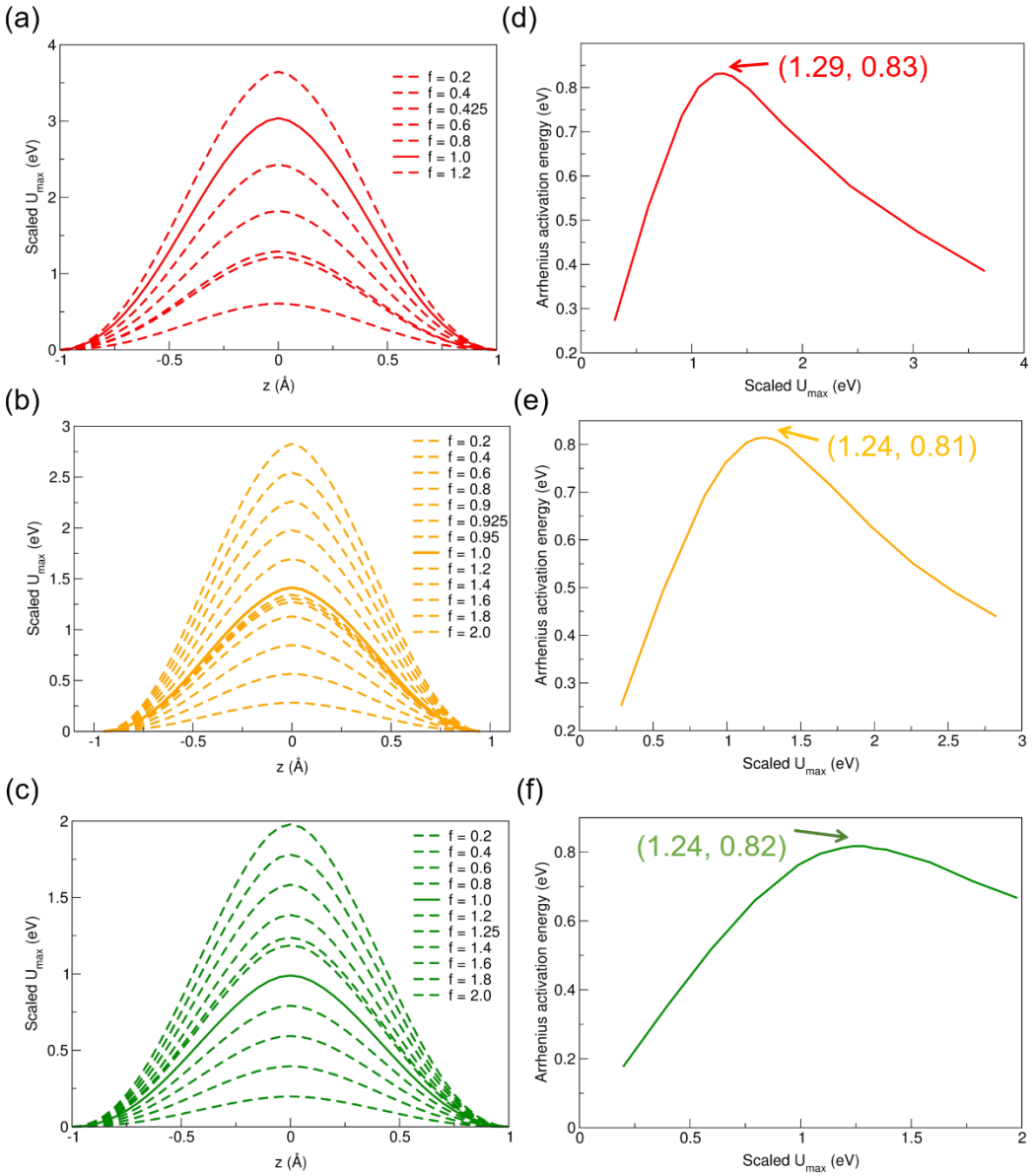

Figure 5.5.1 Scaled PESs for 5MR (a), 6MR (b) and 7MR (c) with different scaling factors *f*, the original PES for each system are represented as solid lines, the scaled ones are in dash lines. (d)-(f) are the effective Arrhenius activation energies include quantum tunneling (y axis) versus the scaled energy barriers U_{max} without quantum tunneling (x axis), temperature is set at 300 K.

Apparently, the effective Arrhenius activation energies include quantum tunneling are all smaller than the original barriers U_{max}, as quantum tunneling lowers the energy barrier. However, the weird behavior is a vertex appears in Figure 5.5.1d-f. For instance, in the scenario of 5MR (see Figure 5.5.1d), when U_{max} is smaller than 1.29 eV, the effective Arrhenius activation energy increases positively with U_{max}, which is as

expected — larger original barrier (U_{max}) corresponds larger effective Arrhenius activation energy. However, when U_{max} is larger than 1.29 eV (at the right side of the vertex), the effective Arrhenius activation energy decreases with the increasing U_{max}— larger U_{max} correspond lower effective Arrhenius activation energies, which is unphysical at all. Similar phenomena appear in the cases of scaled 6MR (Figure 5.5.1e) and 7MR (Figure 5.5.1f), when U_{max} is larger than 1.24 eV, the unphysical behavior starts.

To find out why such weird vertex appears in the cases, we revisited the Arrhenius equation. Previous study [194] demonstrated that when quantum effects play a significant role (for example, at low temperature) in the reactions, nonlinear Arrhenius graph could be observed. In particular, the curvature were found in the reactions that involve hydrogen atom (H) or proton (H^+). Figure 5.5.2 presents the plots of transmission probability k for each isotope (H^+, D^+ and T^+) vs. the inverse of temperature (1000/T) for the 5MR, 6MR and 7MR systems, the temperature range is 200-1000 K.

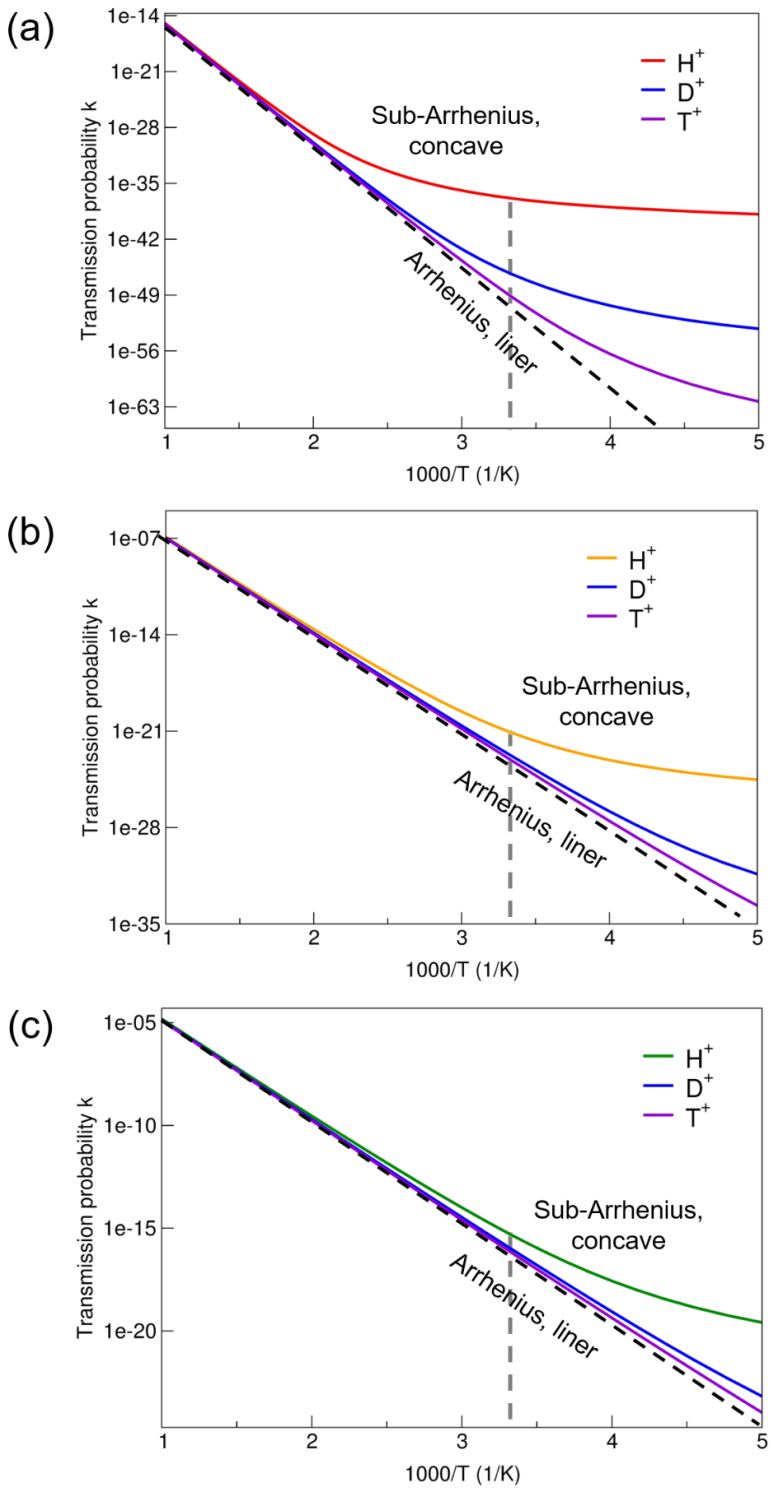

Figure 5.5.2 The transmission probability *k* of different hydron isotopes (H^+, D^+ and T^+) as a function of inverse temperature (1000/*T*) for the cases of 5MR (a), 6MR (b) and 7MR (c). The concaved lines indicate the role of quantum tunneling. The black dashed lines represent the liner behavior of Arrhenius plots, grey dashed lines point to the temperature at 300 K.

The sub-Arrhenius concave (usually associated with quantum tunneling effect) [195] was observed in Figure 5.5.2. Especially, in the case of 5MR, when the temperature is around 500 K, the curvature in the plot of H^+ already becomes quite strong. For 6MR, at 300 K, the Arrhenius graph of H^+ shows a trend of curvature as well, which means Arrhenius equation is not applicable in the case of 6MR either. In 7MR, at 300 K, the Arrhenius plot is normally behaved.

When U_{max} is high, such as in the cases of 5MR and 6MR, where the original energy barrier is 3.04 eV and 1.41 eV, it is impossible for such reactions happen at classical cases, but there is still a finite possibility for the protons to tunnel through the energy barriers due to quantum tunneling. In other words, in the reactions with high energy barriers and quantum tunneling plays a significant role, the classical Arrhenius equation is inapplicable (e.g., in the scenarios of 5MR and 6MR), due to their high original energy barriers. This explains the weird vertex in Figure 5.5.1, when U_{max} is too high, the Arrhenius equation fails. Therefore, to employ Arrhenius equation in a reaction where quantum tunneling plays an important role, the energy barrier of the reaction should below 1.2 eV, otherwise inaccurate effective Arrhenius activation energies would be obtained because of quantum tunneling.

Now let us come back to see the effective whether or not we can get effective Arrhenius activation energies of each proton isotope permeation through graphene. As demonstrated in Section 5.4, protons are indeed tunnel through the 7MR, with the original barrier U_{max} 0.99 eV. Hence, in the case of 7MR, it is safe to apply Arrhenius equation to obtain effective activation energies includes quantum tunneling. We find that these effective energies for H^+ and D^+ through 7MR are 0.76 eV and 0.92 eV, respectively; dropped by 0.23 eV and 0.07 eV from BO-DFT energy barriers without quantum tunneling.

5.6 Conclusions

In summary, combining the results of calculations of the energy barriers (U_{max}), transfer

flow of the particles, and the isotope selectivity, the most plausible hypothesis for the hydron isotope transfer through atomically thick graphene membranes is that the process is governed by tunneling through 7-membered rings in the topological (vacancy-free) Stone-Wales (SW(55-77)) defects and in grain boundaries. SW(55-77) defects significantly lower the penetration barrier for hydrogen through graphene: the proton flow through a seven-membered ring is a million times higher compared to a ring in the pristine honeycomb lattice, and yields an H-over-D selectivity of 7 at ambient condition. Our results well explain the recently reported experiment on hydrogen isotope separation on defect-free graphene. Even a presence in a ppm-scale concentration (in absence of vacancy defects) makes 7MR the dominant contributor for proton flow and, thus, governs the hydrogen isotope selectivity. Better membranes would include a large concentration of 7MR in absence of other defects. Hydrogenation lowers the energy barrier but decreases the selectivity meanwhile due to the strongly suppressed quantum effects. Additionally, when applying the empirical Arrhenius equation in the H/H^+ involved reactions where NQE plays a significant role, the energy barriers for these reactions should be lower than 1.2 eV, otherwise it would lead to inaccurate effective activation energies because of quantum tunneling.

6. Graphdiyne Monolayer as Efficient Quantum Sieve for Helium Isotopes

In the previous chapter, we show that quantum tunneling plays a critical role for separating hydron isotopes using 2D graphene and *h*-BN monolayers. This success challenged us to search for other 2D materials with ideal pore size to serve as quantum sieves. Except hydrogen, the demand of other isotopes is also growing, such as light helium isotope (^{3}He). To this end, in this chapter, we aim to separate light ^{3}He with one-atom-thick carbon allotrope of graphyne (GY) [47, 48] and graphdiyne (GDY) [49-51] nanoporous materials. The uniformly distributed pores of GY and GDY render themselves promising for separating gas molecules [196], and even isotopes [197, 198]. Yet, how pure quantum tunneling would influence the permeation of helium isotopes through these materials needs to be further investigated, as studied in this chapter[2].

6.1 Introduction

The light isotope of helium—^{3}He, is in growing demand in various of fields, for instance, in cryogenic industries [199], neutron-scattering facilities, and the basic research chemistry and physics [200]. The rareness of ^{3}He in nature renders itself being extremely difficult to be enriched. The conventional approach for harvesting ^{3}He is to skim the tritium reserves and capture ^{3}He as a byproduct of the radioactive tritium decay [201]; nevertheless, the production capability for such technique is excessively limited. In order to meet the increasing demand of ^{3}He, alternative approaches for its harvest is

[2] Data and contents presented here are in preparation for publication.

urgently needed.

Two-dimensional (2D) materials, such as graphene and *h*-BN monolayers, have been demonstrated promising for separating hydron isotopes with high H^+/D^+ selectivity around 10 [41], which is much more efficient than the conventional separation methods [15]. To serve as good quantum sieves, the pore size of 2D nanomaterials, which corresponds for the balance between the permeability and the selectivity of isotopes, is crucial. Because on one hand, larger pore size corresponds smaller energy barriers, the particles can, therefore, permeate through the membranes easier, with greater particle flow; on the other hand, however, according to the kinetic quantum sieving (KQS) [21], increasing the radius of pore would dramatically reduce nuclear quantum effect (NQE), which would strongly decrease the selectivity of the isotopes. Combing these two competing factors together, good candidates for quantum sieving should meet the permeation and separation of the isotopes at the same time, with proper pore sizes.

Most of carbon-based materials only contain sp^2- or sp^3-hybridized carbon atoms, such as graphene (sp^2-hybridized) and diamond (sp^3-hybridized). Yet, the existence of ethynyl units could substantially affect the properties of materials [202, 203]. In the past decades, intensive studies [48, 204-207] were focused on investing the sp-hybridized materials. In 1987, Baughman et al. [47] initially proposed that graphyne (GYs) family would be a series of stable carbon allotropes which are highly sp-hybridized. GYs are composed from benzene rings and acetylenic linkages; according to the number of acetylenic linkers, GYs are divided as graphyne (GY), graphdiyne (GDY), graphtriyne (GTY), and so forth [49]. The high degree of π-conjunction in the GYs with consistently formed pores providing them potential applications in many fields. For instance, previous studies have shown that GDY is promising in separating gas molecules [196] and isotopes [197]. However, whether other GYs can serve as isotope sieves is not clear; and how pure quantum tunneling affects helium isotope separation via GYs needs to be further investigated. In this chapter, on the basis of first-principles calculations, we investigate helium isotope (^{3}He and ^{4}He) separation through

GY and GDY monolayers. By calculating the potential energy surface (PES) of each system, we rule out GY membrane serving as quantum sieve for helium isotopes, due to the high energy barrier it provides. On the other hand, GDY shows a very low energy barrier and is highly permeable to helium isotopes. Nevertheless, in order to separate ^{3}He and ^{4}He efficiently, only at cryogenic temperature, when kinetic energies of the particles are tiny and quantum tunneling plays a significant role, can helium isotopes be separated effectively. For example, at the cryogenic temperature of 15 K, the selectivity of ^{3}He/^{4}He via GDY can be as high as 18.

6.2 Models and Methods

We have built 3×3 supercell of GY and GDY, the optimized structures are shown in Figure 6.2.1. The lattice constants after full optimizations are 6.89 Å and 9.47 Å for GY and GDY, respectively, in good agreement with previous studies [208, 209]. GY has one acetylenic linker (sp-hybridized carbon) between the two benzene rings while GDY has two, which yields GY has smaller van der Waals (vdW) surface than GDY. Different types of bonds exist in GYs: the aromatic bonds (sp^2-hybridized), the single carbon bonds linking adjacent C-C bonds (sp-sp^2-hybridized), and the triple C≡C bonds (sp-hybridized). The calculated bond lengths are shown in Table 6.2.1, which are consistent with former works [208, 209].

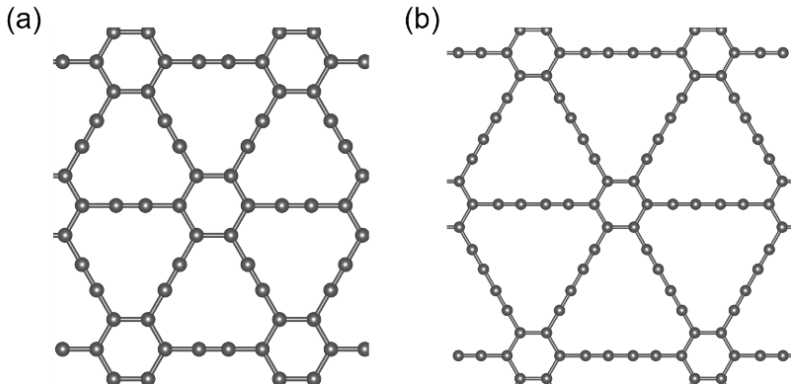

Figure 6.2.1 Structures of GY (a) and GDY (b) monolayers.

Table 6.2.1 Optimized bond length in GY and GDY.

Structure	C_{sp2}-C_{sp2} (Å)	C_{sp2}-C_{sp} (Å)	C_{cp}-C_{sp} (Å)	C_{sp}-C_{sp2} (Å)
GY	1.43	1.41	1.22	-
GDY	1.43	1.40	1.23	1.34

All the calculations were carried out using density-functional theory (DFT) with Perdew-Burke-Ernzerhof [64] (PBE) functional, as implemented in the *CP2K 6.0* package [171]. D3 correction of vdW interactions following the approach of Grimme [76] was applied. The Quickstep method was employed, with Goedecker-Teter-Hutter [172] (GTH) pseudopotentials together with DZVP-MOLOPT-GTH-SR basis set for carbon atoms; helium was treated with the DZVP-all electron basis set and all-electron potential. The plane-wave energy cutoff was set to 550 Ry.

Similar to the PES that calculated in Chapter 5, here we also employ one-dimensional (1D) transition state model. Assuming the isolated helium particles moving from vacuum to the center of the GYs plane perpendicularly. The transport path with the minimal potential energy barrier was defined by the vertical distance between the ^{3}He or ^{4}He particle and the GYs membrane, starting from 3.0 Å to -3.0 Å, with a step of 0.05 Å.

At cryogenic temperature, quantum tunneling would be significant for the permeation and separation. Since the kinetic energy *E* would be very small at cryogenic temperature, we calculate the transmission coefficient *T(E)* for the tunneling by employing Wentzel-Kramers-Brillouin (WKB) approximation [53],

$$T(E) = \exp\left\{-\frac{2}{\hbar}\int_{z_1}^{z_2}\sqrt{2m[U(z)-E]}dz\right\} \tag{6.2.1}$$

where z_1 and z_2 are the turning points at which $U(z_1) = U(z_2) = E$.

Assuming that the helium particles coming from infinite distance to the GYs membrane, by multiplying the kinetic energy distribution with the transmission coefficient $T(E)$, integrating over all the possible kinetic energies, the particle flow u tunneling through

the potential barrier is described as:

$$u = \sqrt{\frac{\beta}{2\pi m}} \int_0^{\infty} \exp(-\beta E) T(E) dE \tag{6.2.2}$$

where $\beta = 1/k_B T$, k_B is the Boltzmann constant, and T is temperature.

For a given potential $U(z)$, the particle flow (u_{tunnel}) passing through the potential barrier that is contributed by quantum tunneling is expressed as:

$$u_{\text{tunnel}} = \sqrt{\frac{\beta}{2\pi m}} \int_{\infty}^{0} T(U(z)) e^{-\beta U(z)} \frac{\partial U}{\partial z} dz \tag{6.2.3}$$

The classical particle flow is given as:

$$u_{\text{class}} = \frac{e^{-\beta U_{\max}}}{\sqrt{2\pi m \beta}} \tag{6.2.4}$$

Therefore, the total particle flow passing through the potential barrier is expressed by:

$$u_t = u_{\text{class}} + u_{\text{tunnel}} = \frac{e^{-\beta U_{\max}}}{\sqrt{2\pi m \beta}} + \sqrt{\frac{\beta}{2\pi m}} \int_{\infty}^{0} T(U(z)) e^{-\beta U(z)} \frac{\partial U}{\partial z} dz \tag{6.2.5}$$

The ratio for the total particle flow (u) of ^{3}He and ^{4}He through the membrane determines the selectivity of ^{3}He/^{4}He.

6.3 Results

Figure 6.3.1 and Figure 6.3.2 depict the scenarios of helium permeate through GY and GDY membrane, respectively. The energy barrier for helium permeate through GY is 1.84 eV (see Figure 6.3.1d) while is only 0.048 eV for GDY (see Figure 6.3.2d). The huge energy barrier (1.84 eV) of GY indicates that it can be ruled out for separating helium isotopes. Therefore, hereafter this chapter, only GDY is reported for helium isotope separation.

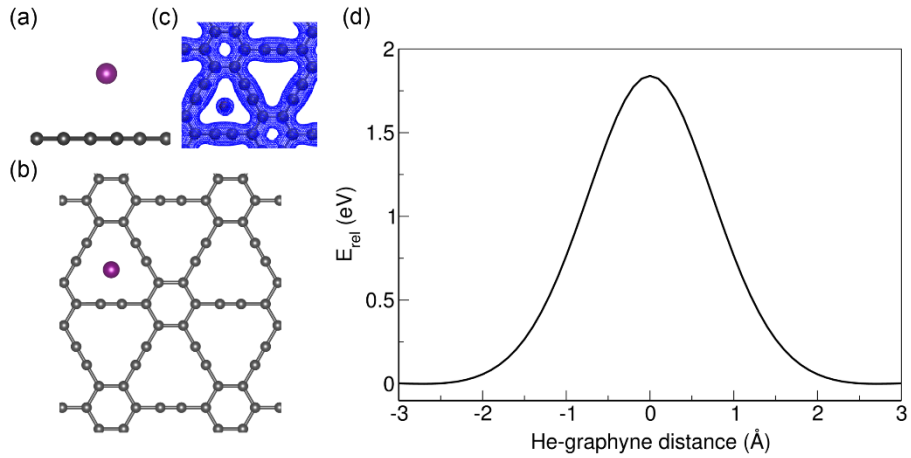

Figure 6.3.1 (a) Side and (b) top views of He transfer through GY membrane; (c) Electron density isosurface (the value of isosurface is set to 0.06) and (d) potential energy surface (PES) of He through GY plane.

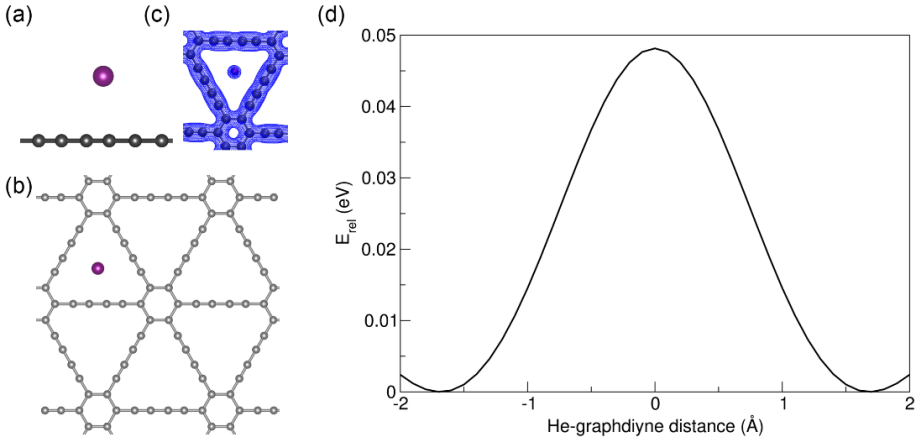

Figure 6.3.2 (a) Side and (b) top views of He transfer through GDY plane; (c) Electron density isosurface (the value of isosurface is set to 0.06) and (d) potential energy surface (PES) of He through GDY membrane.

The small energy barrier and the wide PES (3.4 Å) of helium isotope permeate through GDY increase the difficulty to separate them—only at low temperature, the effect of quantum tunneling is large enough for efficient separation. Figure 6.3.3 presents the calculated particle flow of ^{3}He and ^{4}He through GDY, at the temperature range of 10-80 K, the ratio of ^{3}He/^{4}He flow is given in Figure 6.3.4.

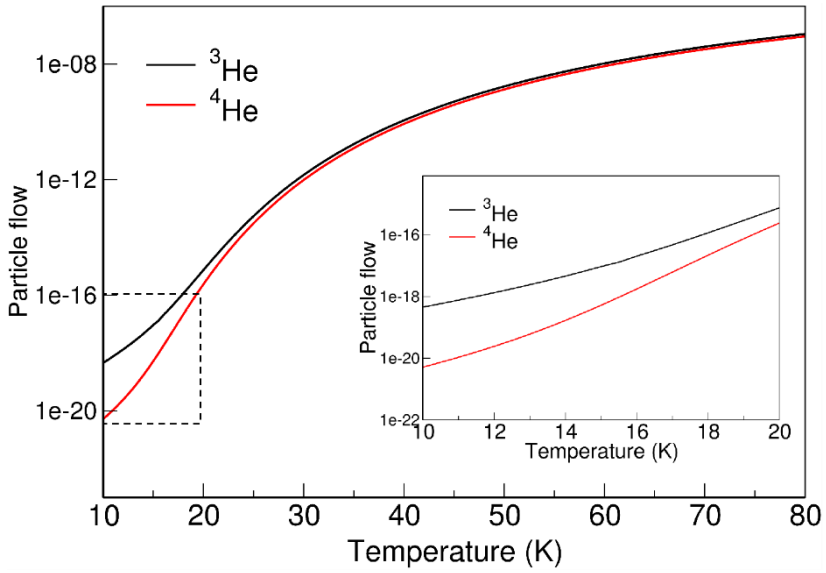

Figure 6.3.3 Particle flows of ^{3}He (black) and ^{4}He (red) through GDY monolayer at the temperature range of 10-80 K; inset is the particle flows at 10-20 K.

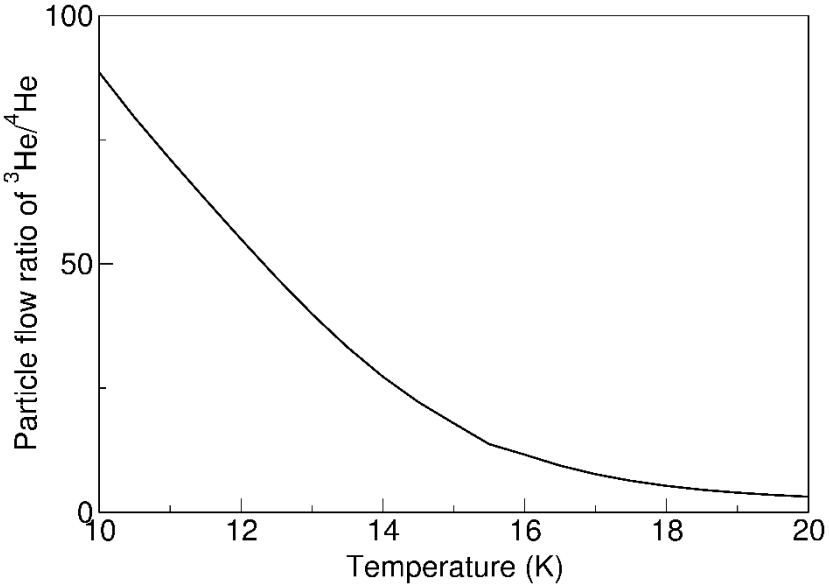

Figure 6.3.4 The particle flow ratio of ^{3}He/^{4}He at 10-20 K.

Figure 6.3.3 shows that the particle flows of lighter ^{3}He are always larger than that of the heavier ^{4}He at all the temperature range, for the reason that quantum tunneling favors lighter particles with larger transmission probabilities. Increasing temperature resulting in the increase of the particle flows as well, for instance, the flow of ^{3}He is only 10^{-19} at 10 K, but it dramatically increases to 10^{-7} at 80 K. Yet, quantum tunneling decreases strongly with high temperature. The selectivity of ^{3}He/^{4}He, therefore, largely

reduced as temperature increasing. At 80 K, for example, the selectivity of ^{3}He/^{4}He drops to only 1.2. To get an acceptable separation factor above 3, the temperature should be below 20 K, as shown in Figure 6.3.4. The classical and total flow of ^{3}He and ^{4}He through GDY at moderate 15 K are given in Table 6.3.1, from which one can see that GDY shows a high ^{3}He/^{4}He selectivity of 17.89 with the large ^{3}He flow of 10^{-17}.

Table 6.3.1 The classical and total flow of ^{3}He and ^{4}He through GDY at 15 K, the particle flows are given in Hartree atomic unit of length/time.

System		GDY
$U_{\max}$ (eV)		0.048
^{3}He	u_{class}	2.47×10^{-21}
	u	9.27×10^{-18}
^{4}He	u_{class}	2.14×10^{-21}
	u	5.18×10^{-19}
$\frac{u_{3\text{He}}}{u_{4\text{He}}}$		17.89

6.4 Conclusions

In summary, we showed that GDY has great potential for capturing ^{3}He effectively at cryogenic temperature while GY is incapable to sieve helium isotopes, due to their van-der-Waals (vdW) surface differences. The large pore size of GDY enables helium isotope permeate through the membrane easily with large particle flow; meanwhile however, such large pore size of GDY limits that only at cryogenic temperature, the effect of quantum tunneling is large enough to separate ^{3}He efficiently. As temperatures get higher, although the particle flows increase, the influence of quantum tunneling

decreases dramatically, which reduces the selectivity correspondingly. To get an industrial acceptable separation factor, the temperature range should be below 20 K. At the moderate 15 K, GDY provides a high $^{3}He/^{4}He$ selectivity around 18.

7. Concluding Remarks

7.1 Summary

In this thesis, three theoretical challenges are solved: (1) identifying the transported hydrogen particles inside interstitial space of layered materials, and revealing their transport mechanisms; (2) investigating the influence of quantum tunneling and topological Stone-Wales-55-77 defects in the process of hydron isotope separation through 2D graphene and *h*-BN monolayers; and (3) harvesting the light helium (^{3}He) using 2D graphdiyne membrane.

In part I of this work, we show that it is protium atoms, rather than protons, are transported in the interstitial space of layered materials. Protiums hop between two adjacent layers on the crystals, following a zigzag manner. The transport is additionally supported by the typical interlayer shear modes in layered materials. Yet, the concentration of protiums must be low, otherwise they will come close to each other and recombine to H_2 molecules. For layered MoS_2, both of proton and protium bounds to sulfur atom in MoS_2 lattice, and transported on a zigzag path with very similar free energy barriers. The common sulfur defect in MoS_2, however, strongly hinders the transport of the particles, making layered MoS_2 inferior to *h*-BN with respect to hydrogen conduction. In addition, for metallic graphite, hydrogen is immobile in its interstitials, due to the strong C-H bond strength. In general, part I of this thesis provides novel perspectives of hydrogen particle transport inside layered materials, as well as approach obtaining free energy barriers for particle diffusion.

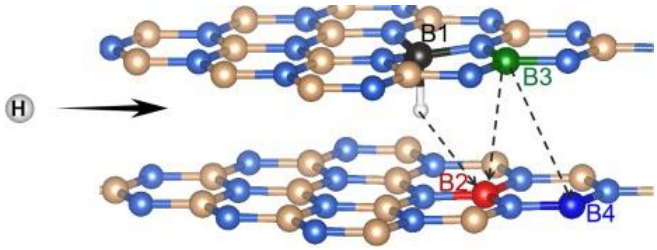

Whether or not pristine graphene allows hydron isotopes to permeate through was a controversial topic during the past few years, both on theoretical and experimental grounds. In part II of this thesis, we show that pristine graphene is quasi-impermeable to protons; yet they can permeate through the most common defect in sp^2 carbons—the topological Stone-Wales (SW(55-77)) defect, with energy barrier below 1 eV and H^+/D^+ selectivity of 7. Even such defect is in the ppm-scale concentration, it still is the dominant contributor for proton flow. Our results actually agree with a very recent work by Griffin et al. [190], which shows disordered graphene enhances proton permeability. In addition to reveal the mechanism of hydron isotope separation through 2D membranes, our work also provides an efficient tool to estimate the influence of quantum tunneling for any symmetric PES. Finally, we find that utilizing pure quantum tunneling at low temperature, 2D graphdiyne can separate helium isotopes efficiently.

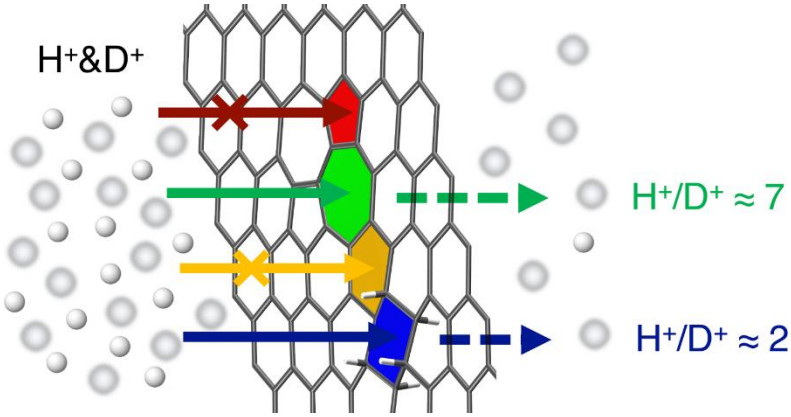

For future applications, in order to improve the performance of separating hydron isotopes, one can consider defect engineering to produce graphene membranes with large concentration of SW(55-77) defect but in absence of other defects. Such membranes could significantly increase the efficiency of hydron isotope separation. In regards to hydrogenation of graphene, since it increases the particle flows dramatically

but reduces the selectivity meanwhile. Thus, hydrogenation could be considered in the technologies such as proton-exchange membranes.

7.2 Further Work

Several intriguing next steps of this work would be carried out in the near future. One of them is to systemically search for 2D membranes that are capable for isotope sieving. One could aim not only for single particles such as hydrogen and helium, but also for the molecules, e.g., H_2 and D_2. The influence of pure quantum tunneling can be utilized to screen the proper materials.

Another very interesting topic is study the influence of lattice vibration of graphene to the permeation and separation of hydron isotopes. This would be challenging since the vibration of the lattice leads to different configurations of graphene. The budding idea at the moment is to first employ molecular dynamics, from which a series of graphene structures with different degrees of lattice vibration can be obtained. Afterwards, one needs to choose proper paths for hydron isotope through the distorted graphene to get the corresponding PESs. By applying the method developed in this work, one can then get a statistical view of how membrane breath affects the energy barriers and selectivities of hydron isotope tunnel through graphene. This could provide a closer insight for hydrogen isotope separation through graphene membranes.

Appendix

A1. Thermodynamic cycle-estimation of transfer energies

The energy involved in the process of H or H^+ entering from PdH_x electrode is difficult to estimate, as the atomistic details are not known. There is obviously a much stronger binding of H^+ to the layered material compared to H atom, however, a similar Coulomb energy penalty applies, when H^+ is removed from its PdH_x source. A rough estimation of the thermodynamic cycle suggests that both processes would show a similar energetic profile. Considering the experimental setup of Hu et al. [34], we estimate the total transfer energies of H^+ or H from the hydrogenated Pd side electrodes and the layered crystals. The transfer reactions are as followings

$$[Pd_nH_m]^+ + \ hBN \ \rightarrow [Pd_nH_{m-1}] + H^+@hBN$$

$$[Pd_nH_m] + \ hBN \ \rightarrow [Pd_nH_{m-1}] + H@hBN$$

The above reactions are described by thermodynamic cycles, both reactions are strongly endothermic with overall 2.18 eV for the transfer of a proton and 2.54 eV for the transfer of a H atom from the PdH_x electrodes to *h*-BN. This rough estimate mainly serves to show that the transfer of a proton is energetically less demanding compared to a hydrogen atom, however, the difference between the energies is in the range of the expected error bar of such a rough estimation. The full thermodynamic simulation of the process of proton or protium transfer in the device is beyond our present capabilities and requires more detailed atomistic information about the interface from the experiment. Considering the experimental conditions, the H species are injected from the PdH_x electrodes (we denote them in the calculation below as Pd_nH_m) and diffuse

through the evaporated Pd thin film before encountering the *h*-BN layered crystal [34]. The total reaction for H^+ in *h*-BN interspace can, therefore, be written as:

$[Pd_nH_m]^+ + h\text{-BN} \rightarrow [Pd_nH_{m-1}] + H^+@h\text{BN}$

The above equation is the sum of the partial reactions:

$[Pd_nH_m]^+ + e^- \rightarrow Pd_nH_m$ ΔE = -5.22 eV, experimental [210]

$Pd_nH_m \rightarrow Pd_nH_{m-1} + 1/2H_2$ ΔE = 0.15 eV, experimental [211]

$1/2H_2 \rightarrow H$ ΔE = 2.25 eV, experimental [35]

$H \rightarrow H^+ + e^-$ ΔE = 13.6 eV, exact

$H^+ + h\text{-BN} \rightarrow H^+@h\text{BN}$ ΔE = −8.6 eV, calculated, this work (see A2. Binding Energies).

Sum of all the above partial energies gives the total transfer energy for H^+ in *h*-BN of 2.18 eV.

The total reactions for H atom in *h*-BN interspace can be written as:

$[Pd_nH_m] + h\text{-BN} \rightarrow [Pd_nH_{m-1}] + H@h\text{BN}$

This equation can be separated to:

$Pd_nH_m \rightarrow Pd_nH_{m-1} + 1/2\ H_2$ ΔE = 0.15 eV, experimental [211]

$1/2\ H_2 \rightarrow H$ ΔE = 2.25 eV, experimental [35]

$H + h\text{-BN} \rightarrow H@h\text{BN}$ ΔE = 0.14 eV, calculated, this work.

Therefore, the total reaction energy for H atom transfer in between *h*-BN layers sums up to 2.54 eV. It is interesting to note that the protium recombination in the lattice, calculated to be 3.46 eV, lowers the transfer energy from PdH_x to *h*-BN by 1.73 eV per atom, resulting in only 0.81 eV per atom.

A2. Binding Energies

The binding energies were calculated as follows (explained on the example of *h*-BN with H^+): $E_b = E_{H+@h\text{-BN}} - E_{h\text{-BN}} - E_{H+}$, with $E_{h\text{-BN}}$ and E_{H+} being the energies of the

perfect *h*-BN and proton, respectively, and $E_{H+@h\text{-BN}}$ being the total energy of the combined structure of H^+@*h*-BN. Due to the difficulty to calculate the total energies of charged solid-state materials, we have used cluster models. For this purpose, we used Gaussian *09* software [188] to calculate the binding energy of proton in *h*-BN cluster with different flake sizes and number of layers (pyrene and coronene cluster models with 1-4 layers). These calculations were performed using more accurate exchange-correlation functional and atomic centered gaussian basis set, augmented with polarization and diffuse functions (B3LYP functional [212] with 6-311+g (d, p) basis set), both with and without zero point energy correction (see Figure A1). We found that the binding energies corrected with zero-point energy converge to -8.55 eV in pyrene and -8.61 eV in coronene cluster models.

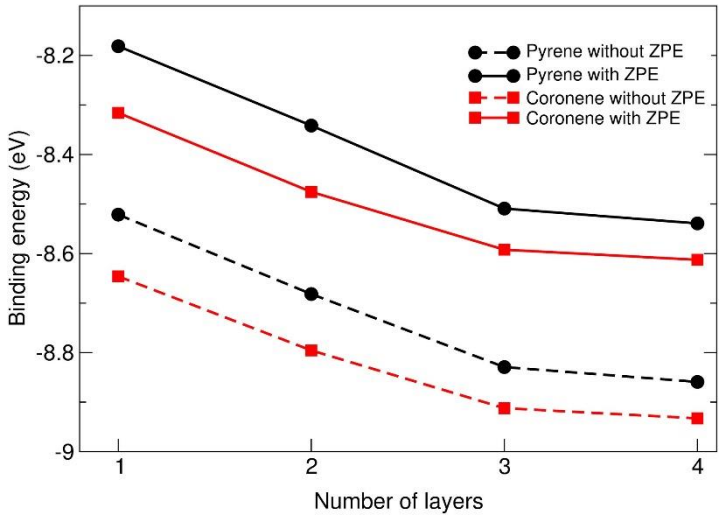

Figure A1. Binding energies with (solid lines) and without (dashed lines) zero-point energy (ZPE) correction for pyrene (black) and coronene (red).

A3. Spin flip energies

When two H atoms are in the interstitial space of a layered material, different spin states can be considered: singlet, triplet or antiferromagnetic singlet. The spin-flip energies for the latter two spin states of two H atoms were shown in Table A1. These energies are very small, therefore, results obtained for the triplet or antiferromagnetic singlet are nearly the same for distant protiums.

Table A1. Spin flip energies between triplet and antiferromagnetic singlet states of two H atoms.

System	2 H in the same layer (meV)	2 H in adjacent layers (meV)	2 H in different interstitials (meV)
2 H close	61.3	32.2	224.1
2 H far	0.8	0.7	0.8

A4. Periodic supercell models

The calculations of periodic graphene (see Figure A2) were carried out using DFT with Perdew-Burke-Ernzerhof (PBE) [64] functional and D3 correction of van der Waals interactions following the approach of Grimme [76], as implemented in the CP2K 5.1 package [171]. The Quickstep method was employed with Goedecker-Teter-Hutter [172] (GTH) pseudopotentials together with DZVP-MOLOPT-SR-GTH basis set. The plane-wave energy cutoff was set to 500 Ry and the reference grid was set to 60 Ry. For a charged system, the charge was set to the total system, calculated using the background charge as implemented in CP2K package. We used 5×5 supercell of graphene, for which the optimized lattice parameters are a = b = 2.47 Å, in good agreement with previous reports [170]. The procedure of calculating the potential energy surface (PES) of hydron isotope permeating through the periodic graphene is similar to that of coronene cluster model, see Section 5.3 in Chapter 5 for details.

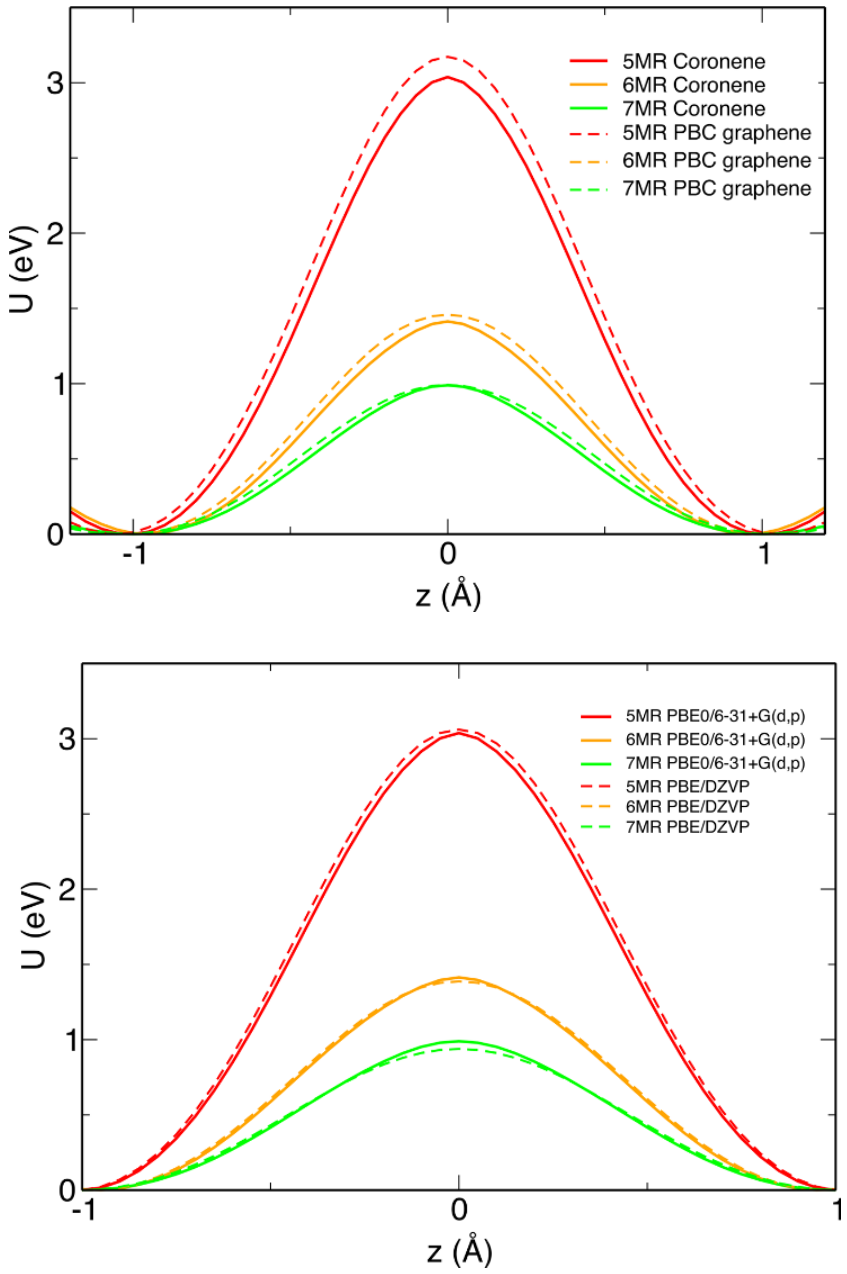

Figure A2. (Top) Comparison of the potential energy plots for H^+ passing through 5MR (red), 6MR (yellow), and 7MR (green) modeled using a coronene cluster (full lines) and a periodic structure of graphene (dashed lines). Coronene model calculated at the PBE0/6-31+G** level of theory and graphene at a lower level of PBE/DZVP. The overestimation of the barriers in periodic case might be a result of smaller basis set and also the fact that the background charge needed to be included in the simulations. (Bottom) Coronene model calculated at both levels of theory.

List of Publications

Peer-reviewed Publications

[1] An, Y., Oliveira, A., Brumme, T., Kuc, A., Heine, T. Stone-Wales defects cause high proton permeability and isotope selectivity of single-layer graphene. *Adv. Mater.*, 32 (37), 2002442. (2020)

[2] An, Y., Kuc, A., Petkov, P., Lozada-Hidalgo, M., Heine, T. On the chemistry and diffusion of hydrogen in the interstitial space of layered crystals *h*-BN, MoS_2, and graphite. *Small*, 15(43), 1901722. (2019)

[3] An, Y., Zhu, Y., Yao, Y., Liu, J. Is it possible to reverse aged acetylcholinesterase inhibited by organophosphorus compounds? Insight from the theoretical study. *Phys. Chem. Chem. Phys.*, *18*(14), 9838-9846. (2016)

Papers in Preparation

[4] Chen G., An, Y., et al., Edge tensile strain effect in Fe-N-C electrocatalysts for enhanced oxygen reduction reaction activity. In preparation. (2020)

[5] An, Y., Oliveira, A., Kuc, A., Heine, T. Pure quantum tunneling drives helium isotope separation through two-dimensional graphdiyne membrane. In preparation. (2020)

[6] An, Y., Springer, M., Oliveira, A., Brumme, T., Kuc, A., Heine, T. Influence of intrinsic ripples on graphene to the separation of hydron isotopes. In preparation. (2020)

[7] Wulf, T., An, Y., et al., Hydrogen isotope separation (review paper). In preparation. (2020)

Conference Contributions

1. Poster: *Proton Transport Through 2D Membranes*

   Y. An, A. Kuc, P. Petkov, A. F. Oliveira, T. Heine

   Chem 2D, Strasbourg, France (2017)

2. Talk: *Theoretical Insight of Hydrogen Isotopes Transport in Interstitial Space of Layered Materials*

   Y. An, A. Kuc, P. Petkov, M. L-Hidalgo, T. Heine

   DPG meeting, Berlin, Germany (2018)

3. Poster: *Hydrogen Particles Transport in Interstitial Space of Layered Materials*

   Y. An, A. Kuc, P. Petkov, M. L-Hidalgo, T. Heine

   Hengstberger Symposium, Heidelberg, Germany (2018**)**

4. Poster: *Proton Transport Through 2D Membranes*

   Y. An, A. Kuc, P. Petkov, A. F. Oliveira, T. Heine

   Hands-on DFT and Beyond workshop, Beijing, China (2018)

5. Poster: *Hydrogen Particles Transport in Interstitial Space of Layered Materials*

   Y. An; A. Kuc, P. Petkov, M. L-Hidalgo, T. Heine

   Flatlands beyond graphene, Leipzig, Germany (2018)

6. Talk: *Theoretical Insight of Hydrogen Transport in Interstitial Space of Layered Materials*

   Midterm Workshop Research Training Group “Quantum Mechanical Materials Modelling”, Etelsen, Germany (2018)

7. Poster: *Hydrogen Isotope Separation Through 2D Graphene Membrane*

   Y. An, A. F. Oliveira, T. Brumme, A. Kuc, T. Heine.

   International Workshop on Strong Correlations and Angle-Resolved Photoemission Spectroscopy CORPES19, Oxford, UK (2019)

8. Poster: *Hydrogen Isotope Separation Through 2D Graphene Membrane*

Y. An, A. F. Oliveira, T. Brumme, A. Kuc, T. Heine

GDCh meeting, Dresden, Germany (2019)

9. Talk: *Separating Hydrogen Isotopes Using 2D Graphene Membrane*

Y. An, A. F. Oliveira, T. Brumme, A. Kuc, T. Heine

HZDR workshop, Scheffau, Austria (2019)

10. Talk: *Hydrogen Isotope Separation Through 2D Graphene Membrane*

Y. An, A. F. Oliveira, T. Brumme, A. Kuc, T. Heine

Second Midterm Workshop Research Training Group “Quantum Mechanical Materials Modelling”, Etelsen, Germany (2019)

Acknowledgements

The last four years of Ph.D. study were a unique experience in my life. At the end, there are a great number of people to thank.

First of all, I am very grateful to my supervisor Prof. Thomas Heine, for his patient supervision and support during the years. As an excellent scientific thinker, his profound views and tons of great discussions were always enlightening. In addition, I would like to thank Prof. Ralf Tonner for agreeing to read my thesis as second reviewer.

I would also like to express big thanks to Agnieszka, especially for her co-supervision and support, as well as the kind encouragement during the last years. I am particularly grateful to Petko, who showed me the nuts and bolts of metadynamics at the very beginning of my study.

Huge thanks to Augusto, whose code makes quantum tunneling calculations much faster; I also thank him for all the fruitful discussions during the collaboration. I am indebted to Thomas (Brumme), especially for those idea-exchange on WKB approximation which had inspired me a lot. In addition, I particularly thank Antje, Katrin, and Kerstin, for their administrative support; thank our experimental collaborators for the nice collaboration and ZIH Dresden for the supercomputer time.

For sure I would like to thank my colleagues in the lab: thank Maximilian for all the help, especially for his kindness in explaining some German-related files and technical problems; thank Patrick for all the defense-related discussions, in particular for his cross-reading of my thesis and providing useful suggestions; thank Florian for the 3D printing of the model in the thesis; thank Lyuben and Knut for the IT support; and thank all the other members in the ThC group for creating such a nice working atmosphere.

Finally, I thank my parents Jiuhua Wang and Baowan An as well as my sisters, for their unconditional love and support throughout my life.

Bibliography

[1] Rao, A., Technology Breakthrough by Heavy Water Board in Material Support to Indian Nuclear Power Programme. *Energy Procedia* **2011,** *7*, 177-185.

[2] Rhodes, R., Why Nuclear Power Must Be Part of the Energy Solution. *Yale School of Forestry and Environmental studies* **2018**.

[3] Loveland, W. D.; Morrissey, D. J.; Seaborg, G. T., *Modern Nuclear Chemistry*. Wiley Online Library: **2006**; Vol. 20061.

[4] Saha, G. B.; Saha, G. B., *Fundamentals of Nuclear Pharmacy*. Springer: **2010**; Vol. 6.

[5] Shultis, J. K.; Faw, R. E., *Fundamentals of Nuclear Science and Engineering Third Edition*. CRC press: **2016**.

[6] Kikuchi, M.; Lackner, K.; Tran, M. Q., Fusion Physics. **2012**.

[7] Horibe, Y.; Kobayakawa, M., Deuterium Abundance of Natural Waters. *Geochim. Cosmochim. Acta* **1960,** *20*, 273-283.

[8] Miley, G. H.; Towner, H.; Ivich, N. *Fusion Cross Sections and Reactivities*; Illinois Univ., Urbana (USA): **1974**.

[9] Ayres, J.; Trilling, C., Heavy Water and Organic Fluids as Neutron Moderator and Reflector Materials. *Nucl. Eng. Des.* **1971,** *14*, 363-389.

[10] Alvarez, L.; Cornog, R., Radioactive Hydrogen. *Phys. Rev* **1940,** *57*, 248.

[11] Tanabe, T., *Tritium: Fuel of Fusion Reactors*. Springer: **2017**.

[12] Nagle, J.; Morowitz, H., Molecular Mechanisms for Proton Transport in Membranes. *Proc. Natl. Acad. Sci. U. S. A.* **1978,** *75*, 298-302.

[13] Stiopkin, I. V.; Weeraman, C.; Pieniazek, P. A.; Shalhout, F. Y.; Skinner, J. L.; Benderskii, A. V., Hydrogen Bonding at the Water Surface Revealed by Isotopic Dilution Spectroscopy. *Nature* **2011,** *474*, 192.

[14] Sanderson, K., Big Interest in Heavy Drugs. Nature Publishing Group: **2009**.

[15] Rae, H. In *Separation of Hydrogen Isotopes, American Chemical Symp*, Ser: **1978**.

[16] Miller, A. I., Heavy Water: A Manufacturers' Guide for the Hydrogen Century. *Canadian Nuclear Society Bulletin* **2001,** *22*, 1-14.

[17] Castell, L., *Time, Quantum and Information*. Springer Science: **2003**.

[18] Rae, H., Selecting Heavy Water Processes. ACS Publications: **1978**.

[19] Andreev, B. M., Separation of Hydrogen Isotopes in H_2O-H_2S System. *Sep. Sci. Technol.* **2001,** *36*, 1949-1989.

[20] Kestin, J.; Sengers, J.; Kamgar-Parsi, B.; Sengers, J. L., Thermophysical Properties of Fluid D2o. *J. Phys. Chem. Ref. Data* **1984,** *13*, 601-609.

[21] Beenakker, J.; Borman, V.; Krylov, S. Y., Molecular Transport in Subnanometer Pores: Zero-Point Energy, Reduced Dimensionality and Quantum Sieving. *Chem. Phys. Lett.* **1995,** *232*, 379-382.

[22] Cai, J.; Xing, Y.; Zhao, X., Quantum Sieving: Feasibility and Challenges for the Separation of Hydrogen Isotopes in Nanoporous Materials. *RSC advances* **2012,** *2*, 8579-8586.

[23] Oh, H.; Hirscher, M., Quantum Sieving for Separation of Hydrogen Isotopes Using Mofs. *Eur. J. Inorg. Chem.* **2016,** *2016*, 4278-4289.

[24] Kim, J. Y.; Zhang, L.; Balderas-Xicohténcatl, R.; Park, J.; Hirscher, M.; Moon, H. R.; Oh, H., Selective Hydrogen Isotope Separation Via Breathing Transition in Mil-53 (Al). *J. Am. Chem. Soc.* **2017,** *139*, 17743-17746.

[25] FitzGerald, S. A.; Pierce, C. J.; Rowsell, J. L.; Bloch, E. D.; Mason, J. A., Highly Selective Quantum Sieving of D_2 from H_2 by a Metal–Organic Framework as Determined by Gas Manometry and Infrared Spectroscopy. *J. Am. Chem. Soc.* **2013,** *135*, 9458-9464.

[26] Weinrauch, I.; Savchenko, I.; Denysenko, D.; Souliou, S.; Kim, H.; Le Tacon, M.; Daemen, L. L.; Cheng, Y.; Mavrandonakis, A.; Ramirez-Cuesta, A., Capture of Heavy Hydrogen Isotopes in a Metal-Organic Framework with Active Cu (I) Sites. *Nature Commun.* **2017,** *8*, 1-7.

[27] Kim, J. Y.; Balderas-Xicohténcatl, R.; Zhang, L.; Kang, S. G.; Hirscher, M.; Oh, H.; Moon, H. R., Exploiting Diffusion Barrier and Chemical Affinity of Metal–Organic Frameworks for Efficient Hydrogen Isotope Separation. *J. Am. Chem. Soc.* **2017,** *139*, 15135-15141.

[28] Zhao, X.; Villar-Rodil, S.; Fletcher, A. J.; Thomas, K. M., Kinetic Isotope Effect for H_2 and D_2 Quantum Molecular Sieving in Adsorption/Desorption on Porous Carbon Materials. *J. Phys. Chem. B* **2006,** *110*, 9947-9955.

[29] Wang, Q.; Challa, S. R.; Sholl, D. S.; Johnson, J. K., Quantum Sieving in Carbon Nanotubes and Zeolites. *Phys. Rev. Lett.* **1999,** *82*, 956.

[30] Kotoh, K.; Nishikawa, T.; Kashio, Y., Multi-Component Adsorption Characteristics of Hydrogen Isotopes on Synthetic Zeolite 5a-Type at 77.4 K. *J. Nucl. Sci. Technol.* **2002,** *39*, 435-441.

[31] Sugiyama, T.; Asakura, Y.; Uda, T.; Kotoh, K., Measurement of Breakthrough Curves on Pressure Swing Adsorption for Hydrogen Isotope Separation. *Fusion Sci. Technol.* **2005,** *48*, 163-166.

[32] Chen, B.; Zhao, X.; Putkham, A.; Hong, K.; Lobkovsky, E. B.; Hurtado, E. J.; Fletcher, A. J.; Thomas, K. M., Surface Interactions and Quantum Kinetic Molecular Sieving for H_2 and D_2 Adsorption on a Mixed Metal−Organic Framework Material. *J. Am. Chem. Soc.* **2008,** *130*, 6411-6423.

[33] Teufel, J.; Oh, H.; Hirscher, M.; Wahiduzzaman, M.; Zhechkov, L.; Kuc, A.; Heine, T.; Denysenko, D.; Volkmer, D., MFU-4–A Metal-Organic Framework for Highly Effective H_2/D_2 Separation. *Adv. Mater.* **2013,** *25*, 635-639.

[34] Hu, S.; Gopinadhan, K.; Rakowski, A.; Neek-Amal, M.; Heine, T.; Grigorieva, I.; Haigh, S.; Peeters, F.; Geim, A.; Lozada-Hidalgo, M., Transport of Hydrogen Isotopes through Interlayer Spacing in Van Der Waals Crystals. *Nature Nanotech.* **2018,** *13*, 468-472.

[35] Blanksby, S. J.; Ellison, G. B., Bond Dissociation Energies of Organic Molecules. *Acc. Chem. Res.* **2003,** *36*, 255-263.

[36] Miao, M.; Nardelli, M. B.; Wang, Q.; Liu, Y., First Principles Study of the

Permeability of Graphene to Hydrogen Atoms. *Phys. Chem. Chem. Phys.* **2013,** *15*, 16132-16137.

[37] Seel, M.; Pandey, R., Proton and Hydrogen Transport through Two-Dimensional Monolayers. *2D Materials* **2016,** *3*, 025004.

[38] Kroes, J.; Fasolino, A.; Katsnelson, M., Density Functional Based Simulations of Proton Permeation of Graphene and Hexagonal Boron Nitride. *Phys. Chem. Chem. Phys.* **2017,** *19*, 5813-5817.

[39] Achtyl, J. L.; Unocic, R. R.; Xu, L.; Cai, Y.; Raju, M.; Zhang, W.; Sacci, R. L.; Vlassiouk, I. V.; Fulvio, P. F.; Ganesh, P., Aqueous Proton Transfer across Single-Layer Graphene. *Nature Commun.* **2015,** *6*, 1-7.

[40] Hu, S.; Lozada-Hidalgo, M.; Wang, F. C.; Mishchenko, A.; Schedin, F.; Nair, R. R.; Hill, E. W.; Boukhvalov, D. W.; Katsnelson, M. I.; Dryfe, R. A. W.; Grigorieva, I. V.; Wu, H. A.; Geim, A. K., Proton Transport through One-Atom-Thick Crystals. *Nature* **2014,** *516*, 227-230.

[41] Lozada-Hidalgo, M.; Hu, S.; Marshall, O.; Mishchenko, A.; Grigorenko, A.; Dryfe, R.; Radha, B.; Grigorieva, I.; Geim, A., Sieving Hydrogen Isotopes through Two-Dimensional Crystals. *Science* **2016,** *351*, 68-70.

[42] Hu, S.; Lozada-Hidalgo, M.; Wang, F.; Mishchenko, A.; Schedin, F.; Nair, R.; Hill, E.; Boukhvalov, D.; Katsnelson, M.; Dryfe, R., Proton Transport through One-Atom-Thick Crystals. *Nature* **2014,** *516*, 227-230.

[43] Mogg, L.; Zhang, S.; Hao, G.-P.; Gopinadhan, K.; Barry, D.; Liu, B.; Cheng, H.; Geim, A.; Lozada-Hidalgo, M., Perfect Proton Selectivity in Ion Transport through Two-Dimensional Crystals. *Nature Commun.* **2019,** *10*, 1-5.

[44] Feng, Y.; Chen, J.; Fang, W.; Wang, E.-G.; Michaelides, A.; Li, X.-Z., Hydrogenation Facilitates Proton Transfer through Two-Dimensional Honeycomb Crystals. *J. Phys. Chem. Lett.,* **2017,** *8*, 6009-6014.

[45] Bartolomei, M.; Hernández, M. I.; Campos-Martínez, J.; Hernández-Lamoneda, R., Graphene Multi-Protonation: A Cooperative Mechanism for Proton Permeation. *Carbon* **2019,** *144*, 724-730.

[46] Li, G.; Li, Y.; Liu, H.; Guo, Y.; Li, Y.; Zhu, D., Architecture of Graphdiyne Nanoscale Films. *Chem. Commun.* **2010,** *46*, 3256-3258.

[47] Baughman, R.; Eckhardt, H.; Kertesz, M., Structure-Property Predictions for New Planar Forms of Carbon: Layered Phases Containing sp^2 and sp Atoms. *J. Chem. Phys.* **1987,** *87*, 6687-6699.

[48] Narita, N.; Nagai, S.; Suzuki, S.; Nakao, K., Optimized Geometries and Electronic Structures of Graphyne and Its Family. *Phys. Rev. B* **1998,** *58*, 11009.

[49] Huang, C.; Li, Y.; Wang, N.; Xue, Y.; Zuo, Z.; Liu, H.; Li, Y., Progress in Research into 2D Graphdiyne-Based Materials. *Chem. Rev.* **2018,** *118*, 7744-7803.

[50] Li, Y.; Xu, L.; Liu, H.; Li, Y., Graphdiyne and Graphyne: From Theoretical Predictions to Practical Construction. *Chem. Soc. Rev.* **2014,** *43*, 2572-2586.

[51] Hirsch, A., The Era of Carbon Allotropes. *Nature materials* **2010,** *9*, 868-871.

[52] Born, M.; Oppenheimer, R., Zur Quantentheorie Der Molekeln. *Annalen der physik* **1927,** *389*, 457-484.

[53] Hall, B. C., *Quantum Theory for Mathematicians*. Springer: **2013**; Vol. 267.

[54] Thomas, L. H. In *The Calculation of Atomic Fields*, Mathematical Proceedings of the Cambridge Philosophical Society, Cambridge University Press: **1927**; pp 542-548.

[55] Fermi, E., Un Metodo Statistico Per La Determinazione Di Alcune Priorieta Dell'atome. *Rend. Accad. Naz. Lincei* **1927,** *6*, 32.

[56] Hohenberg, P.; Kohn, W., Inhomogeneous Electron Gas. *Phys. Rev.* **1964,** *136*, B864.

[57] Kohn, W.; Sham, L. J., Self-Consistent Equations Including Exchange and Correlation Effects. *Phys. Rev.* **1965,** *140*, A1133.

[58] Hartree, D. R. In *The Wave Mechanics of an Atom with a Non-Coulomb Central Field. Part I. Theory and Methods*, Mathematical Proceedings of the Cambridge Philosophical Society, Cambridge University Press: **1928**; pp 89-110.

[59] Perdew, J. P.; Schmidt, K. In *Jacob's Ladder of Density Functional Approximations for the Exchange-Correlation Energy*, AIP Conference Proceedings, American

Institute of Physics: **2001**; pp 1-20.

[60] Gell-Mann, M.; Brueckner, K. A., Correlation Energy of an Electron Gas at High Density. *Phys. Rev.* **1957,** *106*, 364.

[61] Sousa, S. F.; Fernandes, P. A.; Ramos, M. J., General Performance of Density Functionals. *J. Phys. Chem. A* **2007,** *111*, 10439-10452.

[62] Haas, P.; Tran, F.; Blaha, P.; Schwarz, K.; Laskowski, R., Insight into the Performance of Gga Functionals for Solid-State Calculations. *Phys. Rev. B* **2009,** *80*, 195109.

[63] Haas, P.; Tran, F.; Blaha, P., Calculation of the Lattice Constant of Solids with Semilocal Functionals. *Phys. Rev. B* **2009,** *79*, 085104.

[64] Perdew, J. P.; Burke, K.; Ernzerhof, M., Generalized Gradient Approximation Made Simple. *Phys. Rev. Lett.* **1996,** *77*, 3865.

[65] Becke, A. D., Correlation Energy of an Inhomogeneous Electron Gas: A Coordinate-Space Model. *J. Chem. Phys.* **1988,** *88*, 1053-1062.

[66] Zhao, Y.; Schultz, N. E.; Truhlar, D. G., Exchange-Correlation Functional with Broad Accuracy for Metallic and Nonmetallic Compounds, Kinetics, and Noncovalent Interactions. American Institute of Physics: **2005**.

[67] Fock, V., Näherungsmethode Zur Lösung Des Quantenmechanischen Mehrkörperproblems. *Zeitschrift für Physik* **1930,** *61*, 126-148.

[68] Adamo, C.; Barone, V., Toward Reliable Density Functional Methods without Adjustable Parameters: The PBE0 Model. *J. Chem. Phys.* **1999,** *110*, 6158-6170.

[69] Perdew, J. P.; Ernzerhof, M.; Burke, K., Rationale for Mixing Exact Exchange with Density Functional Approximations. *J. Chem. Phys.* **1996,** *105*, 9982-9985.

[70] Dykstra, C.; Frenking, G.; Kim, K.; Scuseria, G., *Theory and Applications of Computational Chemistry: The First Forty Years*. Elsevier: **2011**.

[71] Lin, Y.-S.; Tsai, C.-W.; Li, G.-D.; Chai, J.-D., Long-Range Corrected Hybrid Meta-Generalized-Gradient Approximations with Dispersion Corrections. *J. Chem. Phys.* **2012,** *136*, 154109.

[72] London, F., Zur Theorie Und Systematik Der Molekularkräfte. *Zeitschrift für*

Physik **1930,** *63*, 245-279.

[73] Wagner, J. P.; Schreiner, P. R., London Dispersion in Molecular Chemistry—Reconsidering Steric Effects. *Angew. Chem. Int. Ed.* **2015,** *54*, 12274-12296.

[74] Grimme, S., Semiempirical Gga-Type Density Functional Constructed with a Long-Range Dispersion Correction. *J. Comput. Chem.* **2006,** *27*, 1787-1799.

[75] Grimme, S.; Antony, J.; Ehrlich, S.; Krieg, H., A Consistent and Accurate Ab Initio Parametrization of Density Functional Dispersion Correction (DFT-D) for the 94 Elements H-Pu. *J. Chem. Phys.* **2010,** *132*, 154104.

[76] Grimme, S.; Ehrlich, S.; Goerigk, L., Effect of the Damping Function in Dispersion Corrected Density Functional Theory. *J. Comput. Chem.* **2011,** *32*, 1456-1465.

[77] Coester, F., Bound States of a Many-Particle System. *Nuclear Physics* **1958,** *7*, 421-424.

[78] Coester, F.; Kümmel, H., Short-Range Correlations in Nuclear Wave Functions. *Nuclear Physics* **1960,** *17*, 477-485.

[79] Čížek, J., On the Correlation Problem in Atomic and Molecular Systems. Calculation of Wavefunction Components in Ursell-Type Expansion Using Quantum-Field Theoretical Methods. *J. Chem. Phys.* **1966,** *45*, 4256-4266.

[80] Bartlett, R. J.; Musiał, M., Coupled-Cluster Theory in Quantum Chemistry. *Reviews of Modern Physics* **2007,** *79*, 291.

[81] Riley, K. E.; Pitonák, M.; Jurecka, P.; Hobza, P., Stabilization and Structure Calculations for Noncovalent Interactions in Extended Molecular Systems Based on Wave Function and Density Functional Theories. *Chem. Rev.* **2010,** *110*, 5023-5063.

[82] Morse, P. M., Diatomic Molecules According to the Wave Mechanics. Ii. Vibrational Levels. *Phys. Rev.* **1929,** *34*, 57.

[83] Nimtz, G.; Haibel, A., Zero Time Space. How Quantum Tunneling Broke the Light Speed Barrier. **2008**.

[84] Mandelstam, L.; Leontowitsch, M., Zur Theorie Der Schrödingerschen Gleichung. *Zeitschrift für Physik* **1928,** *47*, 131-136.

[85] Layfield, J. P.; Hammes-Schiffer, S., Hydrogen Tunneling in Enzymes and Biomimetic Models. *Chem. Rev.* **2014,** *114*, 3466-3494.

[86] Pu, J.; Gao, J.; Truhlar, D. G., Multidimensional Tunneling, Recrossing, and the Transmission Coefficient for Enzymatic Reactions. *Chem. Rev.* **2006,** *106*, 3140-3169.

[87] Heisenberg, W., ber Den Anschaulichen Inhalt Der Quantentheoretischen Kinematik Und Mechanik. In *Original Scientific Papers Wissenschaftliche Originalarbeiten*, Springer: **1985**; pp 478-504.

[88] Bohm, D., Quantum Theory Prentice-Hall. *Englewood Cliffs, NJ* **1951**.

[89] Doolittle, W. A., *Wkb Approximation, Variational Methods and the Harmonic Oscillator*. **2005**.

[90] Cocolicchio, D.; Viggiano, M., Wkb Approximation without Divergences. *Int. J. Theor. Phys.* **1997,** *36*, 3051-3064.

[91] Albeverio, S.; Høegh-Krohn, R.; Mazzucchi, S., *Mathematical Theory of Feynman Path Integrals: An Introduction*. Springer Science & Business Media: **2008**; Vol. 523.

[92] Marx, D.; Parrinello, M., Ab Initio Path Integral Molecular Dynamics: Basic Ideas. *J. Chem. Phys.* **1996,** *104*, 4077-4082.

[93] Berne, B. J.; Thirumalai, D., On the Simulation of Quantum Systems: Path Integral Methods. *Annu. Rev. Phys. Chem.* **1986,** *37*, 401-424.

[94] Taylor, J. R.; Dubson, M. A.; Zafiratos, C. D., *Modern Physics for Scientists and Engineers*. Prentice-Hall: **2004**.

[95] Razavy, M., *Quantum Theory of Tunneling*. World Scientific: **2003**.

[96] Zwanzig, R. W., High-Temperature Equation of State by a Perturbation Method. I. Nonpolar Gases. *J. Chem. Phys.* **1954,** *22*, 1420-1426.

[97] Laio, A.; Parrinello, M., Escaping Free-Energy Minima. *Proc. Natl. Acad. Sci. U. S. A.* **2002,** *99*, 12562-12566.

[98] Tuckerman, M., *Statistical Mechanics: Theory and Molecular Simulation*. Oxford university press: **2010**.

[99] Barducci, A.; Bussi, G.; Parrinello, M., Well-Tempered Metadynamics: A Smoothly Converging and Tunable Free-Energy Method. *Phys. Rev. Lett.* **2008,** *100*, 020603.

[100] Novoselov, K. S.; Geim, A. K.; Morozov, S. V.; Jiang, D.; Zhang, Y.; Dubonos, S. V.; Grigorieva, I. V.; Firsov, A. A., Electric Field Effect in Atomically Thin Carbon Films. *Science* **2004,** *306*, 666-669.

[101] Liu, Y.; Bhowmick, S.; Yakobson, B. I., Bn White Graphene with "Colorful" Edges: The Energies and Morphology. *Nano Lett.* **2011,** *11*, 3113-3116.

[102] Dean, C. R.; Young, A. F.; Meric, I.; Lee, C.; Wang, L.; Sorgenfrei, S.; Watanabe, K.; Taniguchi, T.; Kim, P.; Shepard, K. L., Boron Nitride Substrates for High-Quality Graphene Electronics. *Nature Nanotech.* **2010,** *5*, 722-726.

[103] Pacile, D.; Meyer, J.; Girit, Ç.; Zettl, A., The Two-Dimensional Phase of Boron Nitride: Few-Atomic-Layer Sheets and Suspended Membranes. *Appl. Phys. Lett.* **2008,** *92*, 133107.

[104] Dickinson, R. G.; Pauling, L., The Crystal Structure of Molybdenite. *J. Am. Chem. Soc.* **1923,** *45*, 1466-1471.

[105] Joensen, P.; Frindt, R.; Morrison, S. R., Single-Layer MoS_2. *Mater. Res. Bull.* **1986,** *21*, 457-461.

[106] Osada, M.; Sasaki, T., Two-Dimensional Dielectric Nanosheets: Novel Nanoelectronics from Nanocrystal Building Blocks. *Adv. Mater.* **2012,** *24*, 210-228.

[107] Ayari, A.; Cobas, E.; Ogundadegbe, O.; Fuhrer, M. S., Realization and Electrical Characterization of Ultrathin Crystals of Layered Transition-Metal Dichalcogenides. *J. Appl. Phys.* **2007,** *101*, 014507.

[108] Frindt, R.; Yoffe, A., Physical Properties of Layer Structures: Optical Properties and Photoconductivity of Thin Crystals of Molybdenum Disulphide. *Proc. Roy. Soc. Lond. Math. Phys. Sci.* **1963,** *273*, 69-83.

[109] Mattheiss, L., Band Structures of Transition-Metal-Dichalcogenide Layer Compounds. *Phys. Rev. B* **1973,** *8*, 3719.

[110] Dumcenco, D.; Ovchinnikov, D.; Marinov, K.; Lazic, P.; Gibertini, M.; Marzari, N.;

Sanchez, O. L.; Kung, Y.-C.; Krasnozhon, D.; Chen, M.-W., Large-Area Epitaxial Monolayer MoS_2. *ACS nano* **2015,** *9*, 4611-4620.

[111] Li, L.; Yu, Y.; Ye, G. J.; Ge, Q.; Ou, X.; Wu, H.; Feng, D.; Chen, X. H.; Zhang, Y., Black Phosphorus Field-Effect Transistors. *Nature Nanotech.* **2014,** *9*, 372.

[112] Liu, H.; Neal, A. T.; Zhu, Z.; Luo, Z.; Xu, X.; Tománek, D.; Ye, P. D., Phosphorene: An Unexplored 2D Semiconductor with a High Hole Mobility. *ACS nano* **2014,** *8*, 4033-4041.

[113] Reich, E. S., Phosphorene Excites Materials Scientists. *Nature* **2014,** *506*, 19.

[114] Carvalho, A.; Wang, M.; Zhu, X.; Rodin, A. S.; Su, H.; Neto, A. H. C., Phosphorene: From Theory to Applications. *Nat. Rev. Mater.* **2016,** *1*, 1-16.

[115] Geim, A. K.; Grigorieva, I. V., Van Der Waals Heterostructures. *Nature* **2013,** *499*, 419-425.

[116] José-Yacamán, M.; Rendón, L.; Arenas, J.; Puche, M. C. S., Maya Blue Paint: An Ancient Nanostructured Material. *Science* **1996,** *273*, 223-225.

[117] Raccichini, R.; Varzi, A.; Passerini, S.; Scrosati, B., The Role of Graphene for Electrochemical Energy Storage. *Nat. Mater.* **2015,** *14*, 271-279.

[118] Bonaccorso, F.; Sun, Z.; Hasan, T.; Ferrari, A., Graphene Photonics and Optoelectronics. *Nat. Photonics* **2010,** *4*, 611.

[119] Zhang, H., Ultrathin Two-Dimensional Nanomaterials. *ACS nano* **2015,** *9*, 9451-9469.

[120] Neto, A. C.; Guinea, F.; Peres, N. M.; Novoselov, K. S.; Geim, A. K., The Electronic Properties of Graphene. *Rev. Mod. Phys.* **2009,** *81*, 109.

[121] Yi, M.; Shen, Z., A Review on Mechanical Exfoliation for the Scalable Production of Graphene. *J. Mater. Chem. A* **2015,** *3*, 11700-11715.

[122] Yu, Q.; Jauregui, L. A.; Wu, W.; Colby, R.; Tian, J.; Su, Z.; Cao, H.; Liu, Z.; Pandey, D.; Wei, D., Control and Characterization of Individual Grains and Grain Boundaries in Graphene Grown by Chemical Vapour Deposition. *Nat. Mater.* **2011,** *10*, 443-449.

[123] Obraztsov, A. N., Chemical Vapour Deposition: Making Graphene on a Large

Scale. *Nature Nanotech.* **2009,** *4*, 212.

[124] Chen, Z.; Ren, W.; Gao, L.; Liu, B.; Pei, S.; Cheng, H.-M., Three-Dimensional Flexible and Conductive Interconnected Graphene Networks Grown by Chemical Vapour Deposition. *Nat. Mater.* **2011,** *10*, 424.

[125] Coleman, J. N., Liquid Exfoliation of Defect-Free Graphene. *Acc. Chem. Res.* **2013,** *46*, 14-22.

[126] Banhart, F.; Kotakoski, J.; Krasheninnikov, A. V., Structural Defects in Graphene. *ACS nano* **2011,** *5*, 26-41.

[127] Huang, P. Y.; Ruiz-Vargas, C. S.; Van Der Zande, A. M.; Whitney, W. S.; Levendorf, M. P.; Kevek, J. W.; Garg, S.; Alden, J. S.; Hustedt, C. J.; Zhu, Y., Grains and Grain Boundaries in Single-Layer Graphene Atomic Patchwork Quilts. *Nature* **2011,** *469*, 389-392.

[128] Liu, L.; Qing, M.; Wang, Y.; Chen, S., Defects in Graphene: Generation, Healing, and Their Effects on the Properties of Graphene: A Review. *J. Mater. Sci. Technol.* **2015,** *31*, 599-606.

[129] Zhang, K.; Feng, Y.; Wang, F.; Yang, Z.; Wang, J., Two Dimensional Hexagonal Boron Nitride (2D-hBN): Synthesis, Properties and Applications. *J. Mater. Chem. C* **2017,** *5*, 11992-12022.

[130] Constantinescu, G.; Kuc, A.; Heine, T., Stacking in Bulk and Bilayer Hexagonal Boron Nitride. *Phys. Rev. Lett.* **2013,** *111*, 036104.

[131] Marom, N.; Bernstein, J.; Garel, J.; Tkatchenko, A.; Joselevich, E.; Kronik, L.; Hod, O., Stacking and Registry Effects in Layered Materials: The Case of Hexagonal Boron Nitride. *Phys. Rev. Lett.* **2010,** *105*, 046801.

[132] Kuzuba, T.; Era, K.; Ishii, T.; Sato, T., A Low Frequency Raman-Active Vibration of Hexagonal Boron Nitride. *Solid State Commun.* **1978,** *25*, 863-865.

[133] Geick, R.; Perry, C. H.; Rupprecht, G., Normal Modes in Hexagonal Boron Nitride. *Phys. Rev.* **1966,** *146*, 543-547.

[134] Kim, K. K.; Hsu, A.; Jia, X.; Kim, S. M.; Shi, Y.; Hofmann, M.; Nezich, D.; Rodriguez-Nieva, J. F.; Dresselhaus, M.; Palacios, T., Synthesis of Monolayer

Hexagonal Boron Nitride on Cu Foil Using Chemical Vapor Deposition. *Nano Lett.* **2012,** *12*, 161-166.

[135] Park, J.-H.; Park, J. C.; Yun, S. J.; Kim, H.; Luong, D. H.; Kim, S. M.; Choi, S. H.; Yang, W.; Kong, J.; Kim, K. K., Large-Area Monolayer Hexagonal Boron Nitride on Pt Foil. *Acs Nano* **2014,** *8*, 8520-8528.

[136] Gao, Y.; Ren, W.; Ma, T.; Liu, Z.; Zhang, Y.; Liu, W.-B.; Ma, L.-P.; Ma, X.; Cheng, H.-M., Repeated and Controlled Growth of Monolayer, Bilayer and Few-Layer Hexagonal Boron Nitride on Pt Foils. *ACS nano* **2013,** *7*, 5199-5206.

[137] Kim, G.; Jang, A.-R.; Jeong, H. Y.; Lee, Z.; Kang, D. J.; Shin, H. S., Growth of High-Crystalline, Single-Layer Hexagonal Boron Nitride on Recyclable Platinum Foil. *Nano Lett.* **2013,** *13*, 1834-1839.

[138] Mahvash, F.; Eissa, S.; Bordjiba, T.; Tavares, A.; Szkopek, T.; Siaj, M., Corrosion Resistance of Monolayer Hexagonal Boron Nitride on Copper. *Sci. Rep.* **2017,** *7*, 42139.

[139] Blase, X.; Rubio, A.; Louie, S. G.; Cohen, M. L., Quasiparticle Band Structure of Bulk Hexagonal Boron Nitride and Related Systems. *Phys. Rev. B* **1995,** *51*, 6868.

[140] Mak, K. F.; Lee, C.; Hone, J.; Shan, J.; Heinz, T. F., Atomically Thin MoS_2: A New Direct-Gap Semiconductor. *Phys. Rev. Lett.* **2010,** *105*, 136805.

[141] Lopez-Sanchez, O.; Lembke, D.; Kayci, M.; Radenovic, A.; Kis, A., Ultrasensitive Photodetectors Based on Monolayer MoS_2. *Nature Nanotech.* **2013,** *8*, 497-501.

[142] Zhang, W.; Chuu, C.-P.; Huang, J.-K.; Chen, C.-H.; Tsai, M.-L.; Chang, Y.-H.; Liang, C.-T.; Chen, Y.-Z.; Chueh, Y.-L.; He, J.-H., Ultrahigh-Gain Photodetectors Based on Atomically Thin Graphene-MoS_2 Heterostructures. *Sci. Rep.* **2014,** *4*, 3826.

[143] Bernardi, M.; Palummo, M.; Grossman, J. C., Extraordinary Sunlight Absorption and One Nanometer Thick Photovoltaics Using Two-Dimensional Monolayer Materials. *Nano Lett.* **2013,** *13*, 3664-3670.

[144] Tsai, M.-L.; Su, S.-H.; Chang, J.-K.; Tsai, D.-S.; Chen, C.-H.; Wu, C.-I.; Li, L.-J.; Chen, L.-J.; He, J.-H., Monolayer MoS_2 Heterojunction Solar Cells. *ACS nano*

2014, *8*, 8317-8322.

[145] Manzeli, S.; Ovchinnikov, D.; Pasquier, D.; Yazyev, O. V.; Kis, A., 2D Transition Metal Dichalcogenides. *Nat. Rev. Mater.* **2017,** *2*, 17033.

[146] Wang, Q. H.; Kalantar-Zadeh, K.; Kis, A.; Coleman, J. N.; Strano, M. S., Electronics and Optoelectronics of Two-Dimensional Transition Metal Dichalcogenides. *Nature Nanotech.* **2012,** *7*, 699.

[147] Tongay, S.; Zhou, J.; Ataca, C.; Liu, J.; Kang, J. S.; Matthews, T. S.; You, L.; Li, J.; Grossman, J. C.; Wu, J., Broad-Range Modulation of Light Emission in Two-Dimensional Semiconductors by Molecular Physisorption Gating. *Nano Lett.* **2013,** *13*, 2831-2836.

[148] Li, H.; Yin, Z.; He, Q.; Li, H.; Huang, X.; Lu, G.; Fam, D. W. H.; Tok, A. I. Y.; Zhang, Q.; Zhang, H., Fabrication of Single-and Multilayer MoS_2 Film-Based Field-Effect Transistors for Sensing No at Room Temperature. *Small* **2012,** *8*, 63-67.

[149] Late, D. J.; Huang, Y.-K.; Liu, B.; Acharya, J.; Shirodkar, S. N.; Luo, J.; Yan, A.; Charles, D.; Waghmare, U. V.; Dravid, V. P., Sensing Behavior of Atomically Thin-Layered MoS_2 Transistors. *ACS nano* **2013,** *7*, 4879-4891.

[150] Wakabayashi, N.; Smith, H. G.; Nicklow, R. M., Lattice Dynamics of Hexagonal MoS_2 Studied by Neutron Scattering. *Phys. Rev. B* **1975,** *12*, 659-663.

[151] Splendiani, A.; Sun, L.; Zhang, Y.; Li, T.; Kim, J.; Chim, C.-Y.; Galli, G.; Wang, F., Emerging Photoluminescence in Monolayer MoS_2. *Nano Lett.* **2010,** *10*, 1271-1275.

[152] Kuc, A.; Zibouche, N.; Heine, T., Influence of Quantum Confinement on the Electronic Structure of the Transition Metal Sulfide TS_2. *Phys. Rev. B* **2011,** *83*, 245213.

[153] Najmaei, S.; Yuan, J.; Zhang, J.; Ajayan, P.; Lou, J., Synthesis and Defect Investigation of Two-Dimensional Molybdenum Disulfide Atomic Layers. *Acc. Chem. Res.* **2015,** *48*, 31-40.

[154] Vancsó, P.; Magda, G. Z.; Pető, J.; Noh, J.-Y.; Kim, Y.-S.; Hwang, C.; Biró, L. P.;

Tapasztó, L., The Intrinsic Defect Structure of Exfoliated MoS_2 Single Layers Revealed by Scanning Tunneling Microscopy. *Sci. Rep.* **2016,** *6*, 29726.

[155] An, Y.; Kuc, A.; Petkov, P.; Lozada-Hidalgo, M.; Heine, T., On the Chemistry and Diffusion of Hydrogen in the Interstitial Space of Layered Crystals *h*-BN, MoS_2, and Graphite. *Small* **2019,** *15*, 1901722.

[156] Kitagawa, S.; Matsuda, R., Chemistry of Coordination Space of Porous Coordination Polymers. *Coord. Chem. Rev.* **2007,** *251*, 2490-2509.

[157] Fu, Q.; Bao, X., Surface Chemistry and Catalysis Confined under Two-Dimensional Materials. *Chem. Soc. Rev.* **2017,** *46*, 1842-1874.

[158] Chen, Z.; Leng, K.; Zhao, X.; Malkhandi, S.; Tang, W.; Tian, B.; Dong, L.; Zheng, L.; Lin, M.; Yeo, B. S.; Loh, K. P., Interface Confined Hydrogen Evolution Reaction in Zero Valent Metal Nanoparticles-Intercalated Molybdenum Disulfide. *Nature Commun.* **2017,** *8*, 14548.

[159] Novoselov, K.; Mishchenko, A.; Carvalho, A.; Neto, A. C., 2D Materials and Van Der Waals Heterostructures. *Science* **2016,** *353*, aac9439.

[160] Britnell, L.; Ribeiro, R. M.; Eckmann, A.; Jalil, R.; Belle, B. D.; Mishchenko, A.; Kim, Y.-J.; Gorbachev, R. V.; Georgiou, T.; Morozov, S. V.; Grigorenko, A. N.; Geim, A. K.; Casiraghi, C.; Neto, A. H. C.; Novoselov, K. S., Strong Light-Matter Interactions in Heterostructures of Atomically Thin Films. *Science* **2013,** *340*, 1311-1314.

[161] Geick, R.; Perry, C.; Rupprecht, G., Normal Modes in Hexagonal Boron Nitride. *Phys. Rev.* **1966,** *146*, 543.

[162] Verble, J. L.; Wietling, T. J.; Reed, P. R., Rigid-Layer Lattice Vibrations and Van Der Waals Bonding in Hexagonal MoS_2. *Solid State Commun.* **1972,** *11*, 941-944.

[163] Vancso, P.; Magda, G. Z.; Peto, J.; Noh, J. Y.; Kim, Y. S.; Hwang, C.; Biro, L. P.; Tapaszto, L., The Intrinsic Defect Structure of Exfoliated MoS_2 Single Layers Revealed by Scanning Tunneling Microscopy. *Sci. Rep.* **2016,** *6*, 29726.

[164] González-Herrero, H.; Gómez-Rodríguez, J. M.; Mallet, P.; Moaied, M.; Palacios, J. J.; Salgado, C.; Ugeda, M. M.; Veuillen, J.-Y.; Yndurain, F.; Brihuega, I.,

Atomic-Scale Control of Graphene Magnetism by Using Hydrogen Atoms. *Science* **2016,** *352*, 437-441.

[165] Chen, L.; Cooper, A. C.; Pez, G. P.; Cheng, H., Density Functional Study of Sequential H2 Dissociative Chemisorption on a Pt6 Cluster. *J. Phys. Chem. C* **2007,** *111*, 5514-5519.

[166] Yazyev, O. V., Magnetism in Disordered Graphene and Irradiated Graphite. *Phys. Rev. Lett.* **2008,** *101*, 037203.

[167] Beyer, W.; Wagner, H., Determination of the Hydrogen Diffusion Coefficient in Hydrogenated Amorphous Silicon from Hydrogen Effusion Experiments. *J. Appl. Phys.* **1982,** *53*, 8745-8750.

[168] Herrero, C. P.; Ramírez, R., Diffusion of Hydrogen in Graphite: A Molecular Dynamics Simulation. *J. Phys. D: Appl. Phys.* **2010,** *43*, 255402.

[169] Paine, R. T.; Narula, C. K., Synthetic Routes to Boron Nitride. *Chem. Rev.* **1990,** *90*, 73-91.

[170] Wyckoff, R. W. G., *Crystal Structures - Volume 1*. Interscience Publishers: New York, 1963.

[171] Hutter, J.; Iannuzzi, M.; Schiffmann, F.; VandeVondele, J., Cp2k: Atomistic Simulations of Condensed Matter Systems. *Wires: Comput. Mol. Sci.* **2014,** *4*, 15-25.

[172] Goedecker, S.; Teter, M.; Hutter, J., Separable Dual-Space Gaussian Pseudopotentials. *Phys. Rev. B* **1996,** *54*, 1703.

[173] Nosé, S., A Molecular Dynamics Method for Simulations in the Canonical Ensemble. *Mol. Phys.* **1984,** *52*, 255-268.

[174] Bussi, G.; Donadio, D.; Parrinello, M., Canonical Sampling through Velocity Rescaling. *J. Chem. Phys.* **2007,** *126*, 014101.

[175] Lipscomb, W. N., *Boron Hydrides*. Courier Corporation: **2012**.

[176] An, Y.; Oliveira, A. F.; Brumme, T.; Kuc, A.; Heine, T., Stone–Wales Defects Cause High Proton Permeability and Isotope Selectivity of Single-Layer Graphene. *Adv. Mater.* **2020,** *32*, 2002442.

[177] Souers, P., Hydrogen Properties for Fusion Energy University of California. Berkeley: **1986**.

[178] Ekanayake, N. T.; Huang, J.; Jakowski, J.; Sumpter, B. G.; Garashchuk, S., Relevance of the Nuclear Quantum Effects on the Proton/Deuteron Transmission through Hexagonal Boron Nitride and Graphene Monolayers. *J. Phys. Chem. C* **2017,** *121*, 24335-24344.

[179] Zhang, Q.; Ju, M.; Chen, L.; Zeng, X. C., Differential Permeability of Proton Isotopes through Graphene and Graphene Analogue Monolayer. *J. Phys. Chem. Lett.,* **2016,** *7*, 3395-3400.

[180] Bukola, S.; Liang, Y.; Korzeniewski, C.; Harris, J.; Creager, S., Selective Proton/Deuteron Transport through Nafion| Graphene| Nafion Sandwich Structures at High Current Density. *J. Am. Chem. Soc.* **2018,** *140*, 1743-1752.

[181] Walker, M. I.; Braeuninger-Weimer, P.; Weatherup, R. S.; Hofmann, S.; Keyser, U. F., Measuring the Proton Selectivity of Graphene Membranes. *Appl. Phys. Lett.* **2015,** *107*, 213104.

[182] Meyer, J. C.; Kisielowski, C.; Erni, R.; Rossell, M. D.; Crommie, M.; Zettl, A., Direct Imaging of Lattice Atoms and Topological Defects in Graphene Membranes. *Nano Lett.* **2008,** *8*, 3582-3586.

[183] Bracamonte, M. V.; Lacconi, G. I.; Urreta, S. E.; Foa Torres, L. E. F., On the Nature of Defects in Liquid-Phase Exfoliated Graphene. *J. Phys. Chem. C* **2014,** *118*, 15455-15459.

[184] Poltavsky, I.; Zheng, L.; Mortazavi, M.; Tkatchenko, A., Quantum Tunneling of Thermal Protons through Pristine Graphene. *J. Chem. Phys.* **2018,** *148*, 204707.

[185] Lozada-Hidalgo, M., Proton Conducting Membrane Comprising Monolithic 2D Material and Ionomer, a Process for Preparing Same and Use of Same in Fuel Cell and Hydrogen Gas Sensor. Google Patents: **2020**.

[186] Lozada-Hidalgo, M.; Zhang, S.; Hu, S.; Esfandiar, A.; Grigorieva, I. V.; Geim, A. K., Scalable and Efficient Separation of Hydrogen Isotopes Using Graphene-Based Electrochemical Pumping. *Nature Commun.* **2017,** *8*, 15215.

[187] Ma, J.; Alfe, D.; Michaelides, A.; Wang, E., Stone-Wales Defects in Graphene and Other Planar sp^2-Bonded Materials. *Phys. Rev. B* **2009,** *80*, 033407.

[188] Frisch, M.; Trucks, G. W.; Schlegel, H. B.; Scuseria, G. E.; Robb, M. A.; Cheeseman, J. R.; Scalmani, G.; Barone, V.; Mennucci, B.; Petersson, G. e., Gaussian~ 09 Revision D. 01. **2014**.

[189] Neese, F., Software Update: The Orca Program System, Version 4.0. *Wires: Comput. Mol. Sci.* **2018,** *8*, e1327.

[190] Griffin, E.; Mogg, L.; Hao, G.-P.; Kalon, G.; Bacaksiz, C.; Lopez-Polin, G.; Zhou, T.; Guarochico, V.; Cai, J.; Neumann, C., Proton and Li-Ion Permeation through Graphene with Eight-Atom-Ring Defects. *ACS Nano* **2020**.

[191] Ferrari, A. C.; Basko, D. M., Raman Spectroscopy as a Versatile Tool for Studying the Properties of Graphene. *Nature Nanotech.* **2013,** *8*, 235.

[192] Cançado, L. G.; Jorio, A.; Ferreira, E. M.; Stavale, F.; Achete, C. A.; Capaz, R. B.; Moutinho, M. V. d. O.; Lombardo, A.; Kulmala, T.; Ferrari, A. C., Quantifying Defects in Graphene Via Raman Spectroscopy at Different Excitation Energies. *Nano Lett.* **2011,** *11*, 3190-3196.

[193] Lucchese, M. M.; Stavale, F.; Ferreira, E. M.; Vilani, C.; Moutinho, M. V. d. O.; Capaz, R. B.; Achete, C. A.; Jorio, A., Quantifying Ion-Induced Defects and Raman Relaxation Length in Graphene. *Carbon* **2010,** *48*, 1592-1597.

[194] Gardiner Jr, W. C., Temperature Dependence of Bimolecular Gas Reaction Rates. *Acc. Chem. Res.* **1977,** *10*, 326-331.

[195] Silva, V. H.; Aquilanti, V.; de Oliveira, H. C.; Mundim, K. C., Uniform Description of Non-Arrhenius Temperature Dependence of Reaction Rates, and a Heuristic Criterion for Quantum Tunneling vs Classical Non-Extensive Distribution. *Chem. Phys. Lett.* **2013,** *590*, 201-207.

[196] Jiao, Y.; Du, A.; Hankel, M.; Zhu, Z.; Rudolph, V.; Smith, S. C., Graphdiyne: A Versatile Nanomaterial for Electronics and Hydrogen Purification. *Chem. Commun.* **2011,** *47*, 11843-11845.

[197] Hernández, M. I.; Bartolomei, M.; Campos-Martínez, J., Transmission of Helium

Isotopes through Graphdiyne Pores: Tunneling Versus Zero Point Energy Effects. *J. Phys. Chem. A* **2015,** *119*, 10743-10749.

[198] Bartolomei, M.; Carmona-Novillo, E.; Hernández, M. I.; Campos-Martínez, J.; Pirani, F.; Giorgi, G., Graphdiyne Pores:"Ad Hoc" Openings for Helium Separation Applications. *J. Phys. Chem. C* **2014,** *118*, 29966-29972.

[199] Cho, A., Helium-3 Shortage Could Put Freeze on Low-Temperature Research. American Association for the Advancement of Science: 2009.

[200] Halperin, W. P., The Impact of Helium Shortages on Basic Research. *Nature Physics* **2014,** *10*, 467-470.

[201] Hauser, A. W.; Schwerdtfeger, P., Nanoporous Graphene Membranes for Efficient ^{3}He/^{4}He Separation. *J. Phys. Chem. Lett.,* **2012,** *3*, 209-213.

[202] Nulakani, N. V. R.; Subramanian, V., A Theoretical Study on the Design, Structure, and Electronic Properties of Novel Forms of Graphynes. *J. Phys. Chem. C* **2016,** *120*, 15153-15161.

[203] Ivanovskii, A., Graphynes and Graphdyines. *Prog. Solid State Chem.* **2013,** *41*, 1-19.

[204] Chen, J.; Xi, J.; Wang, D.; Shuai, Z., Carrier Mobility in Graphyne Should Be Even Larger Than That in Graphene: A Theoretical Prediction. *J. Phys. Chem. Lett.,* **2013,** *4*, 1443-1448.

[205] Cranford, S. W.; Buehler, M. J., Mechanical Properties of Graphyne. *Carbon* **2011,** *49*, 4111-4121.

[206] Haley, M. M.; Brand, S. C.; Pak, J. J., Carbon Networks Based on Dehydrobenzoannulenes: Synthesis of Graphdiyne Substructures. *Angew. Chem. Int. Ed. Engl.* **1997,** *36*, 836-838.

[207] Jusélius, J.; Sundholm, D., The Aromaticity and Antiaromaticity of Dehydroannulenes. *Phys. Chem. Chem. Phys.* **2001,** *3*, 2433-2437.

[208] Kim, B. G.; Choi, H. J., Graphyne: Hexagonal Network of Carbon with Versatile Dirac Cones. *Phys. Rev. B* **2012,** *86*, 115435.

[209] Sun, L.; Jiang, P.; Liu, H.; Fan, D.; Liang, J.; Wei, J.; Cheng, L.; Zhang, J.; Shi, r.,

Graphdiyne: A Two-Dimensional Thermoelectric Material with High Figure of Merit. *Carbon* **2015,** *90*, 255-259.

[210] Jaeckel, R.; Wagner, B., Photo-Electric Measurement of the Work Function of Metals and Its Alteration after Gas Adsorption. *Vacuum* **1963,** *13*, 509-511.

[211] Johansson, M.; Skúlason, E.; Nielsen, G.; Murphy, S.; Nielsen, R. M.; Chorkendorff, I., Hydrogen Adsorption on Palladium and Palladium Hydride at 1bar. *Surf. Sci.* **2010,** *604*, 718-729.

[212] Lee, C.; Yang, W.; Parr, R. G., Development of the Colle-Salvetti Correlation-Energy Formula into a Functional of the Electron Density. *Phys. Rev. B* **1988,** *37*, 785.

Versicherung

Hiermit versichere ich, dass ich die vorliegende Arbeit ohne unzulässige Hilfe Dritter und ohne Benutzung anderer als der angegebenen Hilfsmittel angefertigt habe; die aus fremden Quellen direkt oder indirekt übernommen Gedanken sind als solche kenntlich gemacht. Die Arbeit wurde bisher weder im Inland noch im Ausland in gleicher oder ähnlicher Form einer anderen Prüfungsbehörde vorgelegt.

Datum 19. Januar 2021 Unterschrift 

Erklärung

Die vorliegende Arbeit wurde in der Zeit von Oktober 2016 bis Januar 2021 an der Technischen Universität Dresden im Rahmen des Projektes zum Thema: "Hydrogen Isotope Transport and Separation via Layered and Two-Dimensional Materials" unter wissenschaftlicher Betreuung von Herrn Prof. Dr. Thomas Heine durchgeführt.

Ich erkenne die Promotionsordnung dem Bereich für Chemie und Lebensmittelchemie der Technischen Universität Dresden vom 23.02.2011 in vollem Umfang an.

Datum 19. Januar 2021 Unterschrift